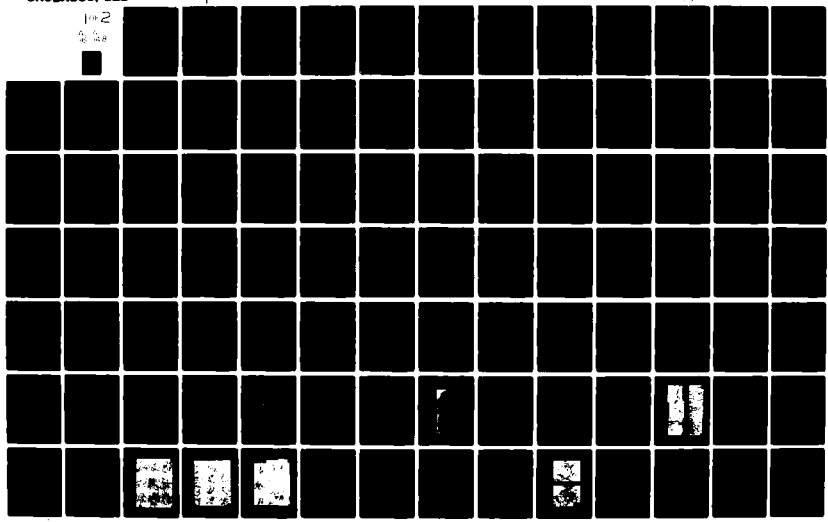


AD-A116 948

PENNSYLVANIA UNIV PHILADELPHIA DEPT OF MATERIALS SCI--ETC F/0 11/6
EFFECTS OF RESIDUAL IMPURITIES ON HYDROGEN ASSISTED CRACKING IN--ETC(U)
JUN 86 N BANDYOPADHYAY, C J MCNAULN NO8019-78-C-0327
ML

UNCLASSIFIED

100-2
5/28



(12)

NAVAL AIR SYSTEMS COMMAND

OFFICE OF NAVAL RESEARCH

AD A116948

CONTRACT N00019-78-C-0327

TECHNICAL REPORT

PART I

EFFECTS OF RESIDUAL IMPURITIES ON HYDROGEN
ASSISTED CRACKING IN HIGH STRENGTH STEELS

BY

N. BANDYOPADHYAY

AND

C. J. MCMAHON, JR.

DEPARTMENT OF MATERIALS SCIENCE AND ENGINEERING

SCHOOL OF ENGINEERING AND APPLIED SCIENCE

UNIVERSITY OF PENNSYLVANIA

PHILADELPHIA, PENNSYLVANIA

JUNE 1982



APPROVED FOR PUBLIC RELEASE
DISTRIBUTION UNLIMITED

82 07 15 043

DTIC FILE COPY

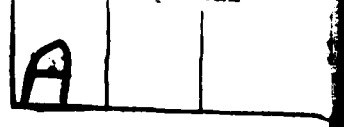
INTRODUCTION

Intergranular brittle fracture in steels can be induced either by the segregation of certain solute elements to the grain boundaries or by the segregation of absorbed hydrogen under stress⁽¹⁾. Alloying elements in steel are generally added because of their beneficial effects on the mechanical properties⁽²⁾. However, certain elements from groups IV, V and VI of the periodic table e.g. Sn, Sb, As, P, S, etc., when present in small quantities as impurities along with the usual alloying elements like Ni, Cr, Mn, Si, etc., can deteriorate the mechanical properties drastically by lowering the cohesion at the grain boundaries and thereby resulting in an intergranular brittle fracture along the prior austenite grain boundaries⁽³⁻⁶⁾. These problems, often encountered in service, are generally known as "temper embrittlement", "tempered martensite embrittlement (TME)", "hydrogen embrittlement (HE)", "stress corrosion cracking (SCC)", etc. The purpose of the present investigation was to clarify the effects of these impurity elements in promoting tempered martensite embrittlement and intergranular cracking in a hydrogen atmosphere at low stress intensity levels.

TEMPERED MARTENSITE EMBRITTLEMENT

The problem of tempered martensite embrittlement, also referred to as 350°C embrittlement, 500°F embrittlement, and one-step tempered embrittlement, is often encountered in commercial, ultra-high strength (yield strength > 200 ksi,

Codes
nd/or
al



1380 MPa) low-alloy steels with the tempered martensite structure. The embrittlement is observed when the as-quenched martensite is tempered in the temperature range of 250°-350°C for relatively short times (usually 1-2 h). The main characteristics of tempered martensite embrittlement can be summarized as follows:

- 1) There is an anomalous decrease (trough) in impact strength (usually measured by the room temperature Charpy V-notch energy) for a tempering treatment in the vicinity of 250°-350°C (480°-660°F) as shown in Figure 1, even though the hardness drops continuously through this temperature range (Figure 2).
- 2) The magnitude of the trough indicates the degree of embrittlement and the temperature range where it occurs specifies the critical heat treatment for this embrittlement.
- 3) The ductile-brittle transition temperature (DBTT) goes through a maximum corresponding to the minimum in the toughness curve. This is shown in Figure 3. The hump in the DBTT may be considered to be another manifestation of TME.
- 4) As shown in Figure 4, this loss in impact-strength or toughness corresponds to a change in fracture mode from predominantly transgranular fracture to almost complete intergranular fracture along prior austenite grain boundaries.

Grossman (in 1946)(9) first suggested that the carbides

formed during tempering play an important role in this type of intergranular embrittlement. He concluded that the loss in toughness after 500°F (260°C) tempering as compared to 400°F (200°C) tempering was due to the agglomeration of carbides on the grain boundaries and that this phenomenon was inherent in the tempering process itself. Later on, Lement et al.(10) (in 1954) investigated the microstructural changes that occur in martensite during tempering of high purity iron-carbon alloys containing 0.15 to 1.4% carbon. By careful electron microscopic studies, they showed that ϵ -carbide and a low carbon martensite containing about 0.25% carbon form after tempering at 300°-400°F (150°-205°C). The ϵ -carbide then progressively dissolves in the low-carbon martensitic matrix on tempering at 400°-600°F (205°-315°C) and is replaced by elongated carbide films at martensitic boundaries and both globular and platelet carbides within the martensite laths or plates. They identified these forms of carbide as cementite (Fe_3C). On tempering above 700°F(370°C), coalescence of the cementite particles occurs and this results in a general softening in the matrix. Similar observations were also made by Klingler et al.(7) using the X-ray diffraction technique. Both groups(7, 10) suggested that, regardless of the tempering time or temperature, the maximum in the Charpy fracture energy curve occurs in the presence of ϵ -carbide and the onset of the embrittlement is always coincident with the beginning of the precipitation of cementite platelets at the prior austenite grain boundaries. Hence, it was initially

believed that the grain boundary precipitation of these cementite platelets was responsible for this type of intergranular embrittlement.

Later, Schrader et al.(11) showed that the steels containing chromium and manganese were highly susceptible to this type of embrittlement, and they found that with about 0.1% Al the toughness trough was completely eliminated in the manganese steel. Therefore, they concluded that the embrittlement was due to the precipitation of a nitride of chromium or manganese.

These early observations(7-11) made on commercial purity steels suggested that this intergranular embrittlement was mainly due to the precipitation of either carbides or nitrides on the grain boundaries. But none of these observations could explain why an increase in P and/or S in these steels increased the severity of embrittlement(3).

Capus et al.(12) were the first to suggest that trace impurities in the steel might exert a major influence on 350°C embrittlement. By studying the impact properties of both "high-purity" and "commercial-purity" Ni-Cr-Mo steels, they found that the embrittlement trough was totally absent in the high-purity heat, whereas the commercial-purity heats containing added elements such as P, N, Sb, Sn, Mn, Si, showed the typical toughness trough in the tempering temperature range \approx 300°-350°C. This is shown in Figures 5 and 6. Hence, they concluded that the impact properties of hardened and tempered commercial

low-alloy steels were controlled to a large extent by the presence of impurity elements, that especially nitrogen and phosphorus play a significant role in "350°C embrittlement, and that the structural changes accompanying the tempering of martensite are not solely responsible for this kind of embrittlement. Electron microscopic studies showed no difference in the carbide precipitation sequence between the high-purity and commercial purity heats. Similar observations were also made by Banerji et al.(3) and Briant et al.(6). Capus and Mayer(12) also found that with 0.3% Si, there was a slight embrittling effect, and as the silicon content was increased (Figure 7), the minimum in the energy curve was found to be associated with progressively higher tempering temperatures. This indicates that silicon slows down the kinetics of embrittlement by delaying the tempering process. This silicon effect is consistent with the observations made by Allten and Payson(13). They found an increase in the ϵ -carbide \rightarrow cementite transformation temperature with silicon additions. A similar observation was also made by Alstetter et al.(14) who found that silicon stabilized ϵ -carbide, and hence the transformation of ϵ -carbide to cementite occurred at higher tempering temperature. The decomposition of low-carbon martensite into cementite and ferrite would also be retarded so that it occurs simultaneously with the dissolution of ϵ -carbide at a higher tempering temperature.

Schulz and McMahon(15) studied in detail the temper

embrittlement of AISI 3340 steel (3.5 Ni, 1.7 Cr, and 0.4C). In the asquenched condition, the fracture mode in 3340 steel with 600 ppm P showed complete intergranular fracture in both oil-quenched and brine-quenched specimens. Auger analysis of the intergranular facets showed the segregation of P. Hence, they suggested that segregation of phosphorus occurred at the grain boundaries in the austenite phase. This observation was later confirmed by Briant and Banerji (1,16), who found that the grain boundary phosphorus concentration did not change during tempering below 350°C. Hence, they(6,16) concluded that all impurity segregation which is important for 350°C embrittlement occurred during austenitization.

A great deal of progress has been made recently(3, 5-6, 17-18) in the understanding of impurity-induced intergranular embrittlement of alloy steels. Very recently, an exhaustive study of the scavenging properties of Mo, especially for P, had been made by Yu and McMahon(17) on 2.25 Cr, 1 Mo steel. They concluded that molybdenum, if available in the ferrite, can act as a powerful scavenger for phosphorus and other metalloid impurities. However, to use it effectively they suggested that molybdenum must be protected from carbide formation. The details of these mechanisms are given elsewhere(17-19).

All the observations on tempered martensite embrittlement suggest that the embrittlement might be due to the segregation of some impurity elements to the grain boundaries

in the austenite phase and not simply due to the structural changes accompanying the tempering of martensite. However, one must consider the possibility of impurity rejection from the growing carbides. Kula and Anctil⁽²⁰⁾ proposed a mechanism which involves an interaction between carbides and impurity elements. They proposed that, after the completion of the cementite precipitation at higher tempering temperatures, the alloying elements in cementite and ferrite would start to diffuse and redistribute themselves. They suggested that certain impurity elements which are more soluble in -ferrite will be rejected from the carbide after the carbide precipitation and hence would result in a transient enrichment of these impurity elements in the ferrite immediately adjacent to the thin, elongated cementite platelets. This, in turn, would cause tempered martensite (or 350°C) embrittlement by lowering the ferrite-carbide interfacial energy. Later, Rellick and McMahon⁽²¹⁾ suggested that the impurity rejection during carbide precipitation is more important than after precipitation. McMahon⁽²²⁾ suggested that the impurities such as S and P did not segregate at equilibrium in iron significantly when present in small quantity, but a transient enrichment of these impurities on the grain boundaries occurred as a result of solute redistribution during carbide formation and this in turn caused the 350°C embrittlement.

Recently, there has been a great deal of discussion about whether tempered martensite embrittlement is simply

an impurity-induced intergranular problem or carbide-induced transgranular (cleavage) problem which may or may not be accompanied by intergranular fracture. The latter viewpoint was proposed by King et al.(23) who made low temperature toughness measurements and fractographic observations on a quenched and tempered 0.6% C steel. They observed minima in the curves of K_{IC} vs. tempering temperature at approximately 297°C (570°K) for 0°C tests and approximately 392°C (665°K) for -100°C tests, for fracture which were reported to be 100% transgranular cleavage. The transgranular cleavage fracture appeared to run across the martensite packets. Based on these observations, they proposed that the coarsening of interlath cementite tends to enable larger crack nuclei to be formed, rather than to provide a more favourable path for propagation.

More recently, a lot of attention has been given to the role of retained austenite and its thermal decomposition to inter-lath cementite during tempering as a possible mechanism for tempered martensite embrittlement(24-27). Thomas and coworkers(24,28) suggested that these interlath retained austenite films, if stable, are beneficial to fracture toughness. Based on this, Thomas⁽²⁴⁾ concluded that the thermal instability of this retained austenite on subsequent tempering produced the embrittlement due to their decomposition to interlath films of $M_3\text{C}$ carbides. He reported that the fracture path were intergranular with respect to martensite but transgranular with respect to austenite.

Later, Horn and Ritchie^(25, 26) investigated the role of interlath films of retained austenite on fracture toughness of commercial, ultra-high strength 4340 and Si-modified 4340 (300-M) steels. Essentially, they made similar types of observations as Thomas⁽²⁴⁾. However, they suggested that the embrittlement was due to the interlath precipitation of cementite (because of partial thermal decomposition of interlath films of retained austenite) and to subsequent deformation-induced transformation (mechanical instability) of remaining interlath austenite to untempered martensite. They reported that the fracture mechanism was interlath cleavage when the steel contained a high volume fraction of retained austenite (as in case of air-cooled or isothermally-transformed) and transgranular cleavage or mixed cleavage/microvoid coalescence when the steel contained a low volume fraction of retained austenite.

However, these mechanisms^(23, 24, 25) could not satisfactorily explain why an increase in P and/or S content in these commercial steels increased the degree of embrittlement. Later on, Krauss et al.⁽²⁷⁾ showed the toughness and impact properties of quenched and tempered 4340-type steels with low (0.003 wt.%) and high (0.03 wt.%) phosphorus. From their observations, they concluded that in steels containing small amounts of phosphorus, the mechanism of brittle fracture involved the cracking of interlath cementite platelets formed by the decomposition of retained austenite and its subsequent propagation across

martensite laths, whereas in steels containing higher amounts of phosphorus the fracture involved extensive amounts of intergranular fracture and the embrittlement mechanism was due to a combination of phosphorus segregation and grain boundary carbides formed during tempering.

Thus, three major mechanisms have been proposed for tempered martensite embrittlement:

First, the embrittlement is due to grain boundary weakening, presumably by segregated impurity elements (e.g. P, S, N, Sn, Sb, etc.) and it is triggered by carbide formation at tempering temperatures above 150°C.

Secondly, the embrittlement is simply a carbide-induced transgranular (cleavage) problem which may or may not be accompanied by intergranular fracture and impurities do not have any significant role.

Thirdly, the embrittlement is due to the thermal decomposition of retained austenite into interlath cementite during tempering process.

Scope of the Present Investigation

From the foregoing literature survey it may be seen that despite the huge volume of data available from as early as 1946 when Grossman(9) first suggested the role of carbides on the intergranular tempered martensite embrittlement and as early as 1941 when Zapffe and Sims(29) made history by reporting how hydrogen flaking affected the quality of ship steel, the phenomena of both tempered martensite embrittlement

(TME) and hydrogen embrittling (HE) are still not adequately understood. Different investigators are still proposing different types of mechanisms to these problems and sometimes completely opposing models are still being supported. The central theme of this research work is essentially an evaluation of the impurity-hydrogen interaction in high strength steels.

Tempered Martensite Embrittlement

It is evident from the literature survey that most of the investigations done on this problem involve the use of commercial-purity steels. This problem was not approached extensively from the impurity point of view until relatively recently. What has been made clear is that intergranular TME involves the interaction of both impurities and carbides on the prior austenite grain boundaries. However, other theories such as King et al.(23), who proposed that TME is mainly a carbide-induced transgranular (cleavage) problem and Thomas(24) and Horn and Ritchie(25) who proposed that TME is mainly due to the thermal decomposition of the retained austenite into interlath carbides, must still be considered.

In the present investigation a systematic study using high purity vacuum-melted lab heats and a series of commercial-purity heats with varying amounts of Mn, Si, P and S was made to determine the mechanism of tempered martensite embrittlement. In the course of this investigation,

attention was focussed on resolving the following issues:

- 1) Whether TME is an impurity-induced intergranular fracture problem or a carbide-induced brittle fracture problem which may or may not be intergranular?
- 2) If it is an impurity-induced intergranular problem, what role do the carbides play in this kind of embrittlement?
- 3) What are the important impurities responsible for this embrittlement?
- 4) What is the role of alloying elements (especially Mn and Si) in promoting TME?
- 5) What controls the fracture mechanism (stress or strain) for TME observed at room temperature and low temperature?
- 6) What is the significance of test temperature with respect to the ductile-brittle transition temperature of the steel for observing TME?
- 7) If this embrittlement phenomenon is a result of segregation of trace impurities on the prior austenite grain boundaries, what is the necessary extent of such segregation?
- 8) To what extent can trace impurities (in the bulk) be tolerated in a commercial steel without seriously impairing the usefulness of such high strength steels?

EXPERIMENTAL PROCEDUREMaterials

The compositions of the steels used in this study are given in Table I. Five heats of vacuum-induction melted (VIM) 4340 steels (nos. 840, 841, 842, 843, and 846) were received from the Republic Steel Corporation Research Center. These heats were designed to reveal the effects of increasing the Mn content from 0.02 to 0.7% in the presence of low Si(0.01%) and of 0.27% Si in the presence of low Mn (0.02%). The purpose was to clarify the respective roles of these elements in promoting tempered martensite embrittlement (TME) and intergranular cracking in a hydrogen atmosphere at low stress intensity levels. The heats were processed into 1 1/2" x 4 1/2" x L billets with a soaking temperature of 2150°F (1177°C). They were then resoaked at 2000°F (1093°C) and cross rolled to 1.00" thick plates and finally straight rolled to a final thickness of 0.625". Subsequently, they were Blanchard ground to 0.50" thickness. Heats B7 and B6 had been received earlier (30) from the General Electric Company, Corporate Research and Development Center, and heat B2 was purchased from the J. T. Ryerson & Son, Inc., Pittsburgh. Heat B2 was a commercial 4340 steel which was air-melted and vacuum degassed. Heat B7 was a high-purity (VIM) NiCrMo steel having the 4340 base composition without Mn or Si and only residual levels of P and S.

Heat B6 was essentially the same as B7 with Mn and Si intentionally added to it.

Heat Treatment

The usual heat treatment of this type of steel involved austenitization in vacuum at $\sim 850^{\circ}\text{C}$ for one hour followed by quenching in oil. Coarse, medium, and fine prior austenite grain sizes were obtained by one-hour austenitization at 1150°C , 1000°C , and 850°C , respectively. This was followed by tempering for one hour in vacuum between 100°C and 525°C . Table II gives the range of grain sizes for the three austenitizing temperatures.

Mechanical Testing

Charpy Impact Test

Standard Charpy V-notch (CVN) impact specimens, tempered at various temperatures, were used to characterize tempered martensite embrittlement both at room temperature and liquid nitrogen temperature. The transition temperatures were measured in terms of the fracture energy over a temperature range from -196° to 100°C by using liquid nitrogen, ethanol, and silicone oil and according to the ASTM standard(31).

Four-Point Bend Test

The critical local fracture stress (σ^*) necessary for the formation of a brittle crack and the maximum principal fracture strain (ϵ^*) at the notch root for the initiation of ductile failure were measured by using both unnotched tensile and notched bend specimens. The shape

and dimensions of the specimens employed for these tests are shown in Figure 8. For the notched specimens, the shape and corresponding finite element elastic-plastic stress analysis developed by Griffiths and Owen(32) were used. This gives the maximum principal stress σ_{22} and maximum principal plastic strain as a function of nominal bending stress, both expressed as fractions of the uniaxial tensile yield stress (σ_y) and yield strain (ϵ_y), respectively. The nominal bending (net section) stress is given by $\sigma_{\text{nom}} = 6M/[B(W-a)^2]$, where M is the applied bending moment, B is the specimen thickness, W is the width, and a is the notch depth. The details of the finite element elastic-plastic stress analysis are given in Ref. 32 . Low temperature (77°K) tests were done by using a special jig to hold liquid nitrogen throughout the tests.

Fracture Toughness (K_{IC}) Tests

The fracture toughness tests were made under plane strain conditions, on fatigue pre-cracked compact tension specimens in accordance with ASTM standard E399(33). The dimensions of the test specimen were: thickness(B) = 10.16 mm, width (W) = 20.32 mm, and a/w = 0.5, where a is the length of the pre-crack. The crack-opening displacement was monitored by a clip gauge at the mouth of the crack, and the displacement with respect to the applied load was recorded by an X-Y recorder; examples of the curves are shown in Figure 9. The figure shows the plots of load vs. clip gauge displacement for steel B2 for

different tempering conditions. The extension of the crack was signalled by a discontinuity in the compliance or "pop-in". The final fracture was preceded by a series of "pop-in" indications. The load corresponding to the first pop-in was used to calculate K_{IC} ; it is given by:

$$K_{IC} = \frac{Y \cdot P \cdot \sqrt{a}}{B \cdot W}, \text{ where } Y = f(a/w), \text{ and } P \text{ is the load corresponding to first pop.}$$

Crack Growth Measurements in Hydrogen

The fracture mechanics approach was used to study crack growth in hydrogen. A modified wedge-opening-loading (WOL) pre-cracked specimen⁽³⁴⁾ was employed in this work. The specimen geometry is given in Figure 10. Semicircular, 5% face notches (side grooves) were used to guide the crack along a single plane. The self-loading of the sample was achieved by a bolt-and-tup arrangement and the crack propagation was recorded by the drop in load on the tup, with the help of strain gages mounted on the side faces of the tup. An analog-to-digital converter was used and the millivolt output was recorded by a teletype. Because the modified WOL specimen was loaded to a constant displacement with the bolt, the load and the crack length were uniquely related by the compliance of the system. The crack length and the stress intensity K were calculated by using the Novak and Rolfe⁽³⁴⁾ compliance calibration. Figure 11 shows the good agreement between their calibration and our experimental compliance calibration for steel 840 (850°C , 1h, OQ and 300°C , 1h, WQ). The stress intensity

value was determined from the measurement of the load at a fixed displacement using a calibration of the compliance of the specimen as a function of crack length through the equation(34):

$$K = \frac{P \cdot C_3(a/w)}{B \cdot a^{1/2}}$$

For the present side-grooved specimen, B is replaced by $(B_x B_n)$ where B_n is the net specimen thickness. The constant $C_3(a/w)$ is given by the following equation⁽³⁴⁾:

$$C_3(a/w) = 30.96(a/w) - 195.8(a/w)^2 + 730.6(a/w)^3 \\ - 1186.3(a/w)^4 + 754.6(a/w)^5$$

The hydrogen tests were performed at $23^\circ \pm 0.5^\circ\text{C}$ in a stainless steel chamber, previously evacuated to a pressure $\leq 10^{-5}$ torr, and then backfilled with high purity hydrogen gas (dried by passing through a liquid nitrogen cold trap) to the desired pressure. Gaseous hydrogen testing was chosen to avoid the uncertainties of complex surface reactions and electrochemical conditions inside a crack in aqueous media.

Fracture Surface Analysis and Metallography

Fracture surfaces of the specimens were analyzed by scanning electron microscopy (SEM) to determine the mode of fracture, with special emphasis on the amount of intergranular fracture. Composite pictures were taken near the notch root in order to have a reasonably complete idea of the total fracture process. The percent intergranular fracture

was measured by outlining the intergranular facets on a semitransparent paper and then counting the number of intersections on a sheet of graph paper. An average value of at least five areas was used to represent the fracture surface.

For metallography, the samples were ground and polished to a 0.5 m finish and then etched with saturated solution of picric acid with two grams of sodium tridecyl benzene sulfonate added to 100 ml of the solution as an wetting agent(35). The temperature of the solution was raised to 50°C. Figure 12 shows an example of the etched surfaces of two of the steels revealing the grain boundaries for fine and coarse grain conditions. The grain size was measured by the linear intercept method. A geometrical factor of 1.62 was applied to the measured diameter approximating the grains as regular tetrakaidecahedra(10).

Transmission Electron Microscopy

Grain boundary carbides were studied by the carbon extraction replica technique(36). The fracture surface was first etched with 3% Nital solution for 40 sec and then quickly rinsed with Methanol. Then a plastic replicating tape was pressed against the etched fracture surface over a thin film of acetone. After the acetone dried, the plastic tape was stripped off the specimen. A thin film (100 to 200 Å) of carbon was deposited on the surface of the plastic tape. The tape was then cut into small squares of about 2mm. Finally, the tape was dissolved in acetone while

holding the carbon replica on a 200 mesh grid. The extraction replica was examined with a Phillips 300 transmission electron microscope.

Auger Electron Spectroscopy

The segregation of impurities on the prior austenite grain boundaries was studied by a scanning Auger microprobe (SAM). The specimens of the geometry shown in Figure 13 were fractured inside the vacuum chamber in pure hydrogen by slow bending. This was done to produce more intergranular fracture by allowing hydrogen to diffuse into the material. The hydrogen was then pumped out and the chamber was evacuated to $\leq 10^{-10}$ torr. Measurements (spectra) were recorded from at least 10 locations on the fracture surface by using a grazing incidence primary beam. The operating conditions used in this study were as follows:

primary beam energy	5 keV
primary beam size	≤ 10 m
beam current	20 A
modulation voltage	6 eV

Measurement of Retained Austenite by Magnetic Saturation Method

Faraday's induction law is the basis of several methods of measuring magnetic moments and fields. Faraday's law states that when the magnetic flux Φ (maxwells) through a coil (Figure 14), is changing, an induced emf V is observed which is proportional to the time rate of change of

flux, $\frac{d\phi}{dt}$. For a coil of N turns each of area A, perpendicular to the flux, the induced emf is given by (37)

$$V = N \frac{d\phi}{dt} \times 10^{-8} = NA\mu dH/dt \times 10^{-8} \quad (1)$$

The factor 10^{-8} applies if V is in volts, dH/dt is in gauss per second, μ is the magnetic permeability, and A is in square centimeters.

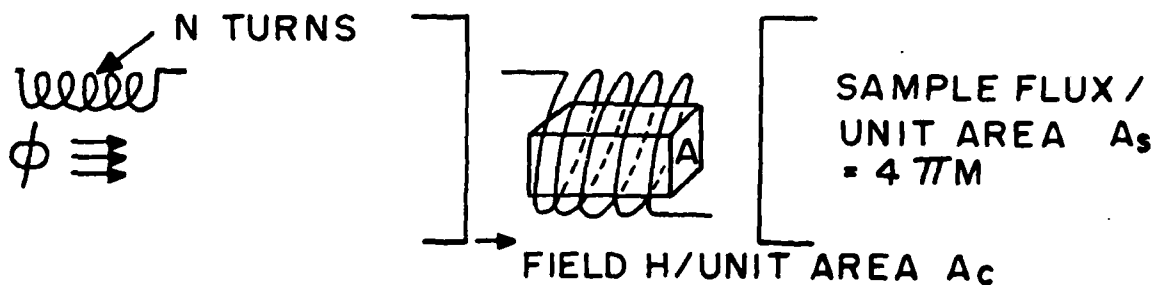


Figure 14

The total magnetic flux ϕ is given by

$$\phi = H A_c + 4\pi M A_s \quad (2)$$

flux due to the field	Flux due to the sample
-----------------------------	------------------------------

An O. S. Walker Electronic Integrator, Model MF1, was used to integrate the induced emf with respect to the time period. The integrated output is proportional to $\int V dt$ and is given by the expression

$$\int V dt = \int N \frac{d\phi}{dt} \times 10^{-8} dt = N \phi \times 10^{-8} \quad (3),$$

with the proportionality constant depending on the RC values of the integrator. From equations (2) and (3), the recorded emf is given by the expression,

$$V \text{ recorded} = N \times 10^{-8} (H A_c + 4\pi M A_s), \quad (4)$$

where A_c is the cross-sectional area of the coil and A_s is the cross-sectional area of the sample.

The electronic integrator circuit for the measuring magnetisation curves is shown in Figure 15. Coils 2 and 3 are sample sense coils and coils 1 and 4 are field buck-out coils. The cross-sectional areas of all the samples were kept constant. A pure "ferro-vac" electrolytic iron was used as a standard sample and the measurements on the unknown samples were done with respect to the standard.

EXPERIMENTAL RESULTS

Fracture Behavior in Air

Charpy Impact Tests

Room Temperature Impact Tests

Because of their high hardenability, the 4340-type steels examined here are martensitic after oil quenching. The reduction in hardness for one hour tempering over a wide range of tempering temperature is shown in Figure 16 for two vacuum-melted lab heats (B6 and B7) and one commercial heat which was air-melted and vacuum-degassed (B2). The hardness is essentially the same for all three heats, the scatter being essentially negligible. Because of this softening, one would expect that the fracture energy to increase monotonically with tempering temperature. However, as shown in Figure 17, only the "pure" steel B7 (with no Mn and Si added) shows this behavior. When Mn

and Si are added to get steel B6, the trough, characteristic of tempered martensite embrittlement (TME), appears. The figure shows the tempering temperature range of about 300-350°C as producing the most severe condition of embrittlement.

The commercial steel B2 also shows the TME trough, along with a considerably lower fracture energy than B6. This is presumably due to larger inclusion content in the air-melted steel B2, as illustrated in Figure 18 which shows examples of areas containing the largest inclusion concentration for steel B6 and B2.

Room temperature impact tests were done on a further series of steels with varying contents of Mn, Si, P, and S. Figure 19 shows the toughness troughs in the RTCVN energy as a function of tempering temperature for these heats in the fine grain size condition. The TME trough is absent, once again, in the Mn- and Si-free heat (no. 840). The addition of Mn and/or Si to this steel causes the appearance of the trough. With increasing bulk concentration of Mn, the depth of the trough increases, indicating that the steel is more and more embrittled. These results suggest that Mn, and perhaps Si(3,38), promote the segregation of P and S to the prior austenite grain boundaries even though the steel contains a very low amount of P and S. Figure 20 shows the reduction in hardness with tempering temperature for two Mn- and Si-free steels B7 and 840. The hardness is essentially

the same for both steels. However, comparing Figures 17 and 19, it may be seen that steel 840 shows lower energy values for all tempering conditions when tested at room temperature. This is presumably due to the fact that 840 has more phosphorus than B7 and, hence, even at room temperature it shows some brittle fracture. This is shown in Figure 21. Note that in case of B7, the fracture is completely ductile, but in case of 840, we can see a mixture of ductile, intergranular and cleavage fracture.

Impact Tests at 77°K

(A) High-Purity 4340-type steel. The Charpy specimens of steel B7 exhibit only rupture by microvoid coalescence in all specimens fractured at room temperature. Therefore, we know that this steel is above its ductile-brittle transition temperature at 23°C for all the tempering temperatures. This is confirmed in Figure 22, which gives the results of Charpy tests over a wide range of temperatures.

Three points to be noted here are:

1. Room temperature is on the upper energy shelf for all the tempering conditions.
2. The transition temperature passes through a maximum for the tempering temperature of 250°C.
3. A minimum in the liquid nitrogen fracture energy occurs for this tempering temperature.

This latter point is also shown in Figures 23 and 24 which give plots of CVN energy as a function of tempering

temperature for the two Mn and Si-free lab heats (B7 and 840). As noted earlier, tests at room temperature show no trough for either 840 or B7, but the trough appears in the tests at 77°K. The general level of fracture energy is reduced at 77°K, as expected, at all tempering temperatures and the minimum in the curve occurs around 250°C in both the heats.

Extensive fractographic studies were done with the scanning electron microscope on the fracture surfaces of broken Charpy bars. Figure 25 shows the results of the specimens tempered at 200°, 250°, and 300°C, i.e., in the vicinity of the minimum fracture energy at 77K for B7. For the 200°C tempering condition (Fig. 25a) i.e. to the left of the minimum, the fracture mode is mostly transgranular cleavage, with a bit of rupture. For the 250°C tempering condition (Fig. 25b) i.e. at the minimum of the trough, a considerable amount of intergranular fracture (approx. 20-25%) can be seen mixed with cleavage and rupture. For the 300°C tempering condition (Fig. 25c) i.e. above the minimum, less intergranular fracture and larger cleavage facets can be observed, along with rupture. Figure 26 shows the Auger spectrum from the intergranular fracture surface of steel B7, fractured in the Auger system in pure hydrogen. It is definite that the presence of S has been detected on prior austenite grain boundaries. Thus, even in this pure steel (B7) with only 30 ppm phosphorus and 30 ppm

sulfur, there is apparently enough impurity segregation (presumably during austenitization) to give an observable amount of TME if the test is done below the transition temperature. The segregation of sulfur on the prior austenite grain boundaries was also observed by Briant and Banerji(39) in a "pure" 3.5 Ni, 1.7 Cr steel.

(B) Commercial 4340-type Steels

The effect of test temperature with respect to the transition temperature⁽⁶⁾ shows up in the commercial steel as well. Figure 27 shows the results of Charpy tests over a wide range of temperatures for commercial steel B2. The figure shows that room temperature is in the transition range for 350°C tempering condition, but not for 250°C tempering condition. Hence, it is obvious that a trough in Charpy energy is observed at all temperatures between liquid nitrogen and room temperature because the 350°C specimen is still somewhat below its upper energy shelf at room temperature. This is illustrated in Figure 28. The TME troughs, with minima in the range 300-350°C, occur for both test temperatures. At 77°K, the level of fracture energy is decreased once again at all tempering temperatures, and there is simply a downward shift in the entire energy curve. Comparing the fracture appearance of the 350°C specimens, as shown in Figure 29, more intergranular fracture can be observed when tested at 77°K.

The shift in transition temperature due to 350°C vs. 250°C tempering in steel B6 (Pure + Mn + Si) is shown in Figure 30. Again, it is obvious that a trough should be observed at all temperatures between room temperature and 77°K for 350°C tempering condition, because the specimen tempered at 350°C is still below the upper energy shelf at room temperature. The changes in fracture mode in these specimens are summarized in Figure 31.

Two points are to be noted here:

1. When the steel is unembrittled (250°C tempering condition), hardly any intergranular fracture is observed at 77K. When the steel is embrittled (350°C temper), we see a significant amount of intergranular fracture even at room temperature.
2. For the 350°C tempering condition, not only the amount of intergranular fracture is increased, but we also get more cleavage fracture.

Presumably, the controlling factor in the toughness of the 350°C specimens is the incidence of intergranular fracture. This itself may lead to cleavage fracture, because an intergranular microcrack provides a local stress intensification sufficient to produce cleavage fracture under the right conditions of temperature and strain rate.

As stated earlier, tempered martensite embrittlement has been considered to be either impurity-induced intergranular fracture triggered by carbides formed during

tempering or only carbide-induced transgranular cleavage fracture. As indicated already, this work consistently supports the former position. To examine further the latter position, taken recently by King et al(23) and others(25), low temperature Charpy impact tests were done on a plain carbon steel. The conventional heat treatment was modified by cooling the oil quenched samples to liquid nitrogen temperature before tempering. This was done to eliminate the possibility of the retention of a large amount of retained austenite. Figure 32 shows the plot of CVN energy as a function of tempering temperature for a plain carbon steel SAE 1064. The trough associated with TME is also observed at 350°C. Figure 33 shows the results of scanning electron microscopy of the fracture surface of the specimen tempered at 350°C, i.e., at the minimum of the trough. Here, again, intergranular fracture is observed just below the notch root. There is no doubt that this steel is very prone to cleavage fracture, but the results on the refrigerated specimens are still consistent with the impurity-induced-intergranular-fracture hypothesis.

Experiments have been done on a series of steels with varying contents of Mn, Si, P and S, as noted earlier (Fig. 19). Figure 34 shows how the magnitude of the Charpy energy trough increases with the value of a composition parameter $Mn + 0.5 Si + P + S$ (in weight percent). These results can be interpreted as a reflection

of the tendency for phosphorus and sulfur segregation on the prior austenite grain boundaries. This is supported by the Auger analyses of these steels. Figures 35 and 36 show the Auger spectra from the intergranular fracture surfaces of steels B2 and 842 fractured in pure hydrogen in a UHV system using a grazing incidence primary beam. The presence of both phosphorus and sulfur was detected on prior austenite grain boundaries. In these ultra-high strength steels small amounts of segregated P and/or S are apparently enough to decrease the strength of grain boundaries in these steels. The P and S concentrations indicated in Figures 35 and 36 are only of the order of one percent of a monolayer.

Four-Point Bend Tests

Tempered martensite embrittlement can also be studied by four-point bend tests of notched specimens, in conjunction with the finite element elastic-plastic stress and strain analysis developed by Griffiths and Owen(32). This gives the maximum principal stress σ_{22} ahead of the notch and the maximum principal strain at the notch root as a function of nominal bending stress, both expressed as fractions of the tensile yield stress. Hence, to use this analysis one must first know the yield stress at each tempering temperature. Figure 37 shows the variations of yield stress with tempering temperature for two different test temperatures. The 0.2 pct offset criterion was used to define yielding. As expected, all the steels

follow essentially the same curve, and the yield stress decreased gradually with tempering temperature for both test temperatures.

Room Temperature Tests

At room temperature, although the fracture of the notched, four-point bend specimens appeared to be macroscopically brittle (as observed from the load-deflection curve), the scanning electron microscopy of the fracture surface showed that the fracture mode was rupture at the notch root. If fracture initiated there by rupture, then the strain at the notch root is more relevant than the stress. Figure 38 shows the calculated notch root strain at failure for two vacuum melted lab heats B7 and B6 and the one commercial heat B2 as a function of tempering temperature.

Two points are to be noted here:

1. Troughs appear for steels B2 and B6, but not for B7; this is consistent with the Charpy results.
2. The strain at failure in the air-melted steel B2 is much lower than the vacuum-melted steels B7 and B6.

Figures 39 and 40 which show the scanning electron micrographs of the fracture surfaces of steels B2 and B6 tempered at 350°C, help us to understand both of these points.

The lower micrograph (Figure 39a) taken from steel B2 shows the region just below the notch root where failure initiated. The fracture appears to have initiated by

rupture or microvoid coalescence; note the rupture cavities formed around the large inclusions. Rupture also occurred at the same location in the steel B6 tempered at 350°C (Figure 39b), but the cavities were much smaller than steel B2. Of course, this is a reflection of the different inclusion contents between B6 and B2, as shown previously in Figure 18. Obviously, the strain to initiate failure is very sensitive to the inclusion content. This effect shows up more clearly in the four-point bend tests (Figure 38) than the Charpy test (Figure 17). Now, Figure 40 shows the region of steel B2 just ahead of the initial rupture. Here, the fracture mode has switched to become partly intergranular. This is schematically illustrated in Figure 41. Presumably, the elevation of local stress due to the rupture "crack" was sufficient to cause intergranular fracture. Hence, it appears that this is what gives the trough in fracture strain in the four-point bend tests. The absence of the trough in steel B7 is presumably due to the fact that the propagation of failure by rupture is not interrupted by intergranular cracking, which is a stress controlled, low-strain, low energy fracture mode. Thus, at room temperature it is the strain at the notch root which is more important than the stress, and this is what ultimately controls the fracture mechanism.

77°K Four-Point Bend Test

When the four-point bend tests were done at 77°K,

rather than room temperature, brittle fracture occurred right at the notch root, without any prior rupture. Figure 42 shows the critical local fracture stress, σ^* , necessary for the formation of a brittle crack for the above three steels as a function of tempering temperature.

Several points are to be noted here:

1. Troughs occur for all three steels, which is again consistent with the Charpy results.
2. The stress to initiate failure in the case of the pure steel B7 is much higher than in the other two steels B2 and B6. This reflects the lower tendency toward intergranular fracture in steel B7, presumably due to the absence of Mn and Si and hence, a decrease in the amount of the impurities P and S on the grain boundaries.
3. In the as-quenched condition (when there is no carbide on the grain boundaries) there is a big difference in σ^* between B7, B6, and B2. The difference between steels B7 and B6 presumably due to the difference in the amount of impurities on the grain boundaries. The difference between lab heat B6 and steel B2 presumably reflects not only a further increase in impurity concentration on grain boundaries, but also the difference in the inclusion content between the two steels.

The results of careful scanning electron microscopy on the fracture surfaces of the 350°C tempered specimens is shown in Figure 43. The following observations are important:

1. In all these three types of steels, the tempered martensite embrittlement trough is associated with the occurrence of intergranular fracture.
2. Steel B7 shows the least amount of intergranular fracture.
3. The commercial steel B2 shows the most intergranular fracture.
4. The steel B6 shows quite a few intergranular facets, but fewer than B2.

Referring back to Fig. 42, we can observe a large drop in σ^* with tempering temperature in all three steels. Now, the question is whether this drop is due to an impurity-induced intergranular fracture problem triggered by carbides formed on the grain boundaries during tempering or due to the formation of extra-large carbides, e.g., from an unusually large amount of retained austenite, which would make cleavage fracture easier. Figures 44a, b, c, d, and e show the results of scanning electron microscopy of the fracture surfaces of the specimens for the as-quenched, 150°C, 250°C, 350°C, and 450°C tempered conditions, respectively for steel B7. We can observe more and more intergranular facets as we go from as-quenched to 350°C tempered

condition. The measured amounts of intergranular fracture are shown in Figure 45. As the critical local fracture stress (σ^*) decreases, the percent intergranular fracture increases and it passes through a maximum corresponding to the bottom of the trough (at 350°C). Hence, this supports the viewpoint that the phenomenon of tempered martensite embrittlement is due mainly to the grain boundary weakening by segregated phosphorus and sulfur and it is triggered by carbide formation at tempering temperatures above 150°C. Figure 46 shows the carbon extracton replicas of steel B6 showing the grain boundary carbides at various stages of tempering. As may be seen from this figure, as we go to higher and higher tempering temperature, we get more and more carbides on the grain boundaries. Note that at 150°C tempering condition (magnified six times), we can observe extremely thin carbide platelets on the grain boundaries. These may be thin ϵ -carbides which are known to form at this temperature. When we have grain boundaries which are already weakened by the impurities, presumably during austenization; this increase in the amount of carbides helps in cracking open more and more grain boundaries by providing effective slip barriers and hence an increase in the amount of intergranular fracture.

In order to study the role of retained austenite, measurements of retained austenite were done by the

magnetic saturation method. Figure 47 shows the variation of the percent retained austenite with tempering temperature for three different types of steels. The precision of the measurements is indicated by the duplicate measurements on steel B6. The pure steel B7 shows the least amount of retained austenite at all tempering temperatures. However, as may be seen from Figure 42, this steel shows the highest toughness. According to one point of view⁽²⁴⁾, these retained austenite films, if stable, are beneficial to fracture toughness and the tempered martensite embrittlement is caused mainly by the decomposition of this interlath retained austenite to carbides on subsequent tempering. The fracture is supposed to occur mainly by quasi-cleavage along the martensitic lath/packet boundaries. However, this is not consistent with the present observations: the pure steel (B7) with the least amount of retained austenite at all tempering conditions shows the highest toughness, and the amount of intergranular fracture increases with tempering temperature. Hence, the amount of retained austenite, itself, cannot control the embrittlement mechanism. The larger amounts of retained austenite in steels B2 and B6 are presumably a reflection of the presence of manganese in these steels. Also, the increase in percent non-magnetic phase above 350°C tempering temperature is presumably due to the formation of some alloy carbides, which are mainly paramagnetic in nature^(40,41,42).

Finally, Figure 48 shows how the critical local fracture stress σ^* at 77°K changes with the composition parameter ($Mn + 0.5Si + S + P$) for various types of steels. The σ^* value characteristic of brittle fracture drops drastically as the bulk Mn, Si, P, S in the steel increases. These results presumably reflect the tendency of phosphorus and sulfur segregation on the grain boundaries by Mn and/or Si.

DISCUSSION

Tempered Martensite Embrittlement

In general, tempered martensite embrittlement can be characterized as follows:

1. By a minimum, or trough, in the room temperature Charpy fracture energy (Figures 17 and 19) when the as-quenched (martensitic) steel is tempered in the vicinity of $300^\circ\text{C} \pm 50^\circ\text{C}$.
2. By a maximum in the ductile-to-brittle transition temperature corresponding to the minimum in the toughness curve (Figure 22).
3. By a minimum in the room temperature fracture strain (ϵ_f^*) at 350°C (Figure 38) where the fracture actually initiates by initial ductile rupture and then switches to partly intergranular fracture.
4. By a minimum in the critical local fracture stress (σ^*) at 77K (Figure 42) where brittle, partly

intergranular fracture occurs right at the notch root.

Whatever the manifestation of tempered martensite embrittlement, some of the key observations can be summarized as follows:

1. The room temperature toughness troughs are absent for the Mn-and Si-free lab heats B7 and 840. However, when the tests are done at 77°K, we do see a small trough even for these pure heats (Figures 23 and 24).
2. An increase in the bulk Mn, Si, P and S contents of the steel, which is empirically represented as $(Mn + 0.5 Si + P + S)$, increases the depth of the trough (that is, RTCFE) indicating that the steel is more and more embrittled (Figure 34).
3. The TME troughs are always associated with intergranular fracture, the amount of which increases as we go from pure steel B7 to commercial steel B2 (Figure 43).
4. As the tempering temperature is increased, more and more carbides precipitate on the grain boundaries (Figure 46) and this corresponds to a gradual increase in the amount of intergranular fracture, the maximum being at the bottom of the trough (Figure 45).
5. Auger spectra from intergranular fracture surfaces (produced in pure hydrogen) show the segregation of

both phosphorus and sulfur on the prior austenite grain boundaries (Figures 26, 35 and 36).

Effects of Mn and Si

From the observations above, it appears that the principal role of Mn and Si is to promote the segregation of phosphorus and sulfur to the grain boundaries, even though the steel contains very low P and S(13,17,18).

It is well known that S is an extremely potent embrittling element in iron and its alloys⁽⁴³⁾, and such a role of S in the present case is also compatible with the observed effects of Mn and Si. As with phosphorus, Mn interacts attractively⁽³⁸⁾, and Si interacts repulsively, with S in iron⁽⁴⁴⁾. The interaction coefficients in liquid iron are compared in Table III.

TABLE III
Interaction Coefficients for Solutes
in Iron at 1873°K (Ref. 44)

	Mn	Si
P	*	8.6
S	-4.3	5.7

*Not available, but presumably negative

From Guttmann's ternary regular solution model^(4,45), which has been later expanded by Yu et al.(17,18) for a multicomponent system, a Guttmann-type expression for G_p

can be written as:

$$\Delta G_P = \Delta G_P^o + 2\alpha_{Fe-P}^B (X_P - X_P^\phi) + \alpha'_{Cr-P}^B (X_{Cr} - X_{Cr}^\phi)$$

$$+ \alpha'_{Mo-P}^B (X_{Mo} - X_{Mo}^\phi) + \alpha'_{Ni-P}^B (X_{Ni} - X_{Ni}^\phi)$$

$$+ \alpha'_{Mn-P}^B (X_{Mn} - X_{Mn}^\phi) + \alpha'_{Si-P}^B (X_{Si} - X_{Si}^\phi)$$

The first term ΔG_P^o is the free energy of segregation of phosphorus in an Fe-P binary alloy and is large because phosphorus is highly surface active in iron. The second term produces a negative effect on ΔG_P because $(X_P - X_P^\phi)$ is negative (since phosphorus is expected to segregate to the grain boundary) and α_{Fe-P} is positive. The other elements such as chromium, molybdenum, nickel and manganese have moderate-to-strong interactions with phosphorus and hence they are expected to co-segregate with P. Thus, they add separately to increase ΔG_P . Silicon interacts repulsively with phosphorus in iron (Cf. Table III); hence α'_{Si-P} is negative. The term $(X_{Si} - X_{Si}^\phi)$ is also negative because silicon is repelled from the interface by phosphorus. Therefore, silicon also adds an increment to G_P .

Similarly, the expression for ΔG_S for sulfur can be written as:

$$\Delta G_S = \Delta G_S^o + 2\alpha_{Fe-S}^B (X_S - X_S^\phi) + \alpha'_{Cr-S}^B (X_{Cr} - X_{Cr}^\phi)$$

$$+ \alpha'_{Mo-S}^B (X_{Mo} - X_{Mo}^\phi) + \alpha'_{Ni-S}^B (X_{Ni} - X_{Ni}^\phi)$$

$$+ \alpha'_{Mn-S}^B (X_{Mn} - X_{Mn}^\phi) + \alpha'_{Si-S}^B (X_{Si} - X_{Si}^\phi)$$

It is reasonable to treat sulfur in the same way as phosphorus with respect to its interaction with manganese and silicon. As shown in Table III, manganese has a strong attractive interaction with sulfur and hence α'_{Mn-S} is positive. Thus, it adds to ΔG_S . As with silicon, it interacts repulsively with S. Since the term $(X_{Si}^{\phi} - X_{Si}^B)$ is negative, Si also adds to ΔG_S .

Because of the above effects, any Mn+P or Mn+S that is left in solution after compound formation, would be expected to co-segregate to the grain boundaries. Silicon itself does not co-segregate, but it increases the driving force for segregation of phosphorus and sulfur. Kaneko et al.(46) also demonstrated a fairly strong interaction of Mn and Si with P in γ -Fe containing 12% Ni at 1000°C. This is shown in Figure 49. From their work it might be expected that both Mn and Si will promote the segregation of phosphorus on the prior austenite grain boundaries. Recently, Clayton(38) also reported that in a NiCr steel, the segregation of phosphorus in the austenite phase was increased with an increase of Mn in the steel.

It is concluded, therefore, that the presence of Mn and/or Si increases the susceptibility to tempered martensite embrittlement by promoting the segregation of P and S to the grain boundaries and thus embrittlement of the grain boundaries.

The effect of silicon on the TME characteristics (Heat 842 in Figure 19) shows that the minimum in the energy

curve is pushed to a higher tempering temperature. This is consistent with the observations(13,14) that silicon slows down the kinetics of the tempering process by increasing the ϵ -carbide \rightarrow cementite transformation temperature.

Fracture Micro-Mechanism

Although the room temperature Charpy fracture energy or the transition temperature are widely used as measures of intergranular embrittlement, they have only limited usefulness as far as a fundamental understanding of the fracture micromechanisms is concerned. In Charpy impact tests, a considerable amount of energy is expended in plastic bending prior to brittle fracture initiation. The fracture is often a mixture of intergranular, cleavage, and rupture by microvoid coalescence. Therefore, it is extremely difficult to evaluate which fracture mechanism is dominant at a particular temperature. As discussed before, the method developed by Kameda and McMahon(5,47) in conjunction with the finite element stress and strain analysis developed by Griffiths and Owen (32), helped in understanding more directly the micromechanism for brittle, as well as ductile fracture. As described already in the previous sections, this involved the use of a notched bar loaded in pure bending and estimation of the critical local fracture stress or fracture strain, depending upon which fracture mechanism is dominant.

Strain-Controlled Fracture

It has been shown previously that in the room

temperature four point bend tests, although the fracture appeared to be macroscopically brittle from the load-deflection curve. The fracture actually initiated by rupture or microvoid coalescence at the notch root (Figure 39). Obviously, this type of fracture is a strain-controlled ductile fracture.

The general behavior of this fibrous fracture involves the formation of voids around inclusions or second-phase particles and the subsequent growth of these voids to give final coalescence. The strain and stress profiles ahead of the notch tip are schematically shown in Fig. 50a. The microvoids are generally formed around inclusion particles ahead of the notch tip under the influence of plastic flow, and the growth of these voids is affected by the hydrostatic component of the stress^(48,49,50), as shown schematically in the figure. The initiation of a void around a particle depends very much on the degree to which the particle is bonded to the matrix. For an inclusion such as manganese sulfide, the bonding is weak and the voids can initiate and grow at low plastic strains. Particles such as carbides in steel are bonded strongly with the matrix, and hence large plastic strains are needed before a void can initiate. In most commercial steels, the microstructure contains a mixture of inclusions and carbides produced by tempering of the martensitic matrix. Cox and Low⁽⁵¹⁾ studied the mechanisms of ductile fracture (dimple rupture) in a quenched and

tempered 4340-type steel. They have shown that fracture occurred by nucleation and subsequent growth of voids formed by decohesion of the interface between manganese sulfide inclusions and the matrix. The growth of these inclusion-nucleated large voids was terminated long before coalescence by the development of void sheets that linked the neighbouring sulfide-nucleated voids. These small voids were nucleated by the cementite precipitates in the quenched and tempered structure. Thus, the fracture surface was composed of a number of rather large cavities, formed around the inclusions, with very fine cavities deriving from the carbides as shown in Figure 39a. It was also demonstrated⁽⁵¹⁾ that the level of tensile stress triaxility did not effect the void nucleation, but it greatly increased the rate of void growth.

In the case of the pure steel B7 (Figure 50b), where the density and size of the inclusion particles were very small, we needed a much higher strain for the nucleation and growth of the microvoids. On the other hand, for the commercial air-melted steel B2(Figure 50c), the inclusions were much larger and more numerous (Figures 18 and 39); hence both nucleation and growth of the microvoids took place at much lower strains. This effect shows up more clearly in Figure 38. The trough in fracture strain for B6 and B2 was due to the incidence of intergranular fracture ahead of the initial

rupture, which interrupted the ductile fracture propagation.

Stress-Controlled Fracture

When the tests were done at a low temperature (77K), the fracture initiated by a brittle mode right at the notch root. Since this fracture mode is a stress-controlled, low strain, low energy brittle decohesion, it is the local stress σ^* which controls the fracture micromechanism.

In steel, intergranular brittle fracture occurs by the following three-stage process:

1) Nucleation of an intergranular brittle crack at a hard particle by the blockage of slip (or a twin) which helps in achieving the necessary high local stress and thus at least local yielding is required(52-54). This is shown schematically in Figure 51a.

2) Propagation of this microcrack nucleus beyond the hard particle when the maximum local tensile stress reaches the critical local fracture stress σ^* .
The value of σ^* depends on both cohesive energy (γ) and the plastic work (γ_p).

As shown schematically in Figure 51b, two independent processes occur to propagate the microcrack. One is bond stretching and breaking (requiring an expenditure of the ideal fracture energy γ per unit area) at the microcrack tip, and the other is the plastic work involving energy γ_p due to dislocation motion away from the crack tip because of the shear component of σ^* . The driving force for both these processes is the local applied stress. Although

the plastic work γ_p is the major component of the fracture energy for brittle fracture of an elastic-plastic material^(55,56), it has been recently demonstrated⁽⁵⁷⁾ that a small reduction in γ by impurity segregation leads to a corresponding reduction in the local stress needed for the generation of an accelerating microcrack, and this in turn causes a large reduction in plastic work γ_p because of the exponential relationship between the local applied stress and the plastic strain rate in the region of the microcrack tip. Hence, segregation of impurities to the prior austenite grain boundaries can cause a large reduction in σ^* . Apparently the segregation of impurities occurs during the austenitization treatment^(6,16), and we assume that the nature of carbide precipitation does not change with the composition of the steel (except as noted earlier for the case of Si). The large differences in σ^* corresponding to the bottom of the trough between the pure steel B7 and the other Mn and Si containing steels B6 and B2 (Figure 42) correspond to an increase in the amount of intergranular fracture (Figure 43). This is also reflected by the drastic reduction in σ^* with the increase in bulk Mn, Si, P and S content in the steel as shown previously in Figure 48.

3) Growth of the microcrack to a macroscopically unstable size. This is governed mainly by the following factors: a) Stress gradient ahead of the notch tip.

- b) Size and density of carbides on the grain boundaries.
- c) Extent of embrittlement of the adjacent boundaries.

These are discussed in detail in the following section.

Mechanism of Tempered Martensite Embrittlement

As shown previously in Figure 42, the trough characteristics of tempered martensite embrittlement can be observed for all pure, pure+Mn+Si, and commercial steels for a tempering treatment in the vicinity of 350°C. Now, the question is whether this trough in σ^* is due to the grain boundary weakening by segregated impurities (such as P and S) in conjunction with the carbides formed during tempering or whether it is due to the formation of extra-large carbides, as for example from an unusually large amount of retained austenite, which would make cleavage fracture easier. That is, is it fundamentally an intergranular or a transgranular fracture phenomenon? As indicated already, the present work consistently supports the intergranular fracture hypothesis.

Let us consider a microcrack of length c nucleated at a grain boundary particle and subjected to the maximum stress σ^* (Figure 51b). Inclusion particles are more favourable as crack initiation sites than the grain boundary carbides because of their size effect. The stress intensification at the tip of the microcrack is given by the local stress intensity factor k . This k is defined as the stress intensity that is needed to propagate a microcrack of length c in a stress field

of magnitude σ^* and is given by $k = \sigma^* \sqrt{\pi C}$. To propagate this unstable microcrack, a Griffith-type energy criterion must be satisfied. In other words, the energy of the system must decrease as the microcrack propagates. This means means that(58,59)

$$E = -\frac{k^2}{2G} (1-\gamma) + 2\gamma + \gamma_p(k) \leq 0 \quad (1)$$

which is superficially similar to the Orowan(60) modification of the Griffith criterion(61). However, in this new formulation(58,59) γ_p is not a material constant, but a function of the local stress intensity k which is, in turn, a function of γ . Jokl et al.(58,59) calculated the dependence of the energy E on k for several values of γ which is shown in Figure 52. For a value $k = k_G$ for which $E = 0$ (as shown in the figure), the microcrack becomes unstable. The uppermost curve corresponds to a case where such an instability does not occur and hence the material behaves in a ductile manner. The figure also indicates that the existence of k_G (that is whether a material will behave in a ductile or brittle manner) depends on the value of γ , which in turn, depends on the extent of impurity segregation. A decrease in γ due to impurity segregation can convert a ductile material to a brittle material, as shown in Figure 52.

In the as-quenched condition, when there are no carbides on the grain boundaries (Figure 46a), and we need a much higher stress σ^* for a microcrack to propagate; hence, only

a few grain boundaries which have relatively large impurity concentrations (or relatively large inclusions) are cracked. With subsequent tempering, more and more carbides precipitate on the already weakened grain boundaries (Figures 46b,c, d and e). This results in an increasingly dense population of carbides around the microcrack nucleated at an inclusion particle. This is shown in Figs. 53b, and 53c. These fine carbides can also act as hard particles and can be cracked by the stress field of the approaching microcrack front and can start new microcracks that are later overtaken by the main crack. Therefore, these carbides act as "kickers" by accelerating the crack velocity, since the crack front loses less energy while passing these carbides. This provides an easier path for crack propagation and thus higher probability for further propagation. As the effective crack size increases, the crack velocity becomes so high that it can overcome even larger values of γ_p , and thus makes final fracture more probable.

Effect of Test Temperature

It had been shown previously that the room temperature Charpy fracture energy did not show any trough for steel B7, but it did for the Mn+Si-containing steel B6 and the commercial steel B2. However, when the tests were done at 77K, even the pure steel showed a small trough which was associated with some intergranular fracture. This signifies the importance of test temperature for the observation of tempered martensite embrittlement.

In the case of steel B7, where the grain boundaries are less contaminated, mere carbide precipitation during tempering cannot raise the ductile-brittle transition temperature above room temperature (Figure 22); hence, the room temperature Charpy fracture energy does not exhibit any trough, and the fracture takes place entirely by rupture or microvoid coalescence for all tempering conditions.

When an impure steel is embrittled (350°C tempering condition), that is, when both impurities and carbides are present on the grain boundaries, room temperature is generally below the ductile-brittle transition temperature or is in the transition region (Figures 27 and 30); hence, this can lead to an anomalously low room temperature toughness. Therefore, the observation of tempered martensite embrittlement depends on the test temperature. The test temperature has to be in or below the transition temperature range for the 350°C tempering condition; otherwise the embrittlement trough will not be observed.

Recently, a lot of attention has been given to the role of retained austenite and its thermal decomposition to interlath carbide during tempering as a possible mechanism for tempered martensite embrittlement(24-26). It has been thought(24) that fracture can be intergranular with respect to the prior austenite and that retained austenite, if stable, could be beneficial to toughness.

This is because the austenite phase is f.c.c. and therefore has a very high resistance to cleavage; hence, a lot of dislocations are generated at the tip of the brittle microcrack. This makes it even more difficult for a brittle crack to propagate. Now, consider the as-quenched condition, where a brittle microcrack is presumably formed only at a large second phase particle. The steel with the highest stress than a steel with a lower amount of retained austenite. Considering Figure 47, it may be seen that steel B7 shows the lowest amount of retained austenite in the as-quenched condition. However, compared with Figure 42 it may be seen that this steel with the lowest amount of retained austenite shows the highest toughness. The same effect continues to be observed when the steels are tempered at increasingly high temperatures. If the toughness of the steel is controlled by the retained austenite, we would expect the opposite effect. Also, if grain boundary impurities do not play any important role, no satisfactory explanation could be given for the increase in the percent intergranular fracture as we go from pure to commercial steel (Figure 43).

It has been suggested by King, Smith and Knott(23), that tempered martensite embrittlement is essentially a carbide-induced transgranular (cleavage) problem, and that the transgranular cleavage fracture appeared to run across martensite packets rather than along prior

austenite grain boundaries. However, as shown in the previous chapter, even in a plain carbon steel (SAE 1064) which was refrigerated after oil quenching (to eliminate the possibility of a large amount of retained austenite), the trough was associated with intergranular fracture at the notch root (Figure 33).

Therefore, from the present observations along with those of Briant and Banerji⁽⁶⁾, it appears that the tempered martensite embrittlement in the steels studied here is mainly due to the grain boundary weakening by impurity elements, combined with intergranular carbides formed during tempering. This is supported by the Auger data which shows evidence of the segregation of P and S on the prior austenite grain boundaries and the measurements of σ^* which show their effects directly on the intergranular strength. Carbide formation, by either tempering or decomposition of retained austenite, is a necessary but not sufficient condition.

It cannot be denied that in extreme cases^(25,26) when there is an unusually large amount of retained austenite (as in the case of air-cooled or isothermally transformed materials), the formation of coarse carbides can accentuate the Charpy energy and fracture toughness troughs. It appears, however, that this is a special case and is peripheral to the main issue. Generally speaking, the problem of tempered martensite embrittlement is viewed as a loss in toughness which is associated with

the incidence of intergranular fracture when the as-quenched martensitic matrix is tempered to retain both toughness and strength. The trough that is normally observed is not large. The enormous loss in toughness resulting from tempering of air-cooled or isothermally transformed product should not be viewed as the same problem, because the basic microstructure in this case is different from that obtained in the as-quenched condition. Therefore, it seems that the latter case is simply a superimposition of a different phenomenon (namely the decomposition of large amounts of retained austenite into coarse carbides) on the basic phenomenon of "normal" tempered martensite embrittlement.

SUMMARY AND CONCLUSIONS

1. Tempered martensite embrittlement is essentially a grain boundary impurity-induced embrittlement problem and is triggered by carbides formed during the tempering process. Carbide formation is a necessary, but not sufficient, condition for this type of embrittlement.
2. The important impurity elements are phosphorus and sulfur, since they segregate to the prior austenite grain boundaries during austenitization. Only a small amount of this impurity segregation is sufficient to cause embrittlement in ultra-high strength steels.

3. The characteristic trough and concomitant intergranular fracture indicative of tempered martensite embrittlement were observed to varying degrees in all the steels investigated when they were tested below their ductile-brittle transition temperature.
4. At room temperature, where the fracture initiates by rupture or microvoid coalescence, it is the strain which controls the micromechanism of fracture initiation. At low temperature where the fracture initiation occurs by a brittle mode, it is the local stress which controls the initiation micromechanism.

REFERENCES

1. Recent review: C. L. Briant and S. K. Banerji, Int. Metals Reviews, 1978, No. 4, Vol. 23, p. 164.
2. E. C. Bain and H. W. Paxton; Alloying Elements in Steels, ASM, 1966.
3. S. K. Banerji, C. J. McMahon, Jr., and H. C. Feng; Met. Trans., vol. 9A, 1978, p. 237.
4. C. J. McMahon, Jr. and L. Marchut; J. Vac. Sci. Tech; Vol 15, No. 2, 1978, p. 450.
5. J. Kameda, and C. J. McMahon, Jr.; Met. Trans., Vol. 11A, 1980, p. 91.
6. C. L. Briant, and S. K. Banerji; Met. Trans., Vol. 10A, 1979, p. 1729.
7. L. J. Klingler, W. J. Barnett, R. P. Frohmberg and A. R. Troiano; Trans. ASM, Vol. 46, p. 1557, 1954.
8. R. L. Rickett and J. M. Hodge; Proc. ASTM, 1951, Vol. 51, p. 931.
9. M. A. Grossman; Trans. AIME, 1946, Vol. 167, p. 39.
10. B. S. Lement, B. L. Averbach, and M. Cohen; Trans. ASM, Vol. 46, 1954, p. 851.
11. H. Schrader, H. J. Wiester, and H. Shiepmann; Archiv Eisenhuttenwesen, Vol. 21, 1950, p. 21-27.
12. J. M. Capus, and G. Mayer; Metallurgia, Vol. 62, 1960, p. 133; J. Iron Steel Inst., Vol. 196, 1958, p. 1255; J. Iron Steel Inst., Vol. 201, 1963, p 201.
13. A. G. Allten, and P. Payson; Trans. ASM, Vol. 45, 1953, p. 498.
14. C. J. Alstetter, M. Cohen, and B. L. Averbach; Trans. ASM, Vol. 55, 1962, p. 287.
15. B. J. Schulz, and C. J. McMahon, Jr.; in "Temper Embrittlement of Alloy Steels", ASTM STP 499, ASTM, 1972, p. 104-135.
16. C. L. Briant, and S. K. Banerji; Met. Trans., Vol. 10A, 1979, p. 123.
17. J. Yu, and C. J. McMahon, Jr.; Met. Trans., Vol. 11A, 1980, p. 277.

Page 2.
REFERENCES

18. J. Yu; Ph.D Thesis, University of Pennsylvania, 1979.
19. C. J. McMahon, Jr.; Met. Sci. and Eng., Vol. 42, 1980, p. 215-226.
20. E. B. Kula, and A. A. Anctil; J. of Matls., ASTM, Vol. 4, 1969, p. 817.
21. J. R. Rellick, and C. J. McMahon, Jr.; Met. Trans., Vol. 5, 1974, p. 2439.
22. C. J. McMahon, Jr.; Grain Boundaries in Engineering Materials, Proc. 4th Bolton Landing Conference, June, 1974, p. 525, ed. J. L. Walter, J. H. Westbrook, D. A. Woodford.
23. J. E. King, R. F. Smith, and J. F. Knott; Proc. Fourth Int. conf. on Fracture, Waterloo, Vol. 2, ICF4, 1977, p. 279.
24. G. Thomas; Met. Trans.; Vol. 9A, 1978, p. 439.
25. R. M. Horn, and R. Ritchie; Met. Trans., Vol. 9A, 1978, p. 1039.
26. R. M. Horn, and R. Ritchie; Proc. 106th Annual AIME Meeting, Atlanta, March 1977.
27. J. P. Materkowsky, and G. Krauss; Met. Trans., Vol. 10A, 1979, p. 1643.
28. J. McMahon, and G. Thomas; Proc. Int. Conf. on The Micro-structure and Design of Alloys, Cambridge, Vol. 1, p. 180, Inst. of Metals, London, 1973.
29. C. Zapffe, and C. Sims; Trans AIME, Vol. 145, 1941, p. 225.
30. S. K. Banerji and C. J. McMahon, Jr.; Final Progress Report Submitted to Naval Air Systems Command Under Contract No. N00019-75-C-0125, Oct. 1, 1975.
31. 1973 ASTM Standard, part 31, E23-72, p. 277.
32. J. R. Griffiths and D. R. Owen; J. Mech. Phys. Solids, Vol. 19, 1971, p. 419.
33. "Plain-Strain Fracture Toughness of Metallic Materials", ASTM Specification E399.
34. S. R. Novak and S. T. Rolfe; Journal of Materials, Vo. 4, No. 3, 1969, p. 701.
35. G. A. Dreyer, D. C. Austen, and W. D. Smith; Met. Progress, Vol. 86, 1964, p. 116.
36. Techniques for Electron Microscopy; Edited by Desmond Kay, Blackwell Scientific Publications, Oxford.

Page 3.
REFERENCES

37. Magnetism and Metallurgy; Edited by Ami E. Berkowitz and Eckart Kneller; Vol. 1 Academic Press, 1969. "Direct Current Magnetic Measurements", T. R. McGuire and P. J. Flanders, p. 123.
38. J. Q. Clayton; Ph.D. Thesis, Cambridge University, U. K., 1977.
39. C. L. Briant, and S. K. Banerji; Met. Trans., Vol. 10A, 1979, p. 1151.
40. D. L. Williamson, R. G. Schupmann, J. P. Materkowski, and G. Krauss; Met. Trans., Vol. 10A, 1979, p. 379.
41. Z. Mathalone, M. Ron, and J. Pipman; J. Appl. Phys., Vol. 42, 1971, p. 687.
42. G. LeCaer, A. Simon, A. Lorenzo, and J. M. Genin; Phys. Status Solidi(a), Vol. 6, 1971, p. K97.
43. P. Jolly and C. Goux; Mem. Sci. Rev. Met., Vol. 66, 1969, p. 695.
44. J. F. Elliott, M. Gleiser, and V. Ramakrishna; Thermochemistry of Steelmaking, Vol. II, Addison-Wesley, 1963.
45. M. Guttmann; Surface Sci., Vol. 53, 1975, p. 213.
46. H. Kaneko, T. Nishizawa, K. Tamaki, and A. Tanifuji; J. Japan Inst. of Metals, Vol. 29, 1965, p. 166.
47. J. Kameda, and C. J. McMahon, Jr.; Met. Trans., Vol. 11A, 1980, (in press).
48. K. E. Puttick; Phil Mag., Vol. 4, 1959, p. 964.
49. H. C. Rogers; Trans. Met. Soc. AIME, Vol. 218, 1960, p. 498.
50. J. F. Knott; Fundamentals of Fracture Mechanics, John Wiley & Sons Publisher, New York.
51. T. B. Cox and J. R. Low, Jr.; Met. Trans. A, Vol. 5, 1974, p. 1457.
52. C. Zener; Fracture of Metals, p. 3, ASM, Cleveland, OH, 1948.
53. A. N. Stroh; Adv. Phys., Vol. 6, 1957, p. 418.
54. C. J. McMahon, Jr., and M. Cohen; Acta. Met., Vol. 13, 1965, p. 591.
55. E. Smith; Proc. Conf. on the Physical Basis of Yield and Fracture, The Institute of Physics and the Physical Society, London, 1966, p. 36.

Page 4.
REFERENCES

56. J. F. Knott; Fracture, 1977, Proc. 4th Int. Conf. on Fracture, Waterloo, Canada, 1977, ed. D.M.R. Taplin, Vol. 1, p. 61.
57. C. J. McMahon, Jr., and V. Vitek; Acta Met., Vol. 27, 1979, p. 507.
58. M. L. Jokl, J. Kameda, C. J. McMahon, Jr., and V. Vitek; Metal Sci. 1980, Vol. 14, (in press).
59. M. L. Jokl, V. Vitek, and C. J. McMahon, Jr.; Acta. Met., Vol. 28, 1980, (in press).
60. E. Orowon; Trans. Inst. Engrs. Shipbuilders Scotland, Vol. 89, 1945, p. 165.
61. A. A. Griffith; Phil. Trans. R. Soc., Vol. A221, 1920, p. 163.

Table I: Chemical Compositions (wt%)

<u>Steel</u>	<u>C</u>	<u>Mn</u>	<u>Si</u>	<u>P</u>	<u>S</u>	<u>Ni</u>	<u>Cu</u>	<u>Cr</u>	<u>Mo</u>	<u>Al</u>	<u>V</u>	<u>Ch</u>
840 4340 VIM	0.37	0.02	0.01	0.014	0.003	1.84	0.01	0.82	0.22	<.01	--	--
841 4340 VIM	0.38	0.72	0.01	0.008	0.005	1.83	<.01	0.82	0.26	<.01	--	--
842 4340 VIM	0.38	0.02	0.27	0.0036	0.005	1.82	0.01	0.85	0.30	<.01	--	--
843 4340 VIM	0.36	0.09	0.01	0.012	0.005	1.81	0.01	0.89	0.28	<.01	--	--
846 4340 VIM	0.37	0.23	0.01	0.009	0.005	1.78	<.01	0.83	0.27	<.01	--	--
82 4340 A36	0.39	0.68	0.08	0.009	0.016	1.72	--	0.73	0.22	0.046	0.05	0.04
87 High Purity VIM NiCrMo base	0.37	0.007	0.002	0.003	0.003	1.82	0.002	0.81	0.25	<.001	--	--
86 High Purity VIM 4340	0.37	0.72	0.32	0.003	0.005	1.80	--	0.75	0.26	--	--	--

TABLE II
Austenitizing Temperatures and Grain Sizes

Temperature, °C	ASTM Number	Grain Size (μm)
850°C	8 to 10	13 to 25
1000°C	6 to 7	36 to 51
1150°C	3 to 5	72 to 144

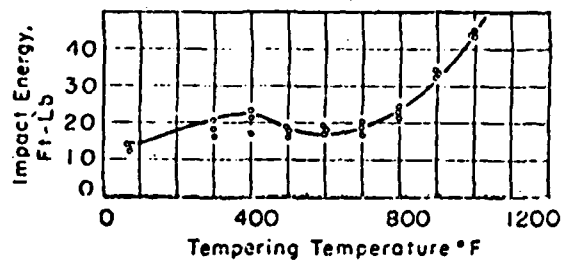


Fig. 1 Room Temperature Impact energy of oil quenched (from 1550°F) 4340 steel as a function of tempering temperature (tempering time 1 hr. at each temperature). (Ref. 7).

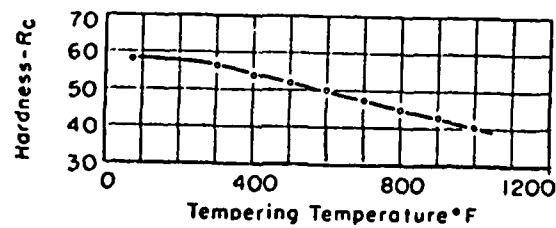


Fig. 2 Hardness for Oil-Quenched (from 1550°F) 4340 steel as a function of tempering temperature (tempering time 1 hr. at each temperature). (Ref. 7).

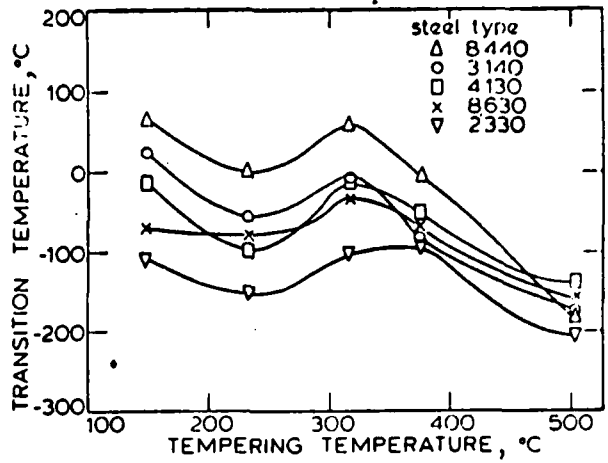


Fig. 3 Variation of ductile-brittle transition temperature as a function of tempering temperature for different types of steels autenitized at 870°C. (Ref. 8,1).

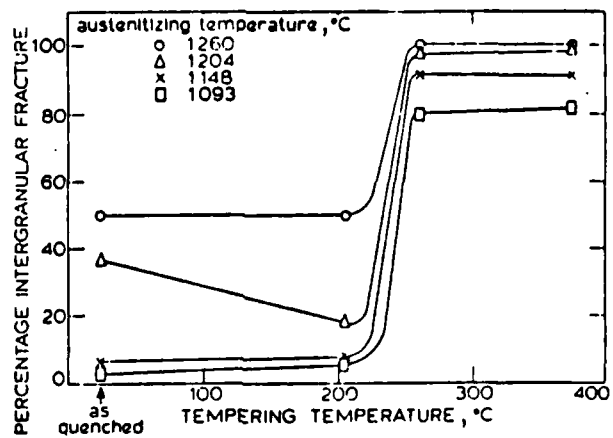


Fig. 4 Change in fracture mode as a function of tempering temperature for different grain sizes. (Ref. 9, 1).

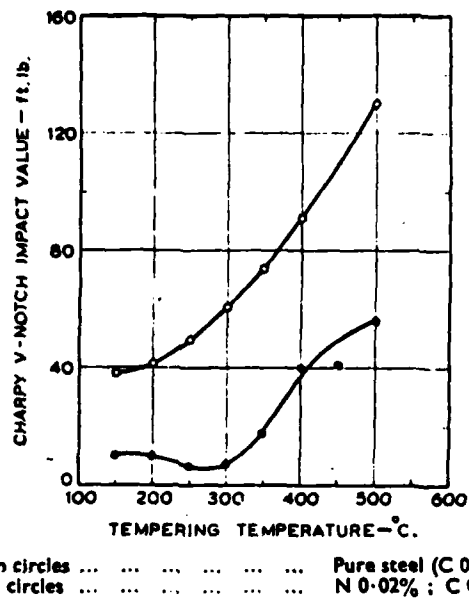


Fig. 5 The influence of impurity element such as N on the impact properties at 20°C of hardened and tempered high purity 3% Ni-Cr steels. (Ref. 12).

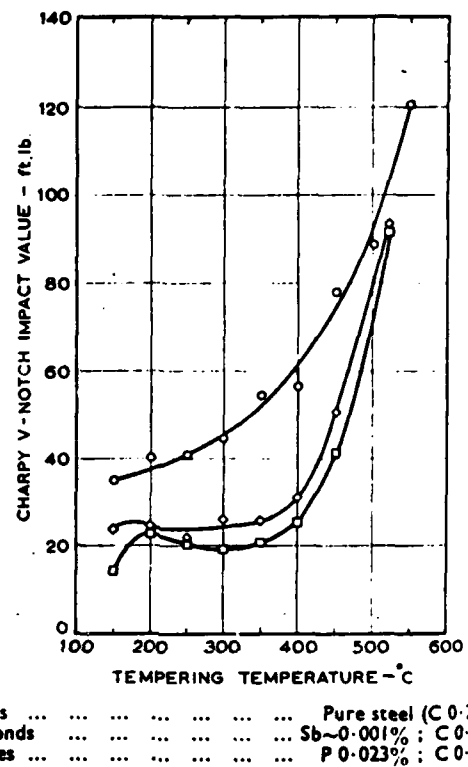


Fig. 6 The influence of impurity elements such as phosphorus and antimony on the impact properties at 20°C of hardened and tempered high-purity base 1.5 Ni-Cr-Mo steels. (Ref. 12).

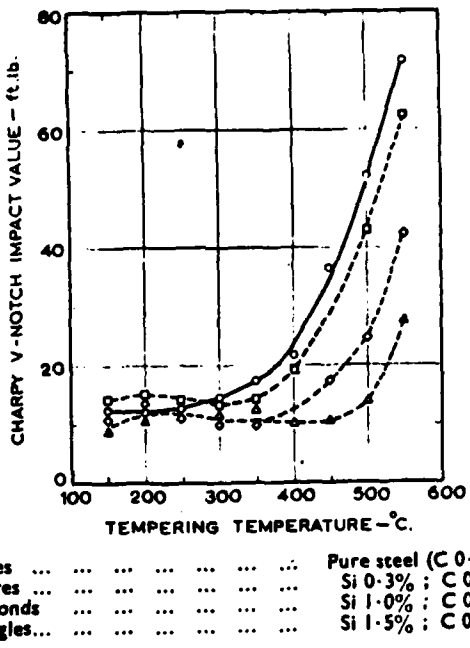
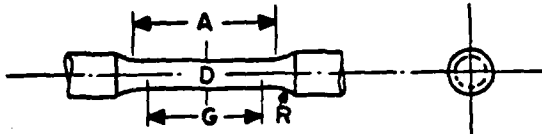


Fig. 7 The influence of silicon on the impact properties at 20°C of hardened and tempered high-purity-base 1.5 Ni-Cr-Mo steels. (Ref. 12).

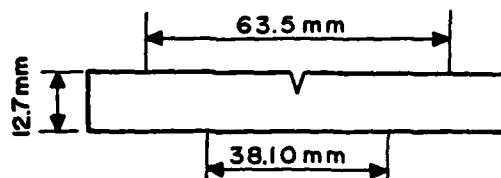
TENSILE SPECIMEN



DIMENSIONS

	in	mm
G - GAGE LENGTH	0.640± 0.005	16.0± 0.10
D - DIAMETER	0.160± 0.003	4.00± 0.08
R - RADIUS OF FILLET	5/32	4
A - LENGTH OF REDUCED SECTION THREADS: 3/8"-16	3/4	20

FOUR-POINT NOTCHED BEND SPECIMEN



NOTCH ROOT RADIUS: 0.25 mm
THICKNESS: 9.525 mm

Fig. 8

The shapes and dimensions of the tensile and four-point notched bend specimens employed under present investigation.

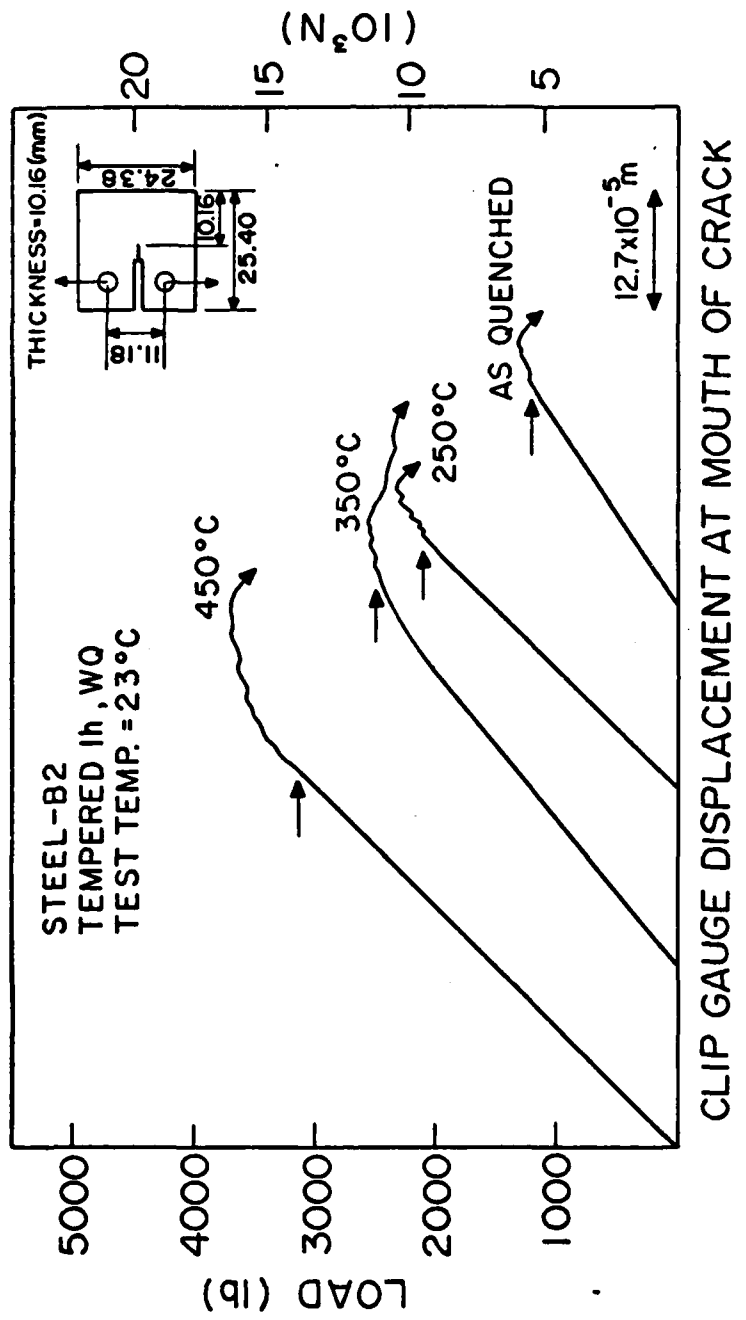
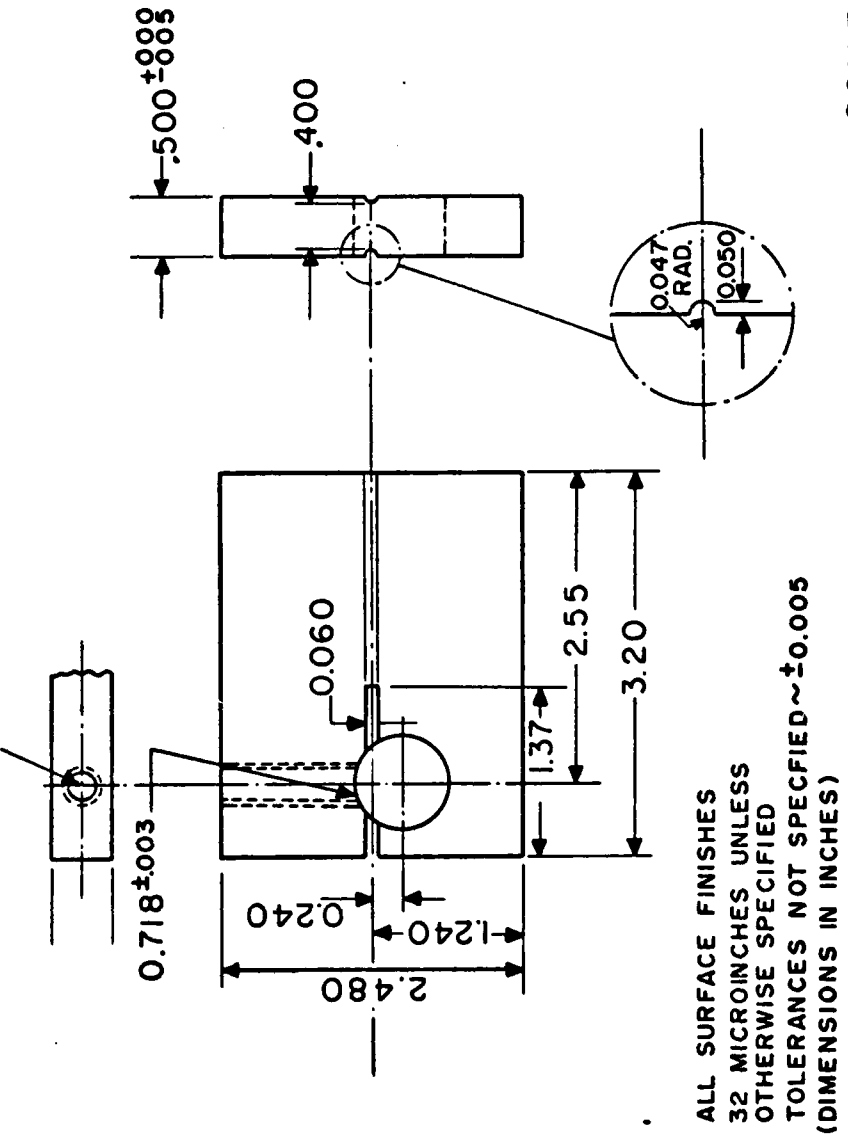


FIG. 9 Load vs. clip gauge displacement curves for precracked specimens, the geometry of which is indicated.

$5\frac{1}{16}$ -18 N.C. W.O.L. SPECIMEN



SCALE : IX

Fig. 10 The shape and dimensions of the wedge-opening-loading (WOL) fracture specimen for determining K_{TH} values in hydrogen. (Ref. 76).

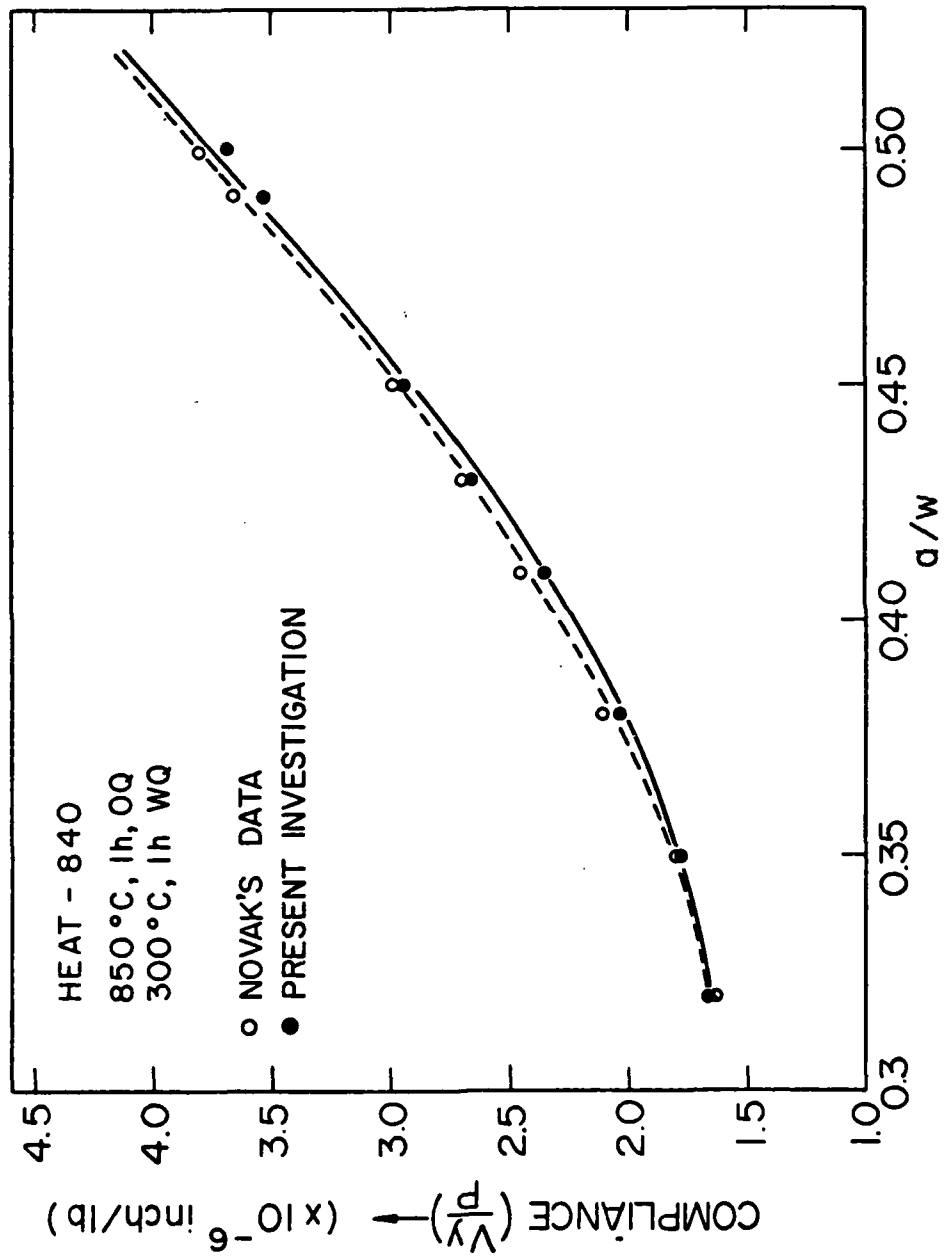
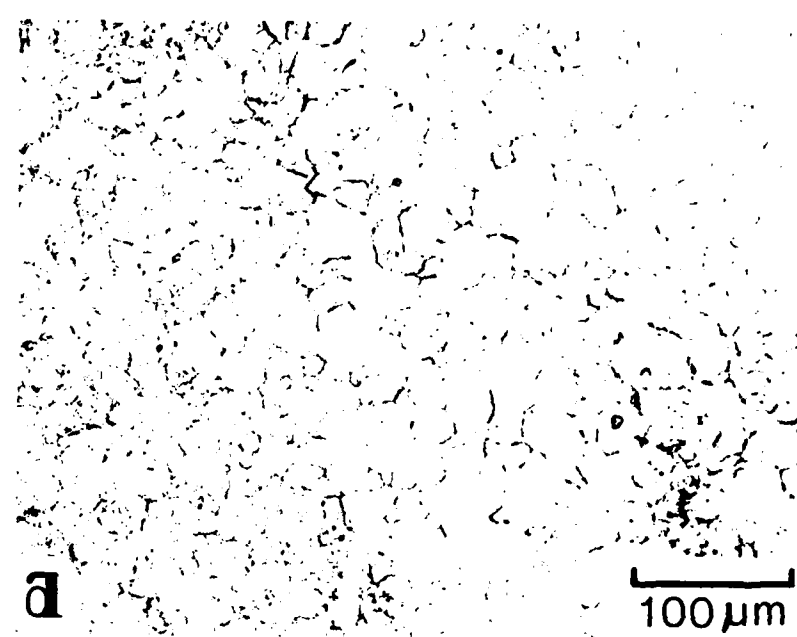


Fig. 11 Experimental compliance calibration for steel 840 and its comparison with compliance calibration of Novak and Rolfe (Ref. 76).

Fig. 12

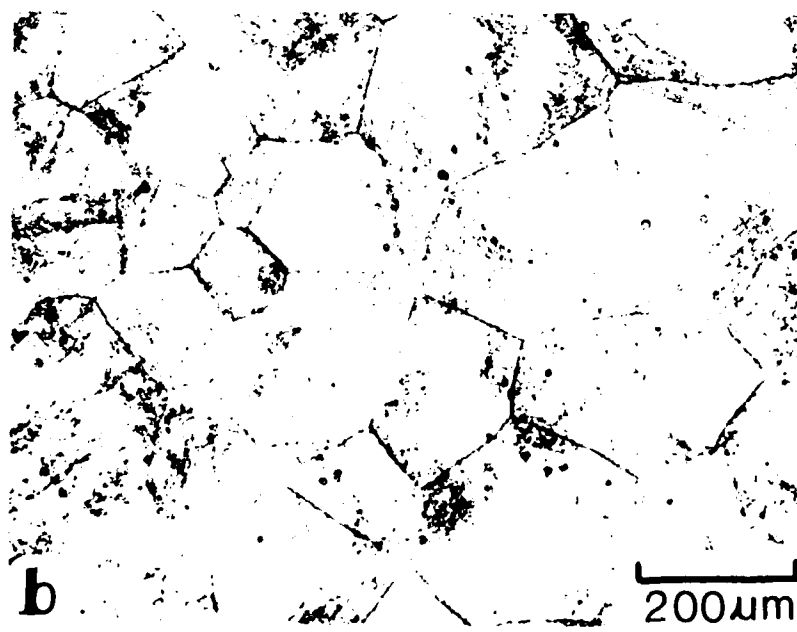
Etched surfaces of the steel 840 revealing prior austenite grain boundaries.

- a) Austenitized for one hour at 850°C followed by oil quenching.
- b) Austenitized for one hour at 1150°C followed by oil quenching.



d

100 μm



b

200 μm

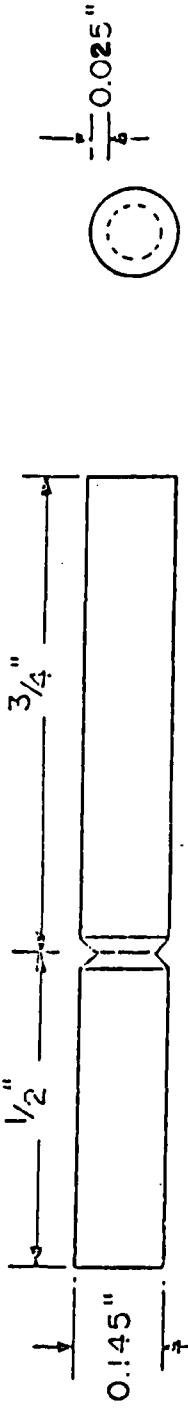


Fig. 13 Specimen geometry for Auger Electron Spectroscopy experiment.

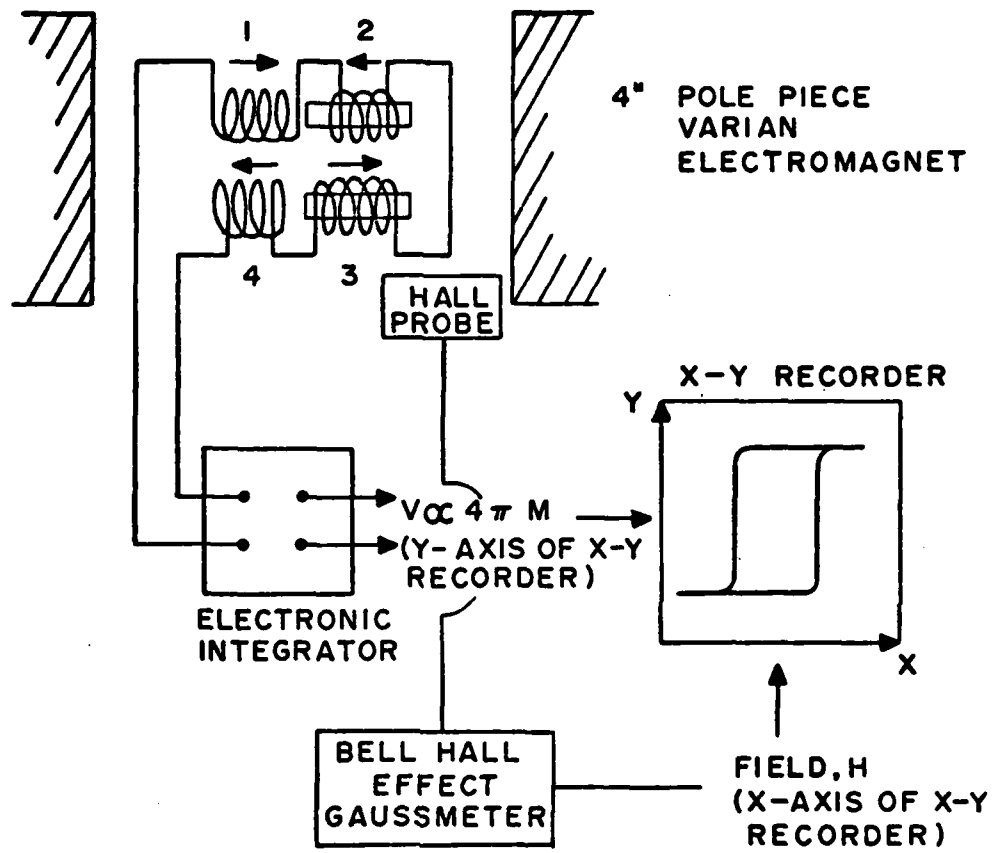


Fig. 15

Schematic representation of the experimental set up used for the measurement of saturation magnetisation.

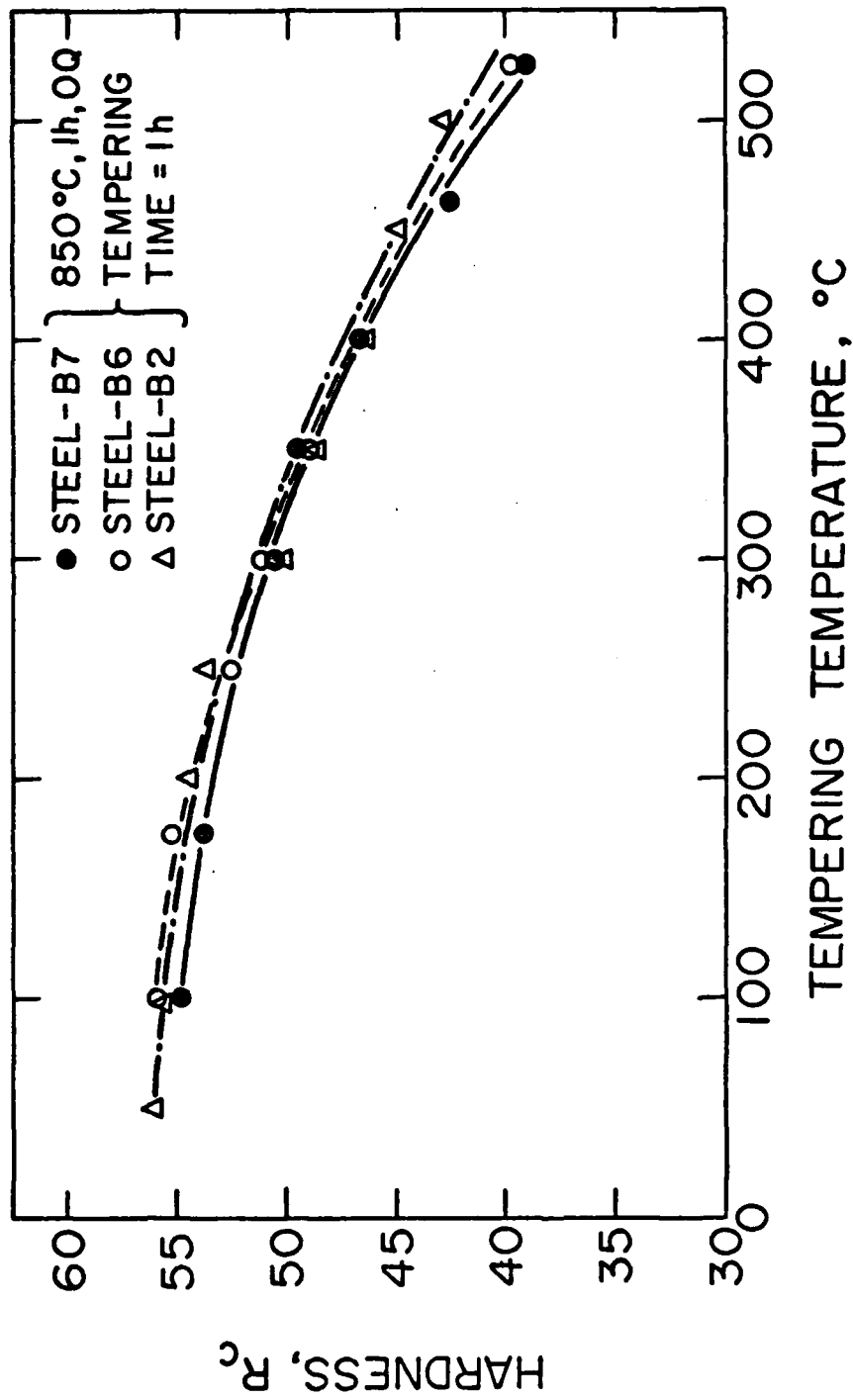


Fig. 16 Variation of hardness with tempering temperature for two vacuum-melted lab heats (B7 and B6) and one air-melted commercial heat B2.

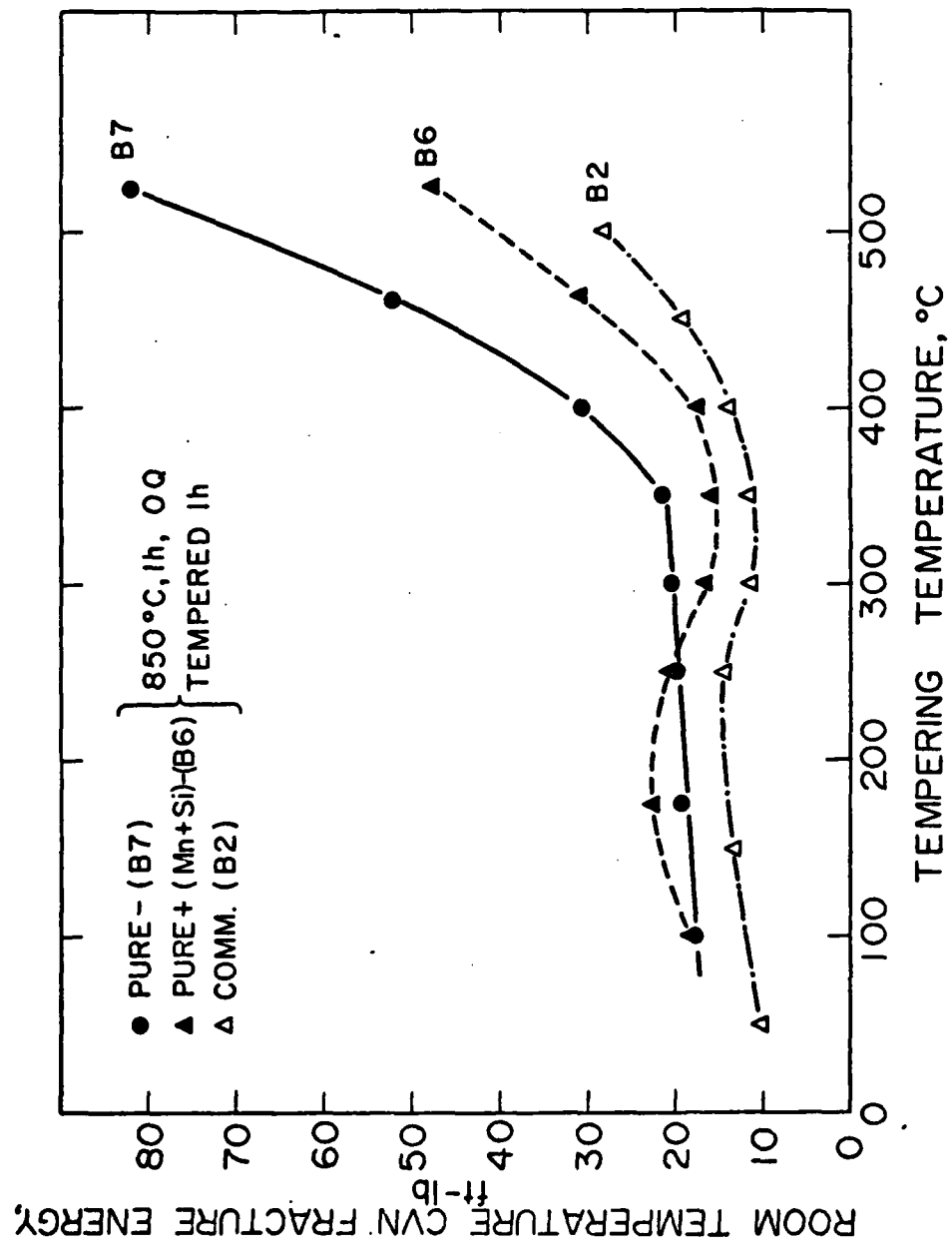
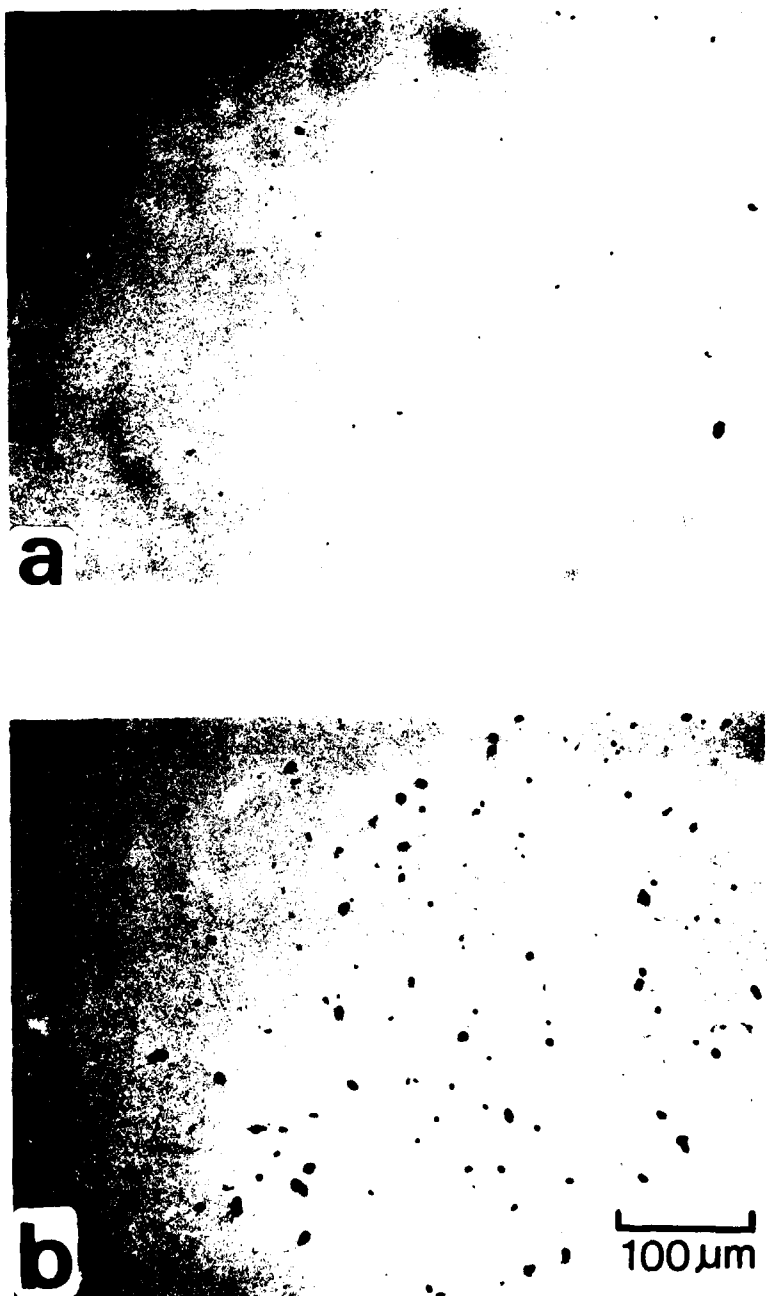


Fig. 17 Variation of Charpy V-notch fracture energy with tempering temperature at 23°C for "pure" steel B7, "pure" + Mn + Si steel B6, and "commercial" steel B2.

Fig. 18

Optical micrographs showing examples
of areas containing largest inclusion
concentration, for:
a) 'Pure + Mn + Si steel B6.
b) Commercial air-melted steel B2.



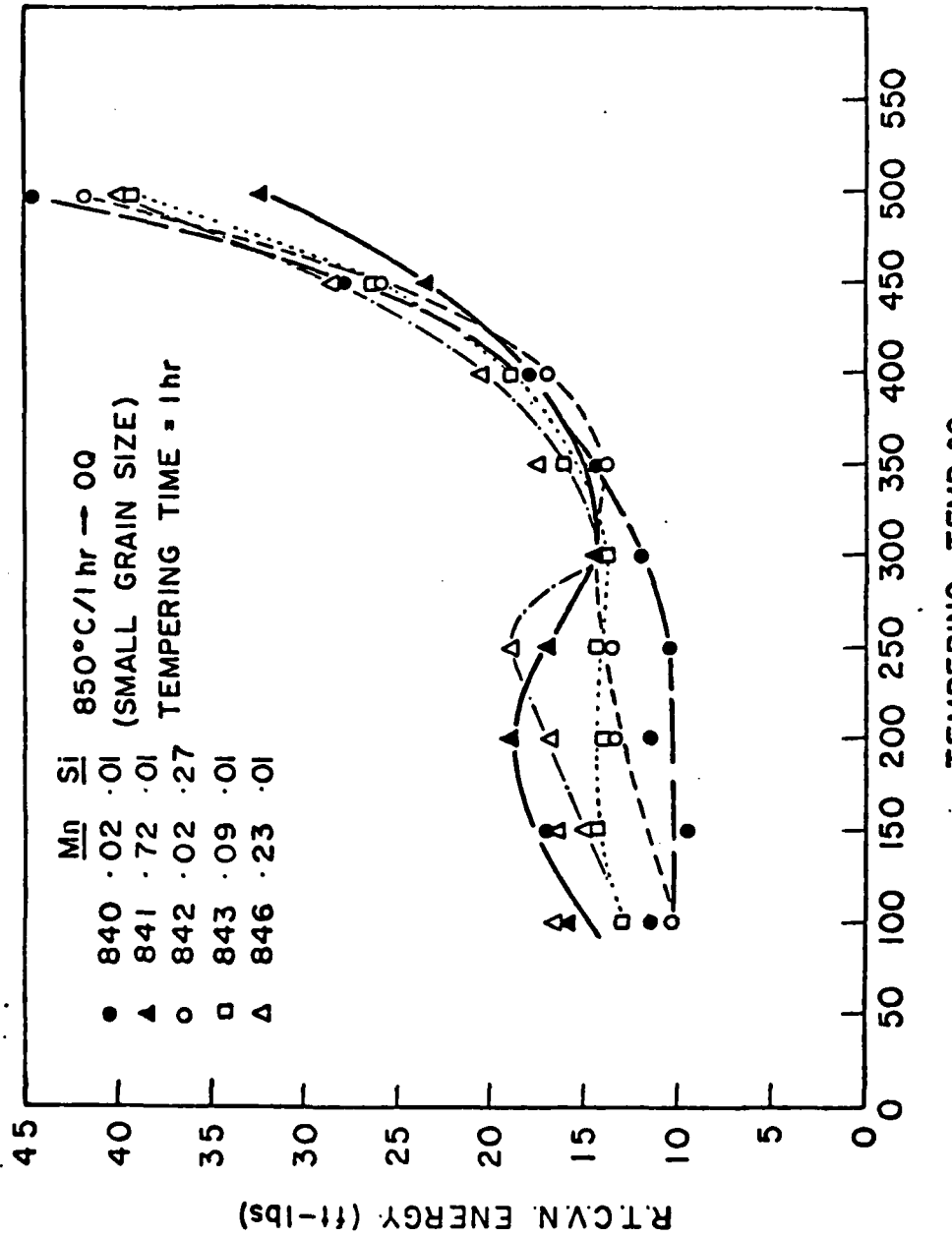


FIG. 19 Variation of Charpy V-notch fracture energy with tempering temperature at 23°C for five heats of 4340 steel with varying amounts of Mn and Si.

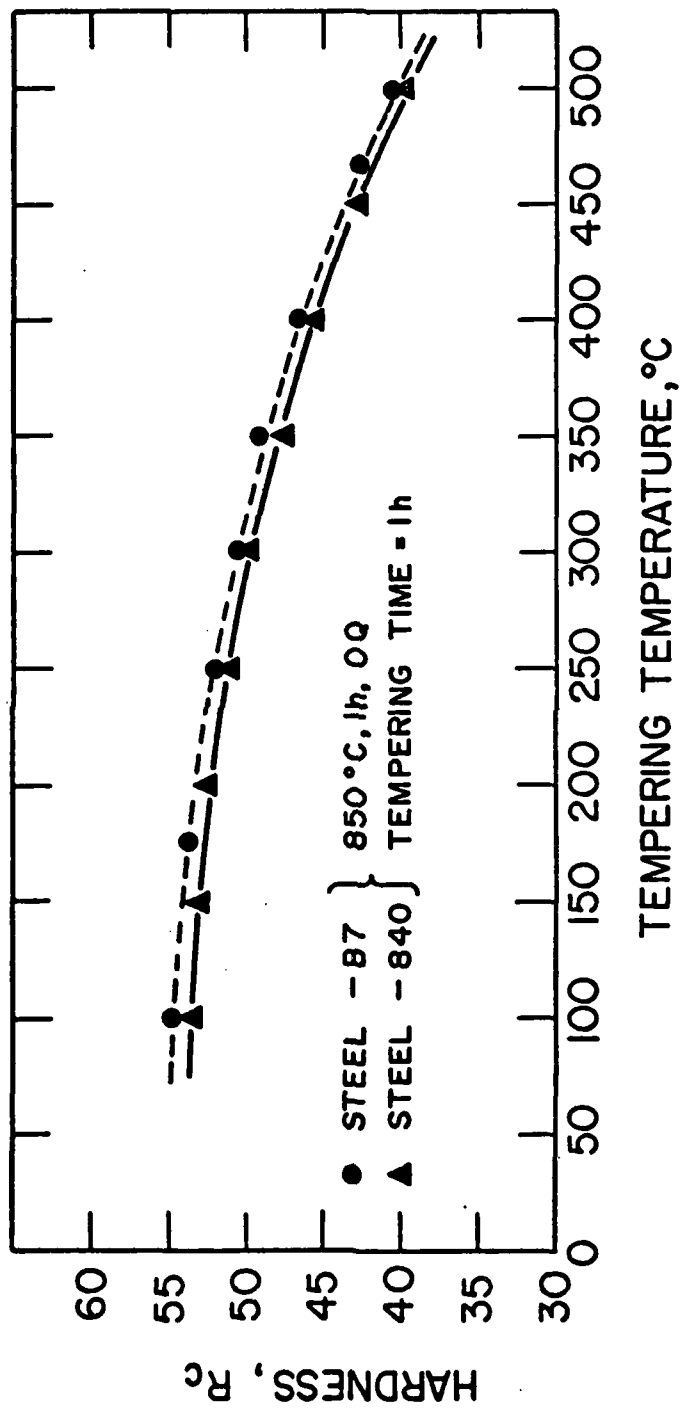


Fig. 20 Variation of hardness with tempering temperature for two Mn- and Si-free steels B7 and 840.

Fig. 20

Fig. 21

Scanning electron micrographs of
fracture surfaces of Charpy specimens
austenitized at 850°C and tempered at
250°C for steels

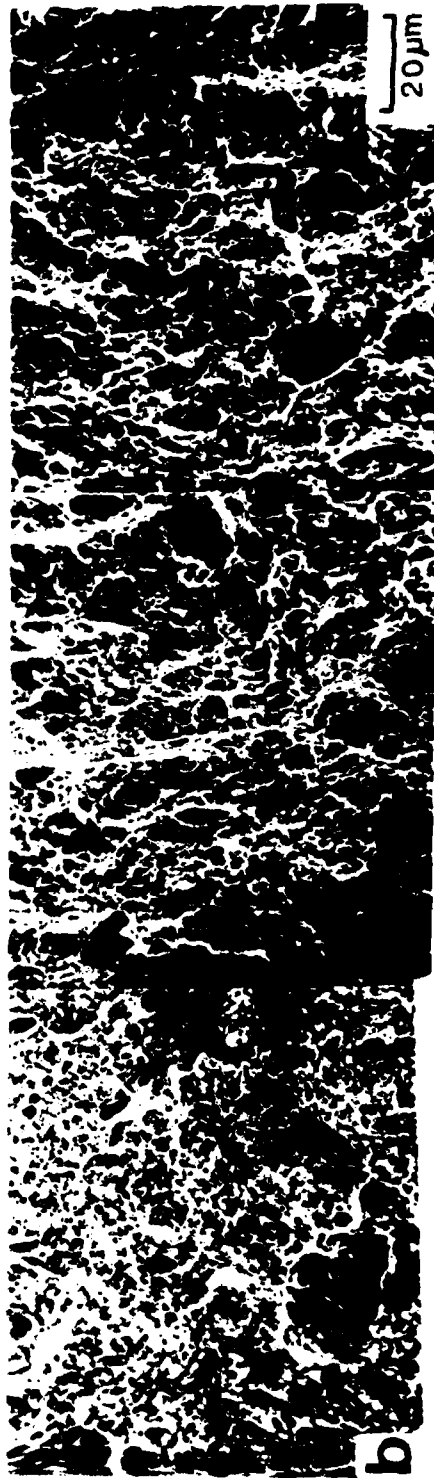
a) 840

b) B7.

Room temperature tests.



a



b

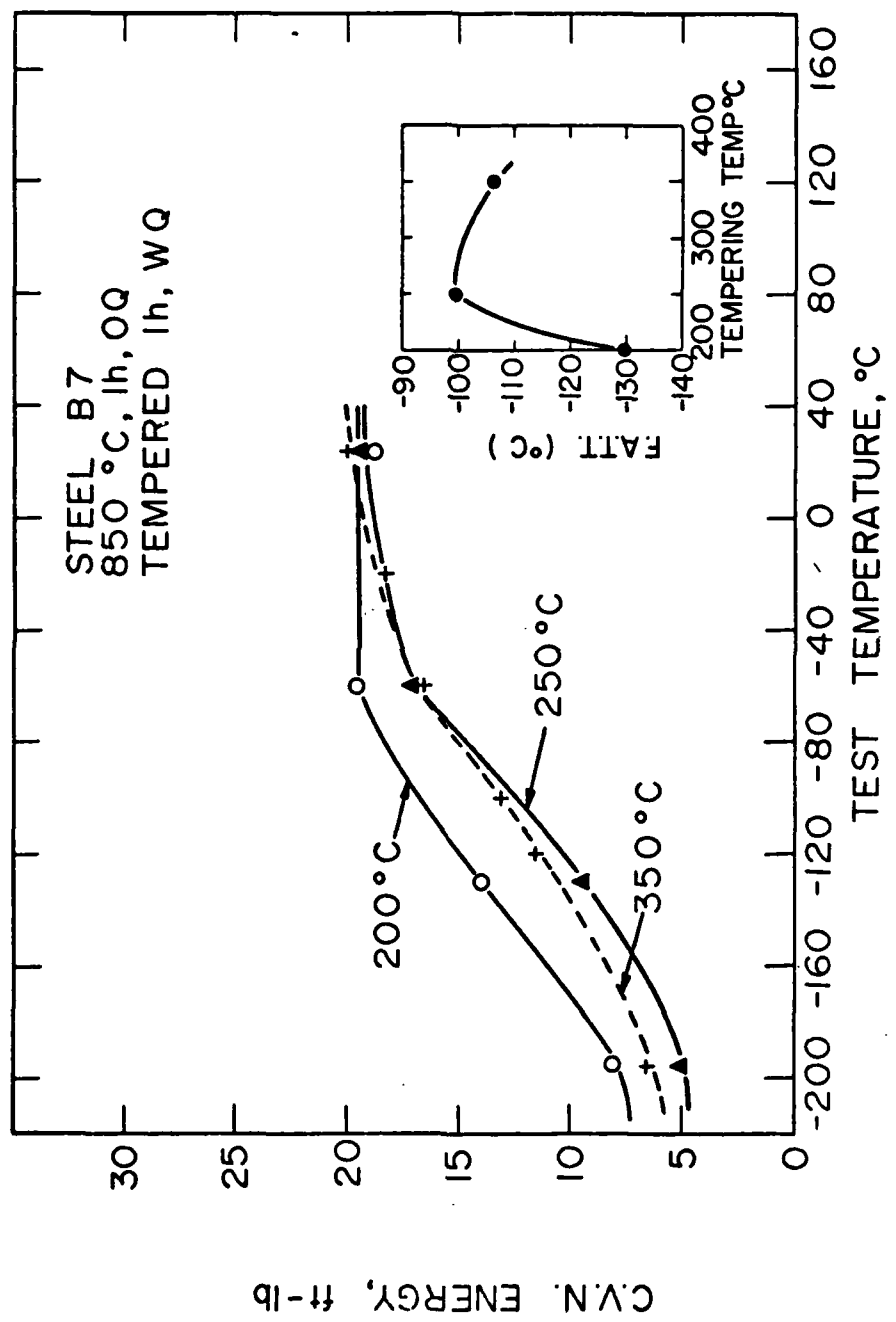


Fig. 22 Variation of Charpy V-notch fracture energy over a wide range of test temperatures for steel B7 for 200°C, 250°C, and 350°C tempering conditions.

Fig. 22

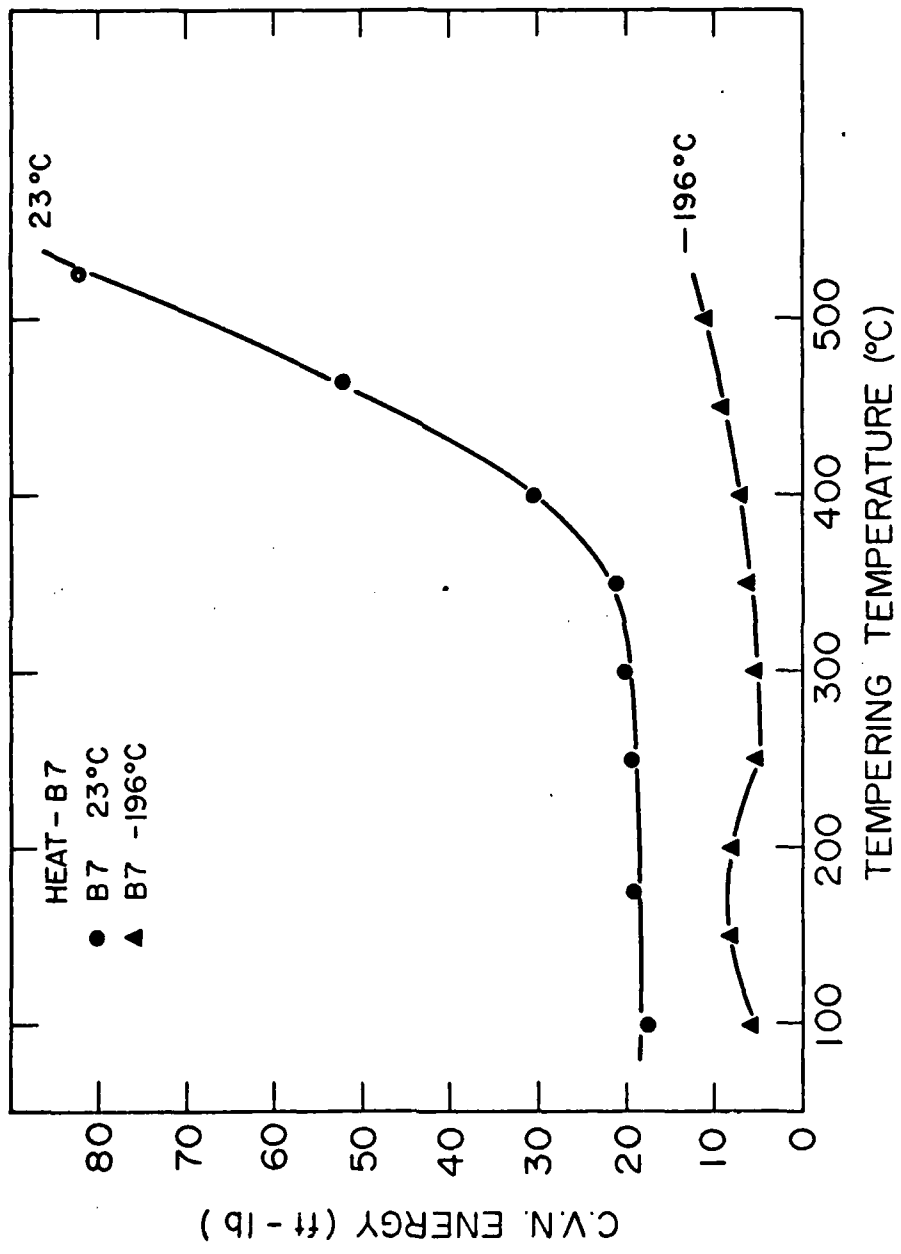


Fig. 23 Variation of Charpy V-notch fracture energy with tempering temperature at 23°C and -196°C for pure steel B7.

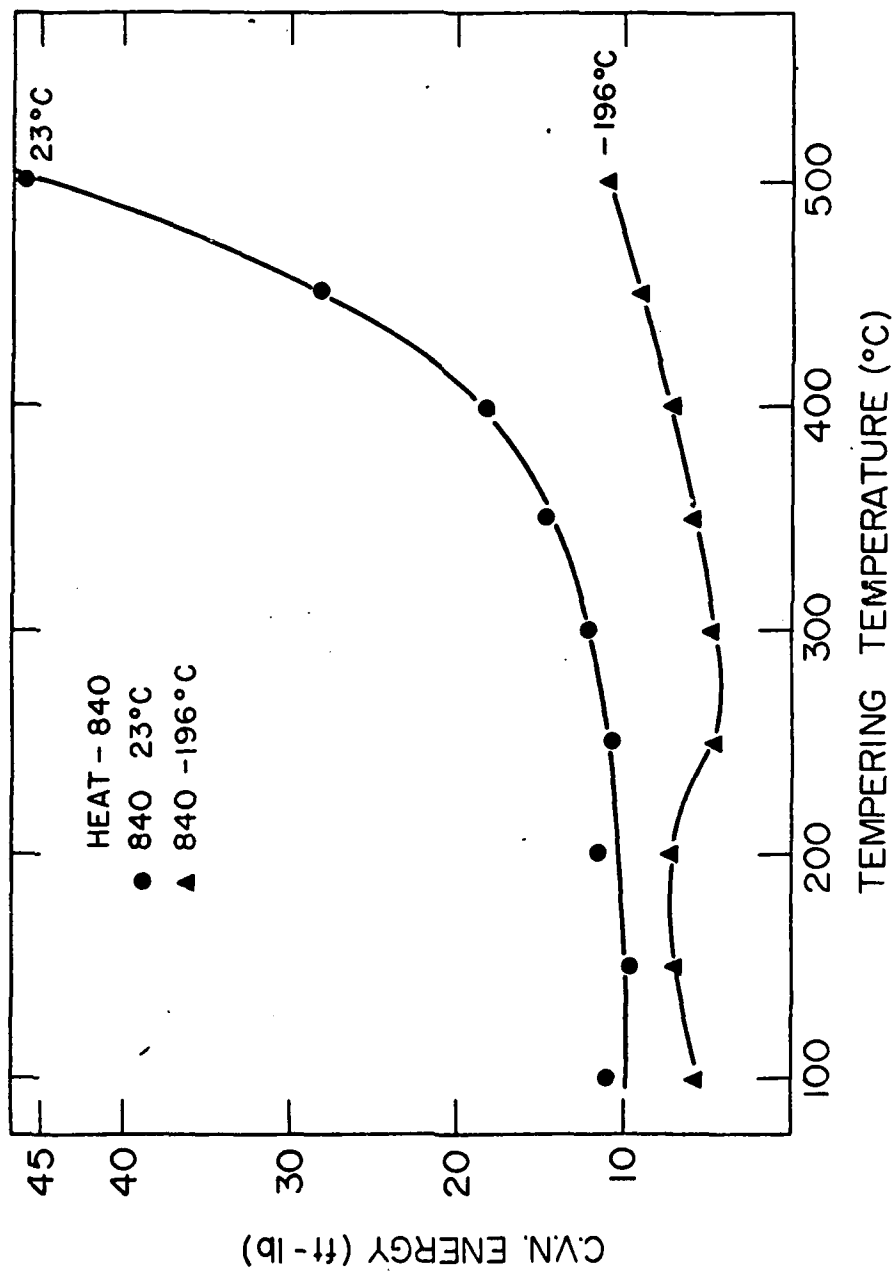
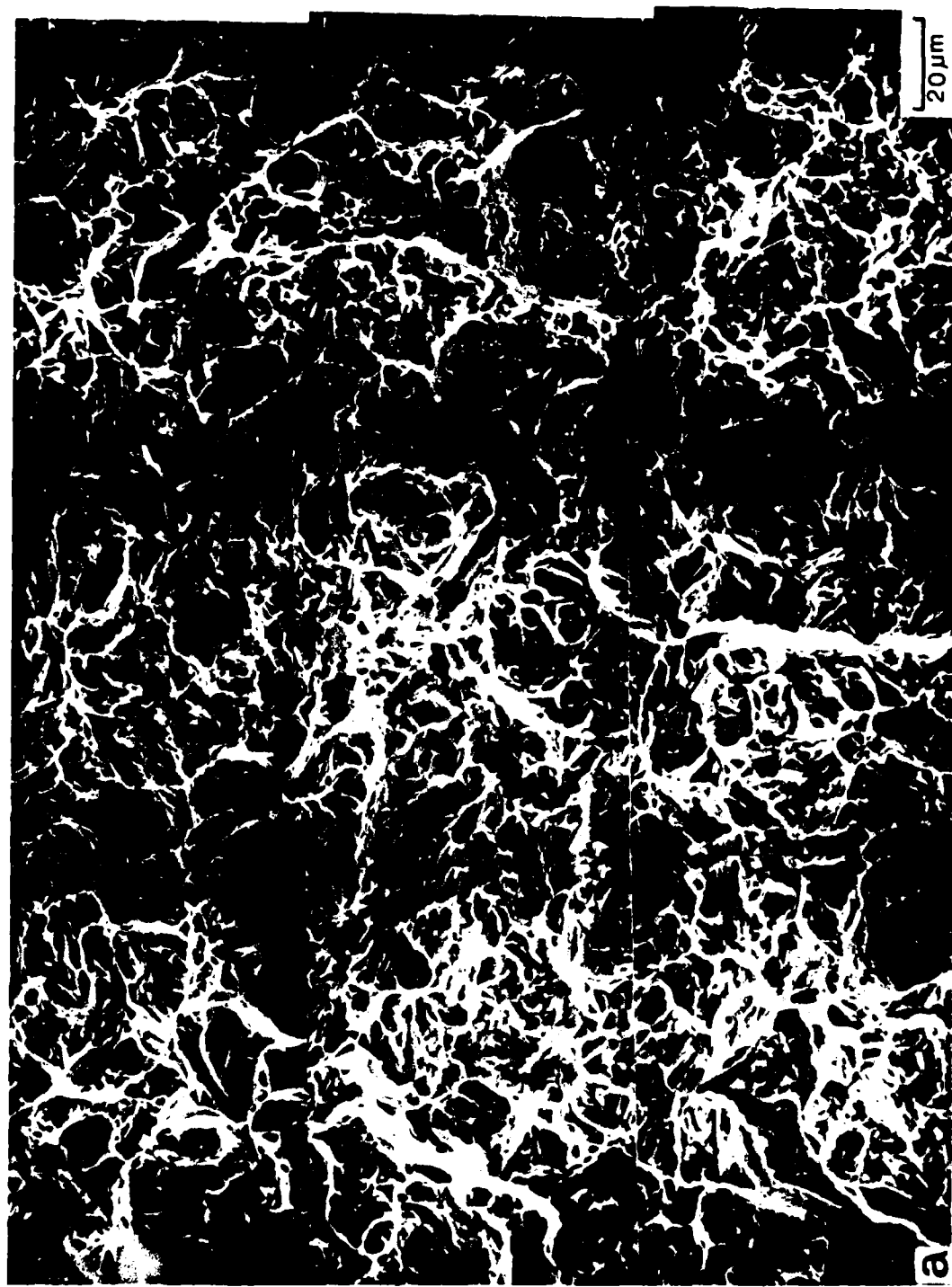
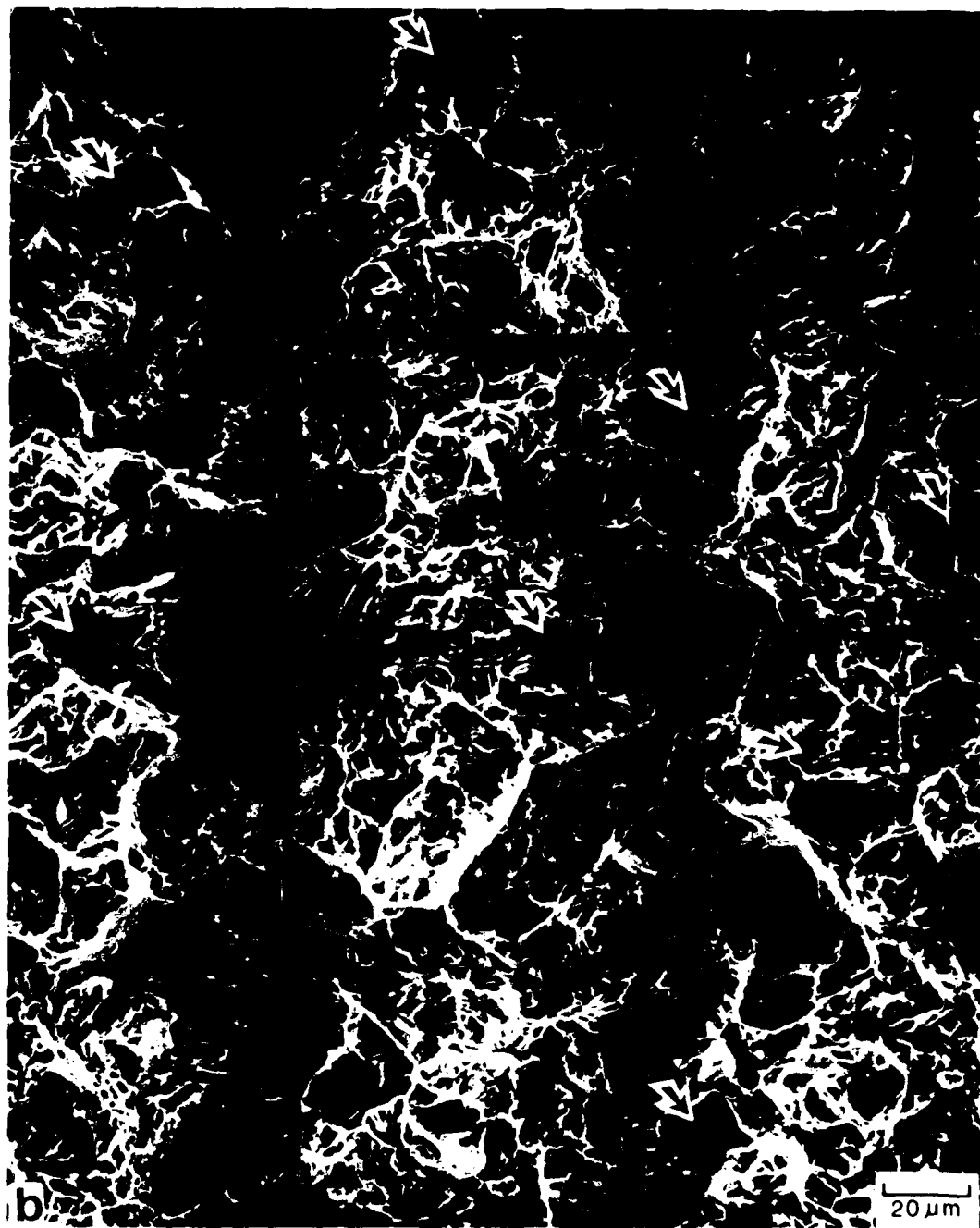


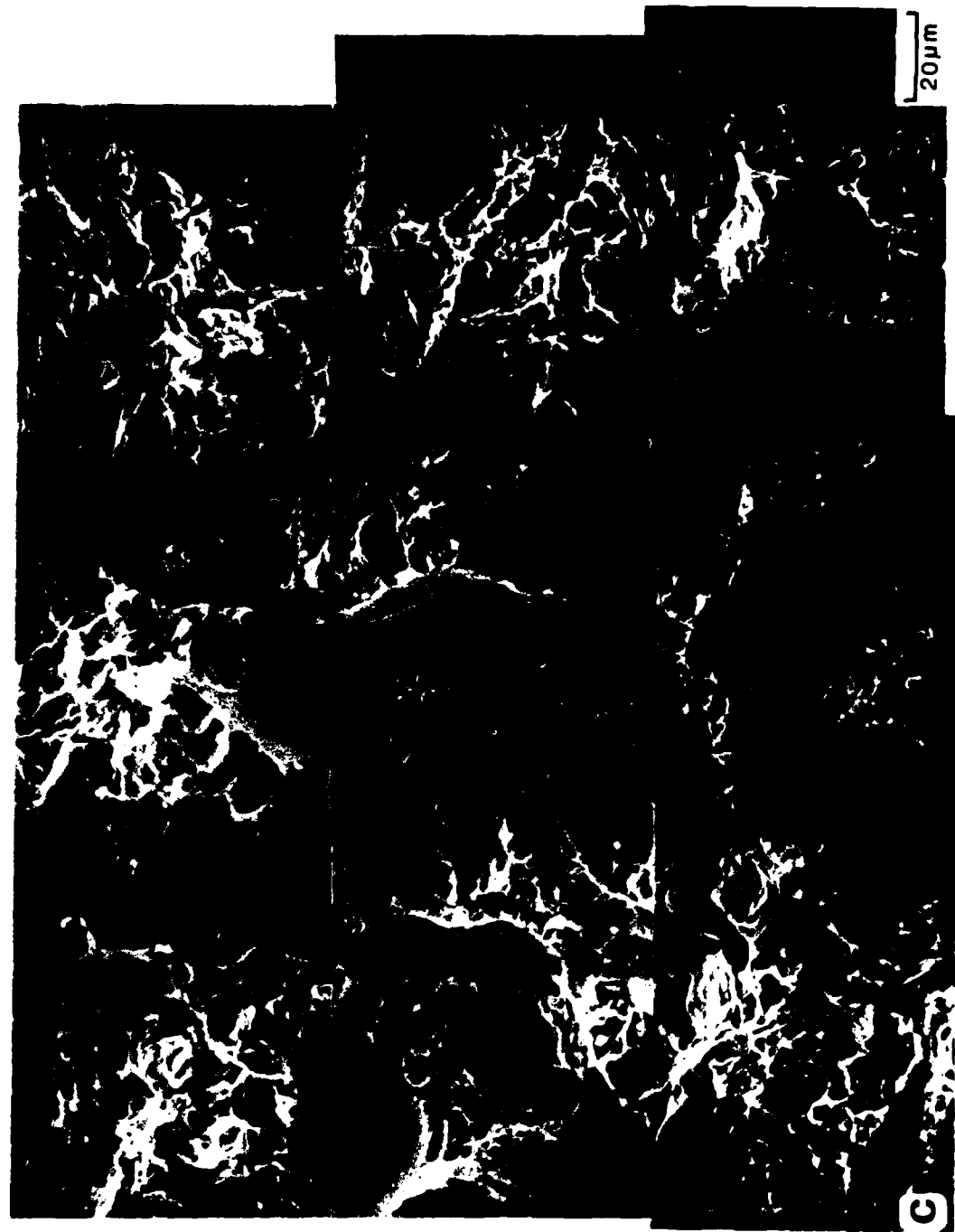
Fig. 24 Variation of Charpy V-notch fracture energy with tempering temperature at 23°C and -196°C for Mn-Si-free steel 840.

Fig. 25 Scanning electron micrographs of fracture surfaces of Charpy specimens of steel B7 austenitized at 850°C and tempered at
a) 200°C
b) 250°C, and
c) 300°C
Low temperature (-196°C) tests.





b



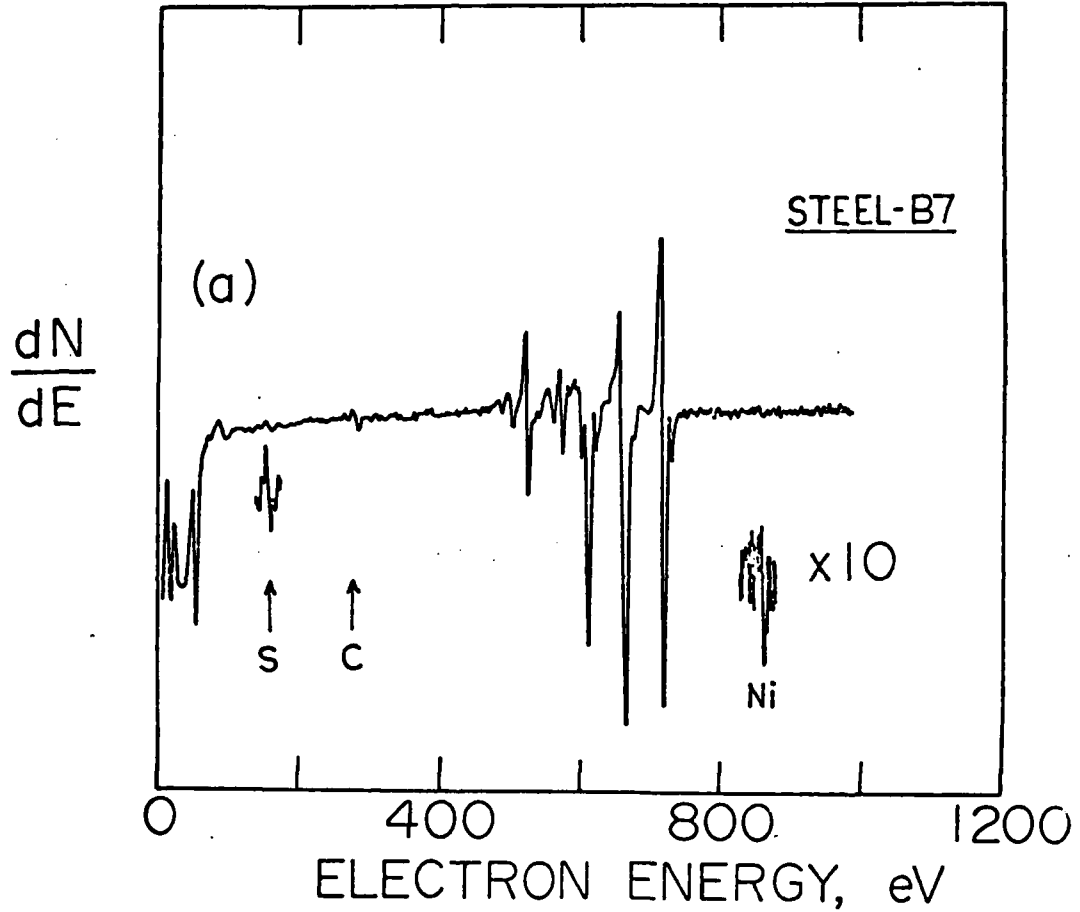


Fig. 26 Auger spectrum from intergranular fracture surface of steel B7 fractured in pure H₂ in a UHV system using a grazing incidence primary beam.

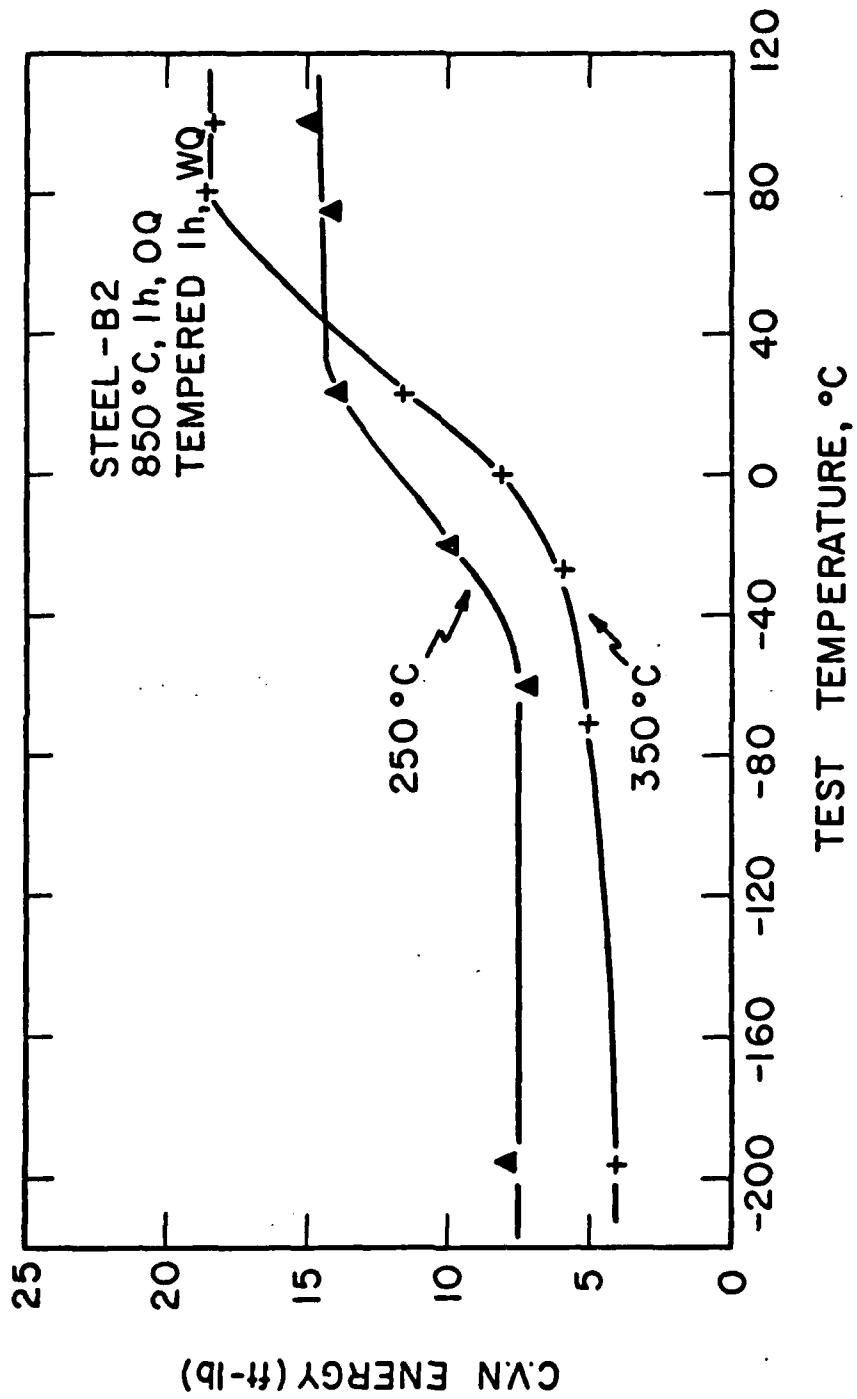


Fig. 27 Variation of Charpy V-notch fracture energy over a wide range of test temperatures for steel B2 for 250°, and 350°C tempering conditions.

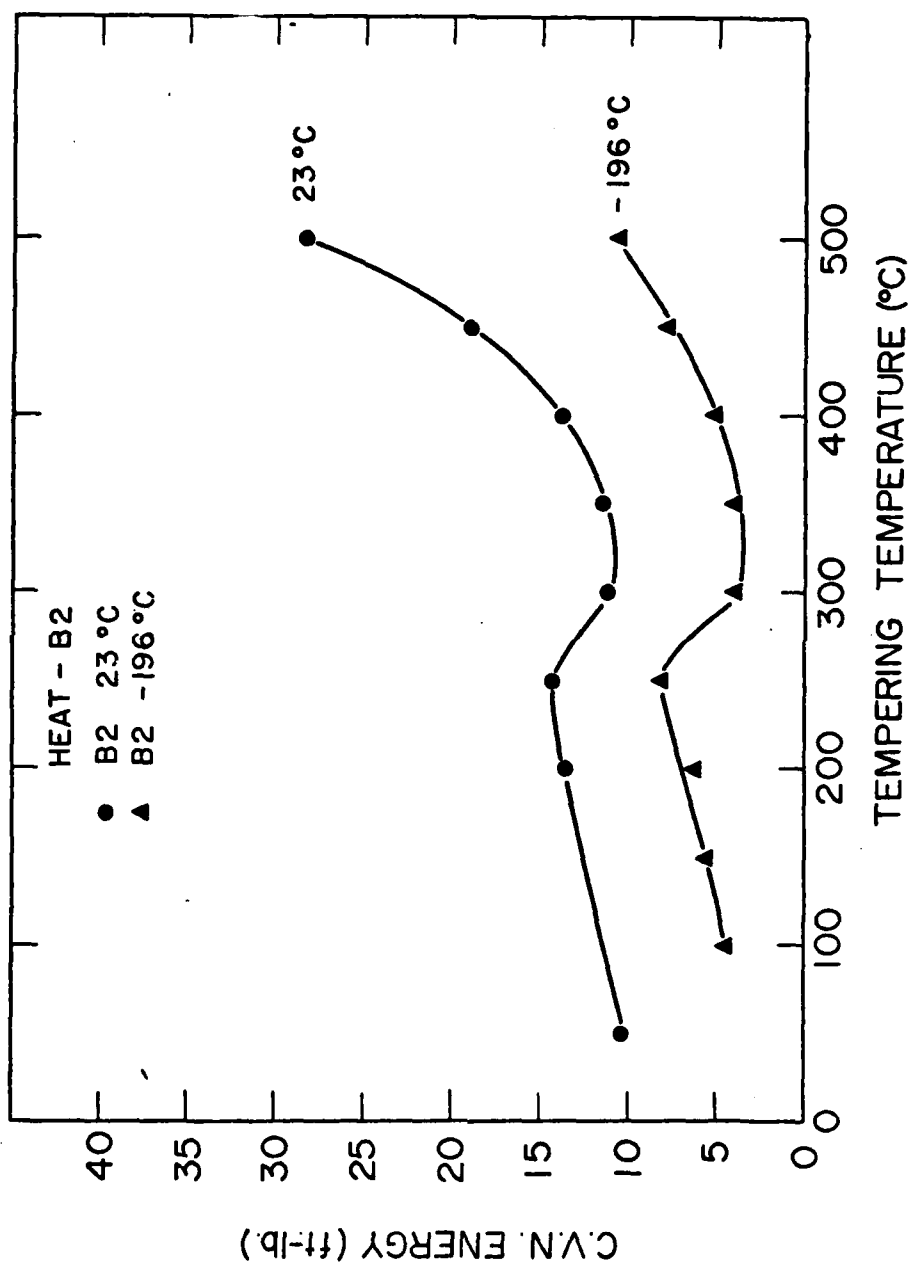
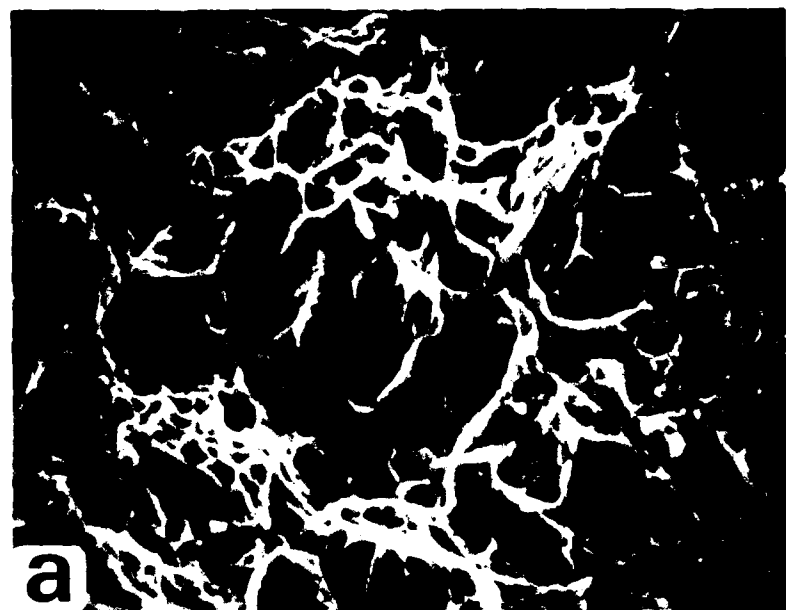


FIG. 28 Variation of Charpy V-notch fracture energy with tempering temperature at 23°C and -196°C for steel B2.

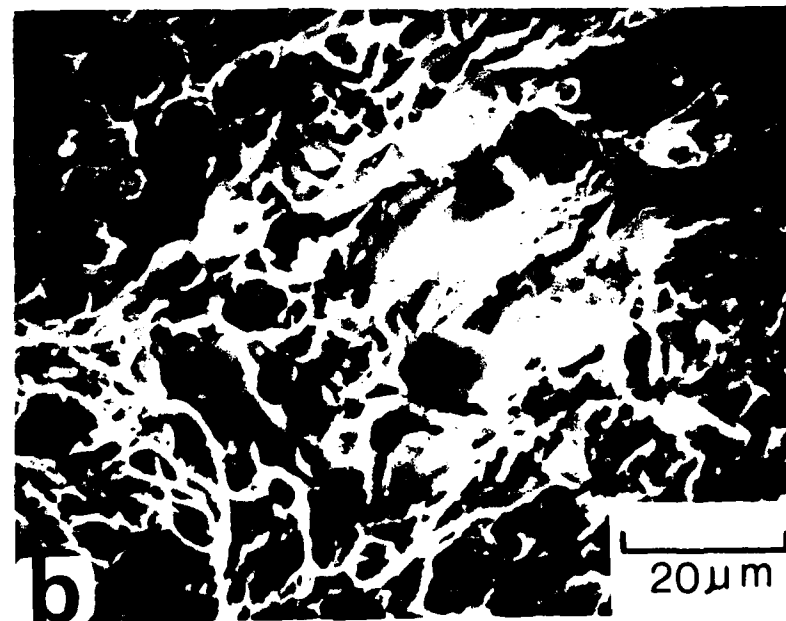
FIG. 28

Fig. 29

Scanning electron micrographs of fracture surfaces of Charpy specimens of steel B2 austenitized at 850°C and tempered at 350°C at two test temperatures:
a) 23°C
b) -196°C



a



b

20 μm

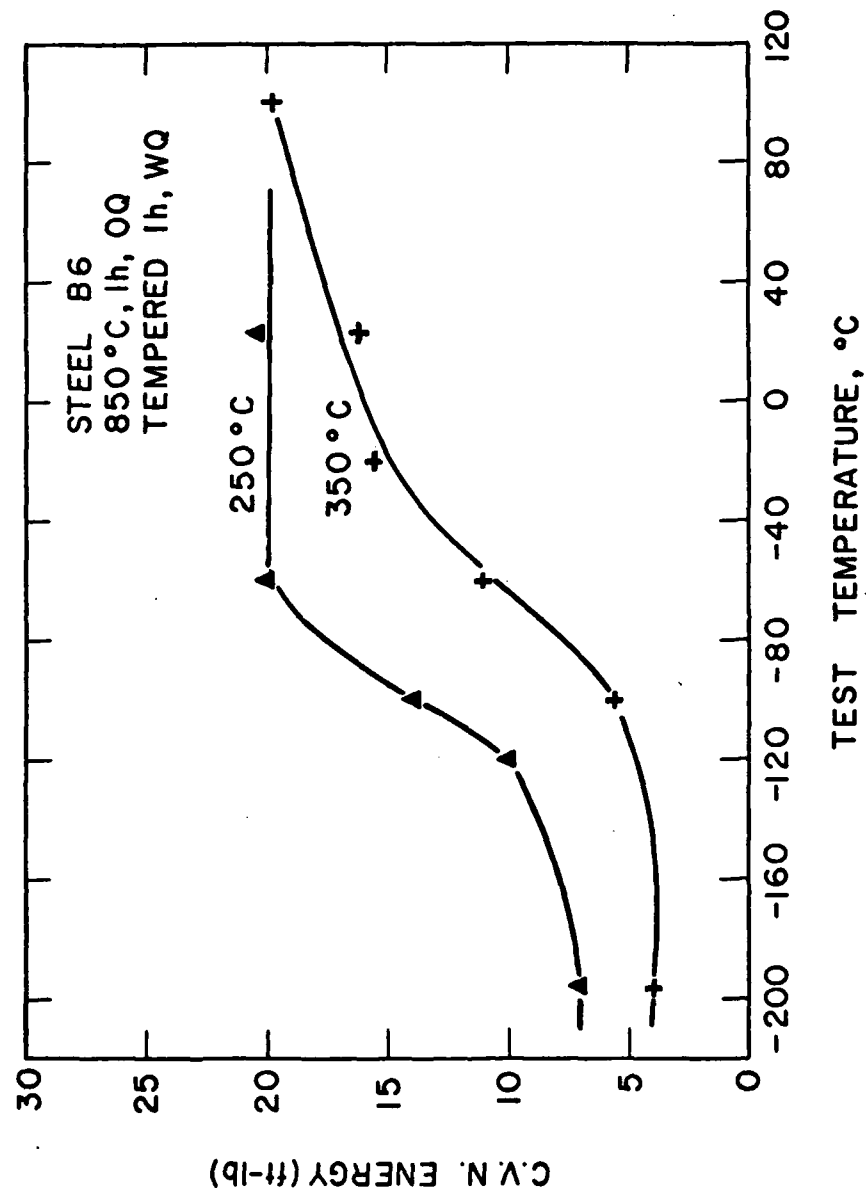
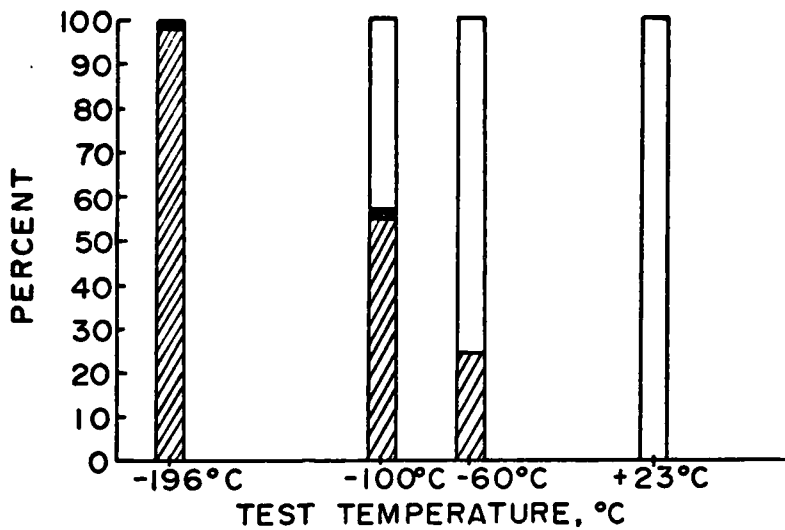


Fig. 30 Variation of Charpy V-notch fracture energy over a wide range of test temperatures for steel B6 for 250°C , and 350°C tempering conditions.

Fig. 30

□ RUPTURE
■ CLEAVAGE
■ I.G.

STEEL-B6 850°C, lh, OQ, TEMPERED 250°C, lh, WQ



STEEL-B6 850°C, lh, OQ, TEMPERED 350°C, lh, WQ

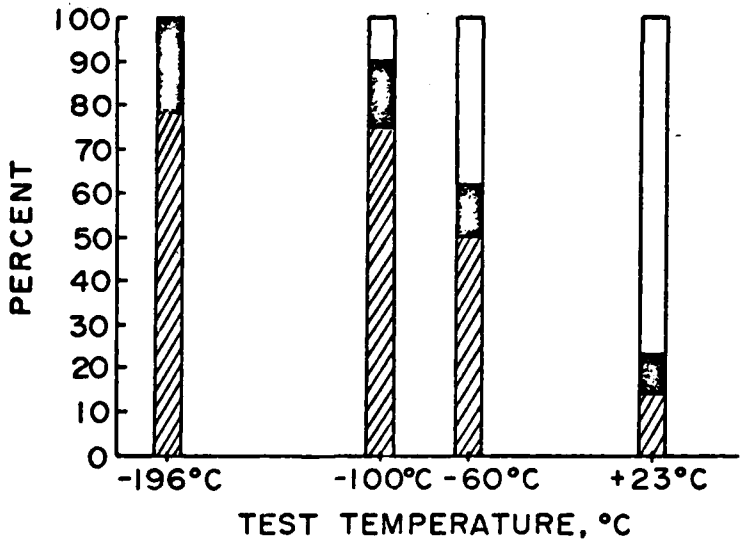


Fig. 31

Changes in fracture mode for steel B6 in unembrittled (250°C temper) and embrittled (350°C temper) and conditions.

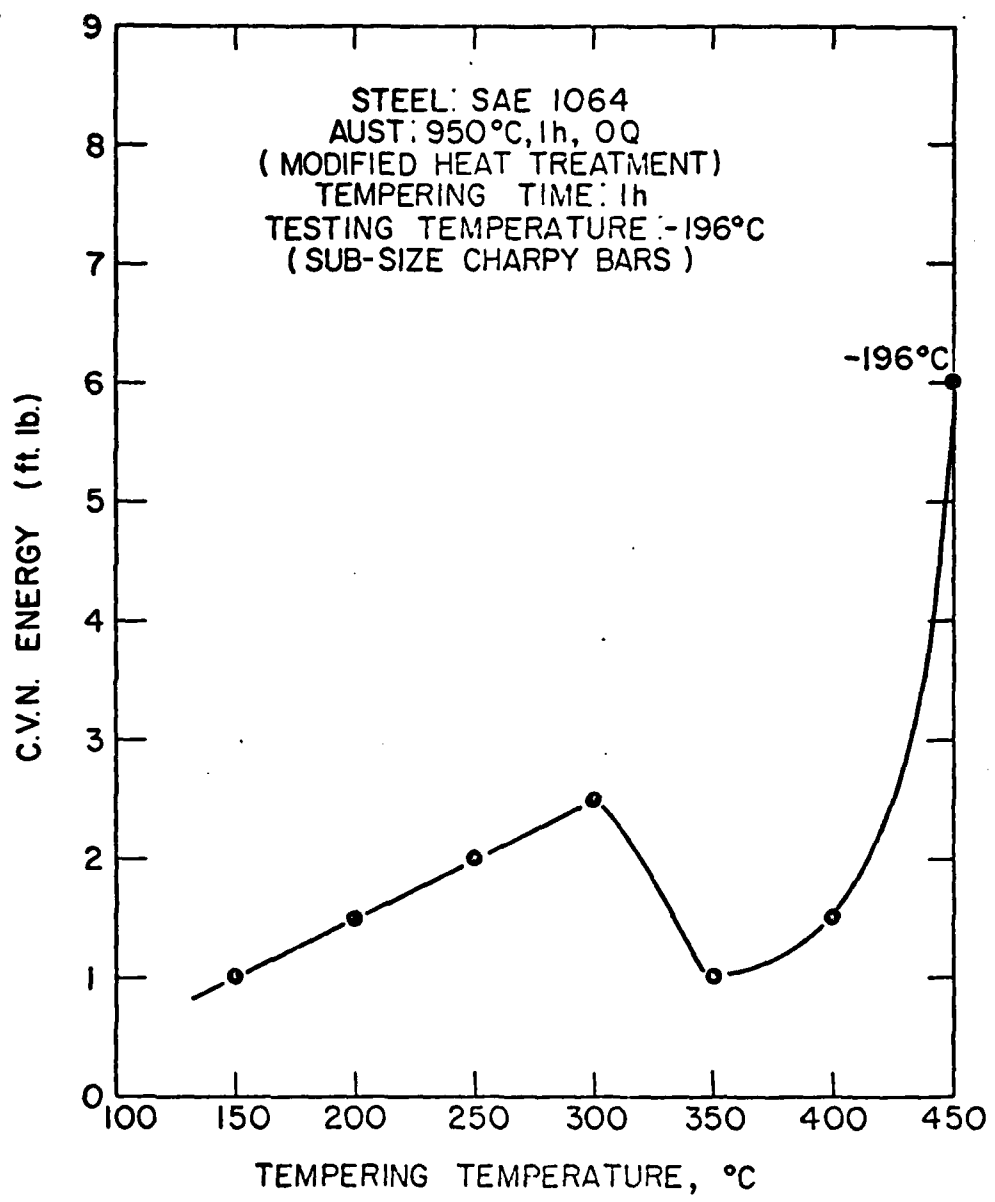


Fig. 32

Variation of Charpy V-notch fracture energy with tempering temperature at -196°C for plain carbon steel SAE 1064.

Fig. 33

Scanning electron micrograph of fracture surface of Charpy specimen of steel SAE 1064 austenitized at 950°C and tempered at 350°C . Intergranular facets are indicated by arrows. Low temperature (-196°C) tests.

AD-A116 948

PENNSYLVANIA UNIV. PHILADELPHIA DEPT OF MATERIALS SCI--ETC F/8 11/6
EFFECTS OF RESIDUAL IMPURITIES ON HYDROGEN ASSISTED CRACKING IN--ETC(U)
JUN 82 N BANDYOPADHYAY, C J MCNAMEE

N00019-78-C-0387

NL

UNCLASSIFIED

2-2

4-2A

4-2B



END
DATE
TIME
-82
RTIC



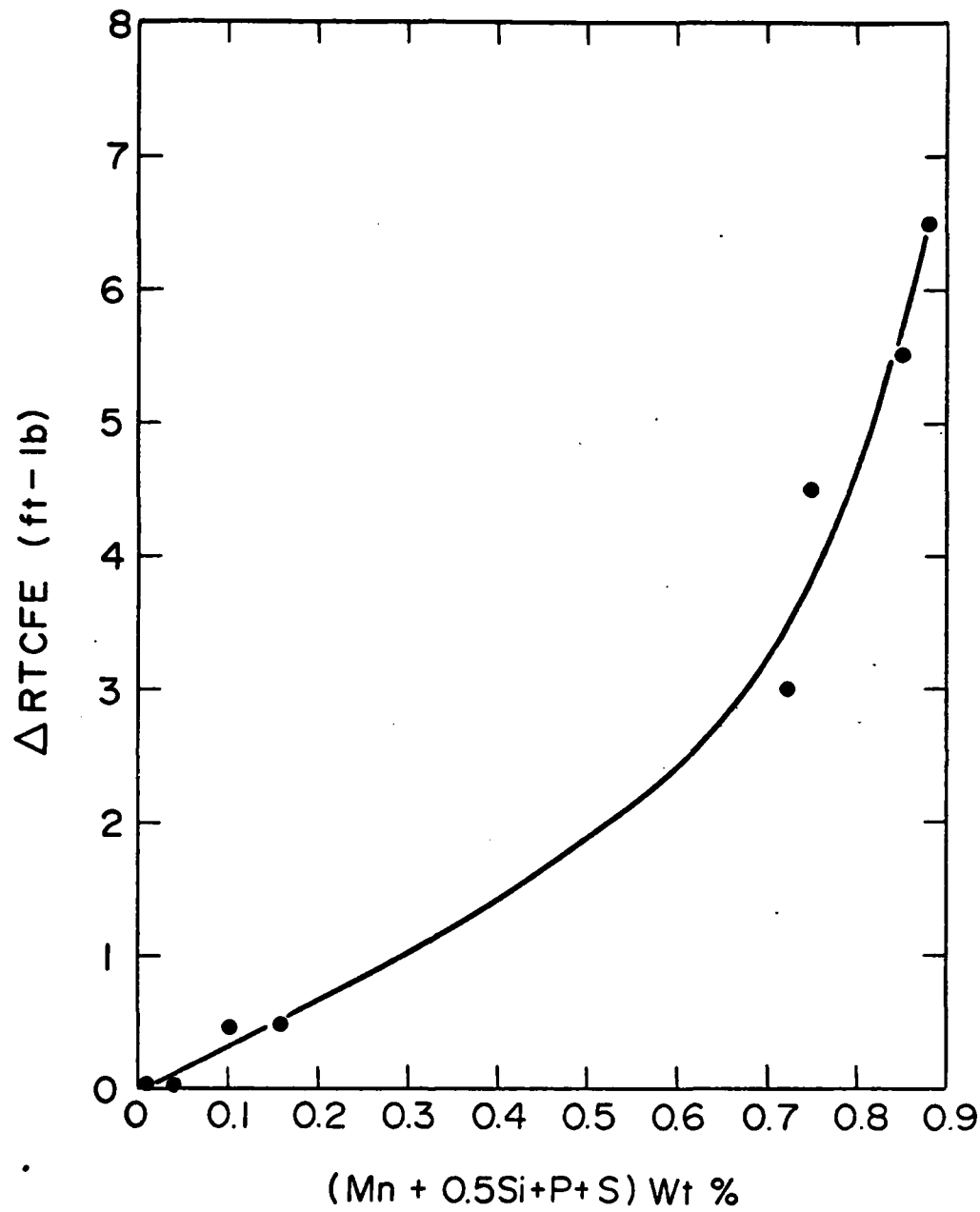


Fig. 34 Variation of the magnitude of Charpy energy trough with composition parameter $(Mn+0.5Si+P+S)$ in wt%.

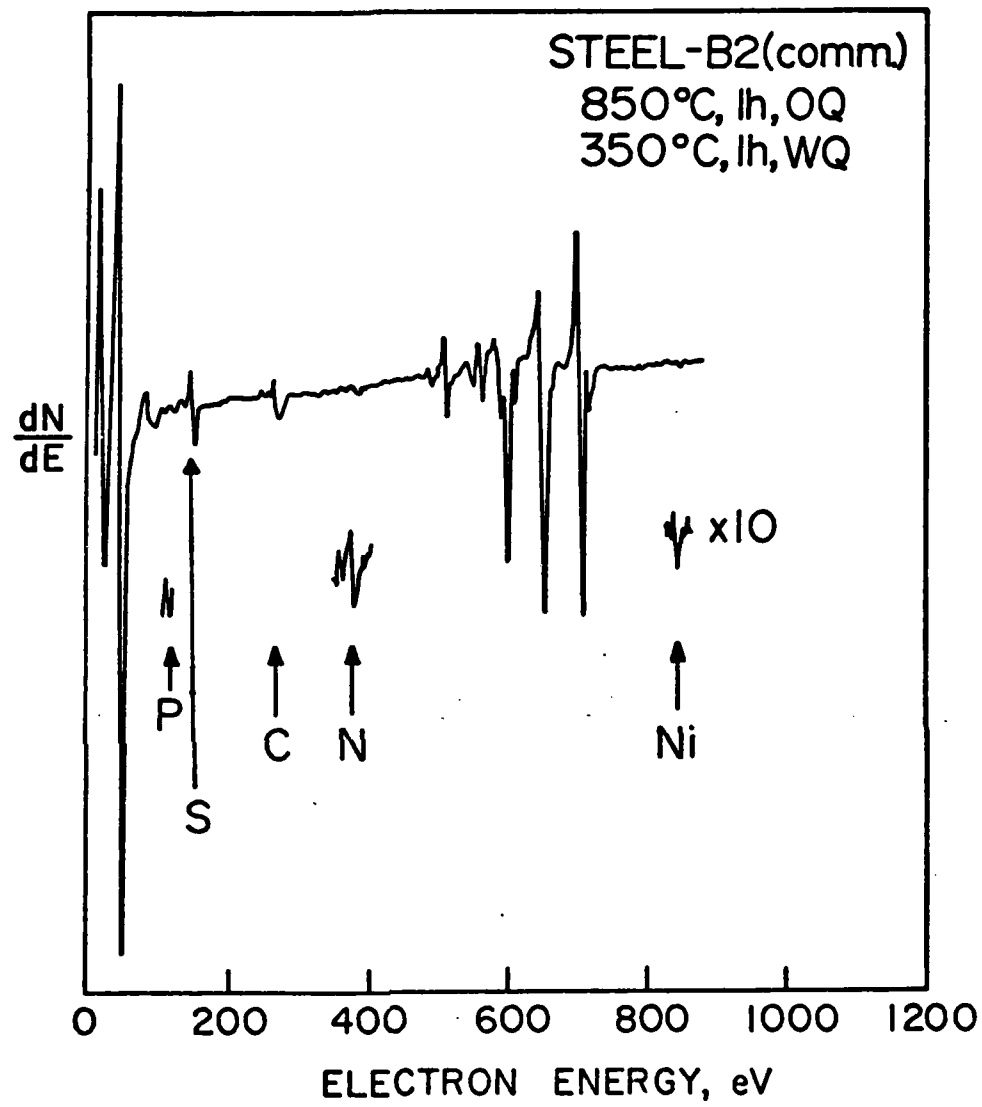


Fig. 35

Auger spectrum from intergranular fracture surface of commercial steel B2 fractured in pure H₂ in a UHV system using a grazing incidence primary beam.

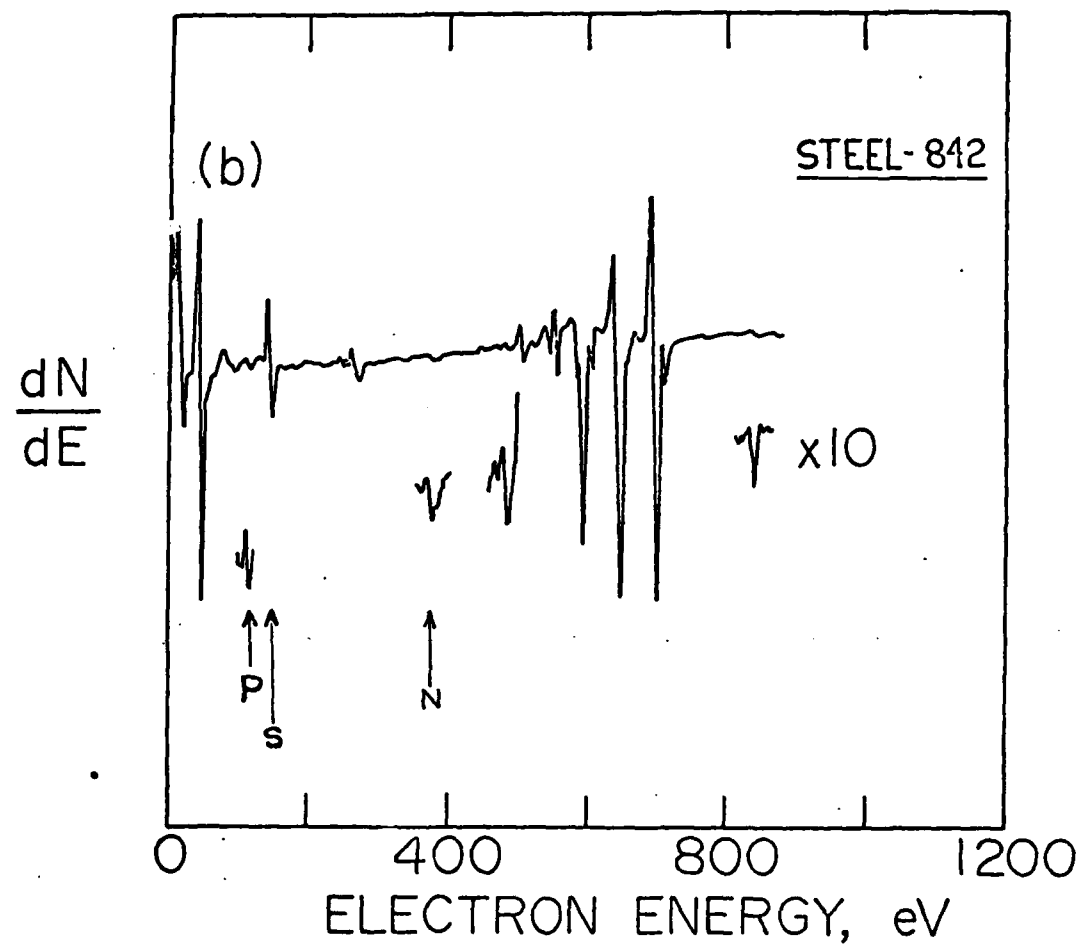


Fig. 36

Auger spectrum from intergranular fracture surface of steel 842 fractured in pure H_2 in a UHV system using a grazing incidence primary beam.

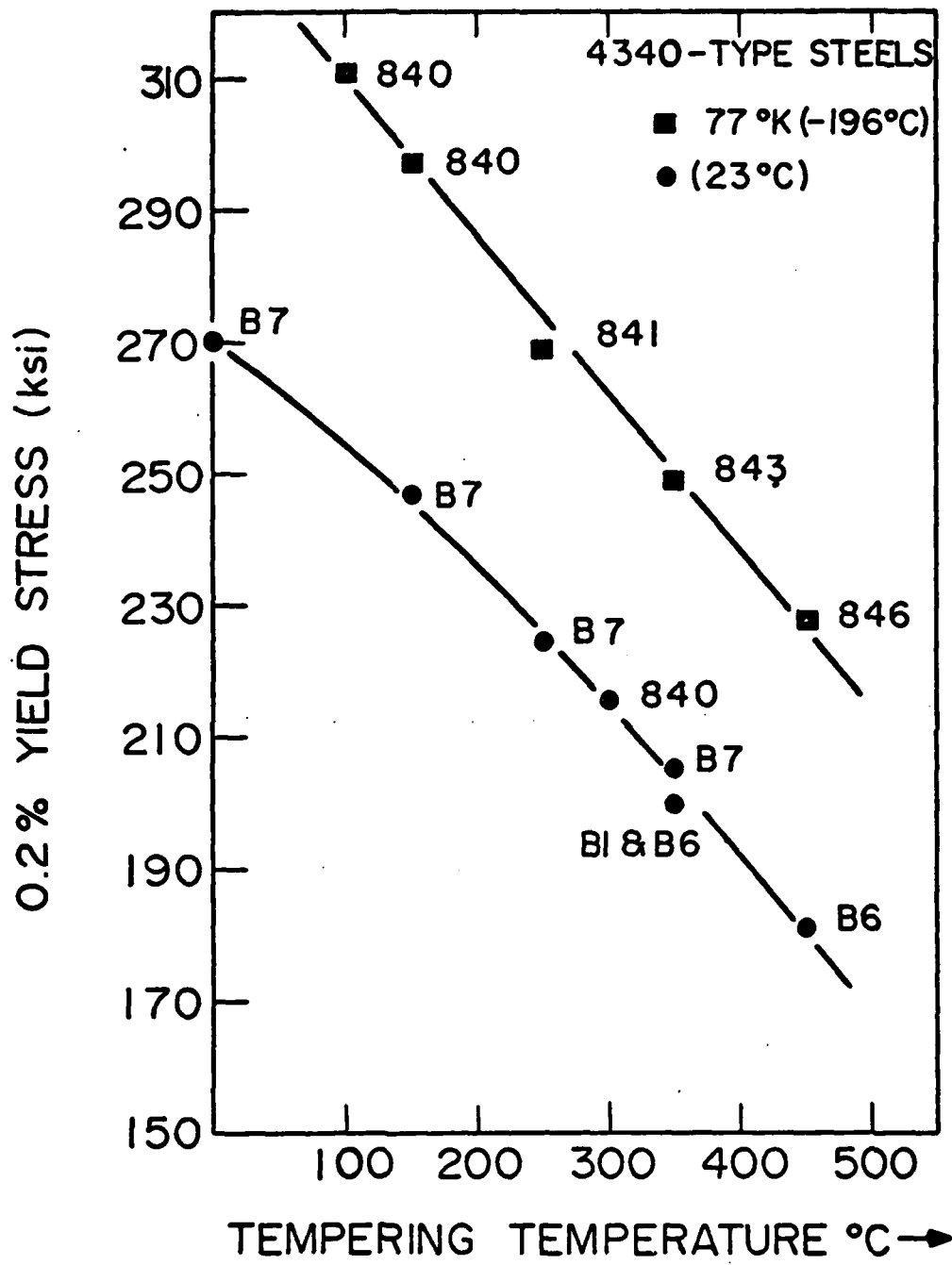


Fig. 37

Variation of yield stress with tempering temperature for two different test temperatures.

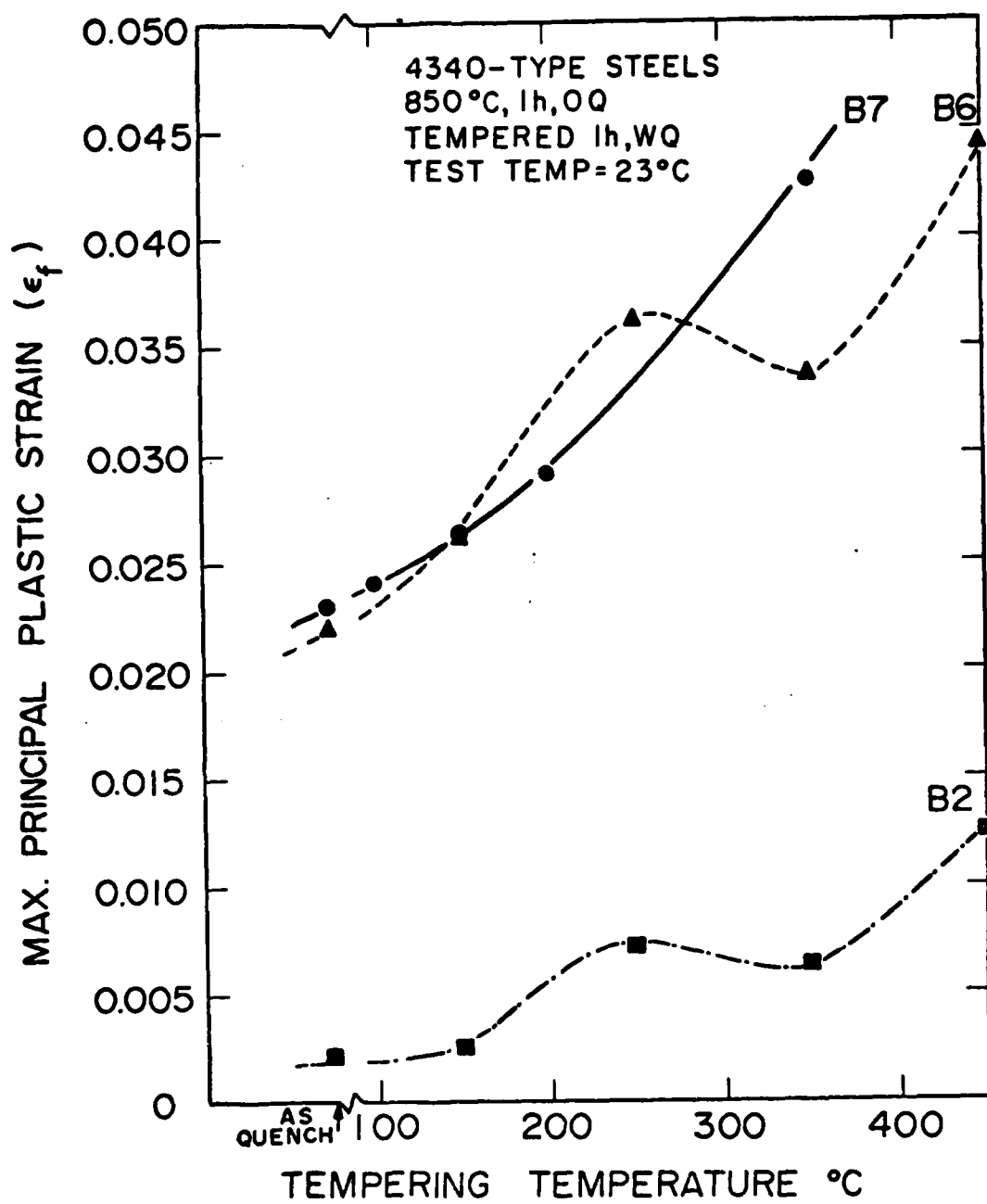
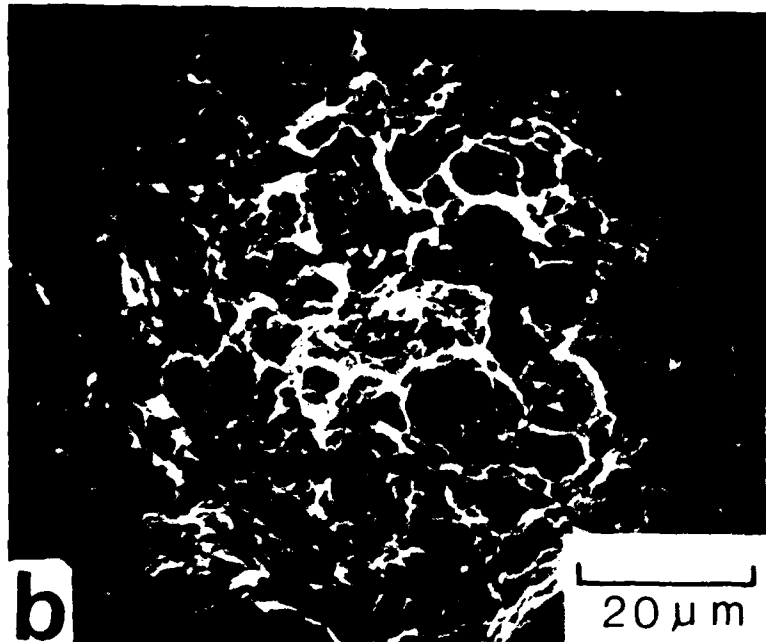


Fig. 38

Variation of calculated notch root strain at failure with tempering temperature for two vacuum-melted lab heats B7 and B6 and one commercial heat B2. Room temperature tests.

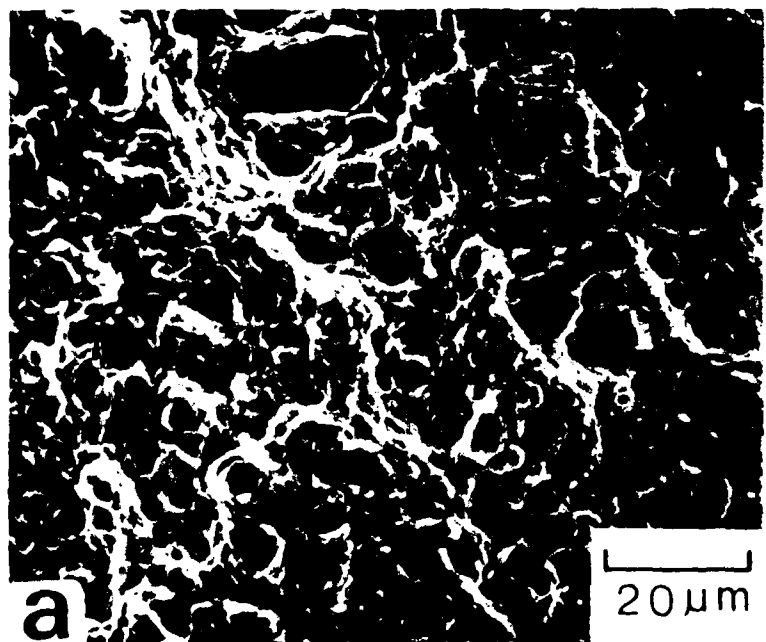
Fig. 39

Scanning electron micrographs of
fracture surfaces of four-point bend
specimens showing regions just below
the notch root for
a) Steel B2 and
b) Steel B6.



b

20 μm

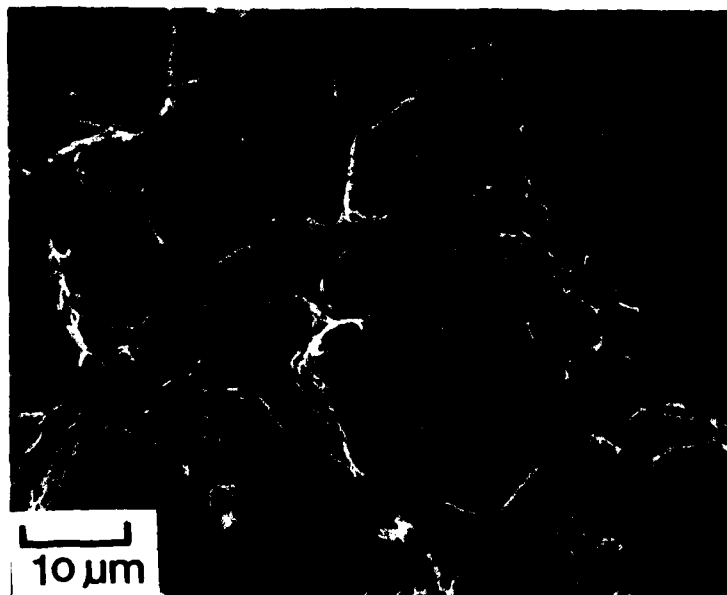


a

20 μm

Fig. 40

Scanning electron micrograph of fracture surface just ahead of initial rupture for steel B2 austenitized at 850°C and tempered at 350°C, showing intergranular fracture.



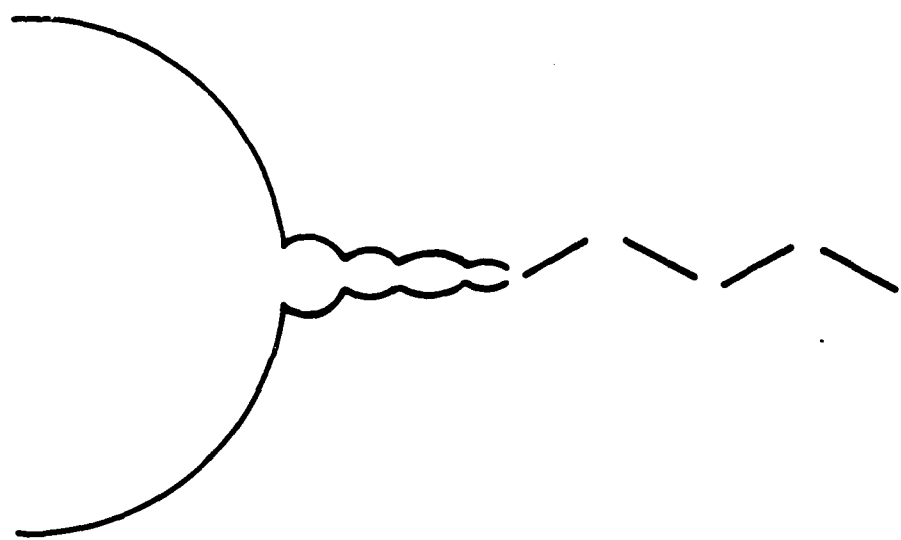


Fig. 41

Schematic illustration of switching
fracture mode from initial rupture
to partly intergranular fracture.
See text.

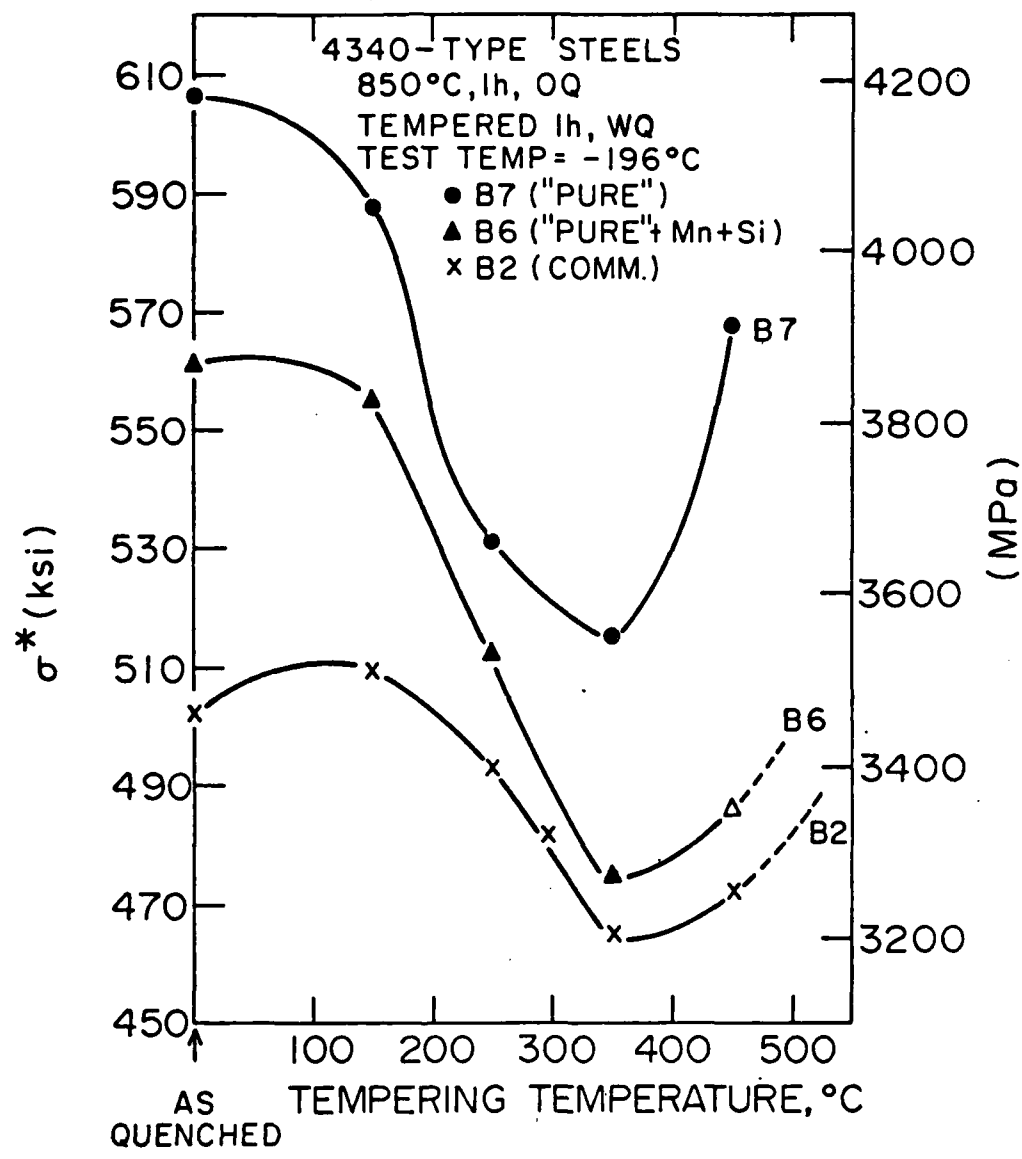
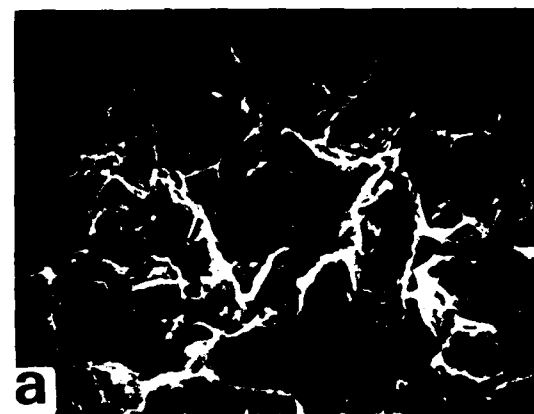


Fig. 42

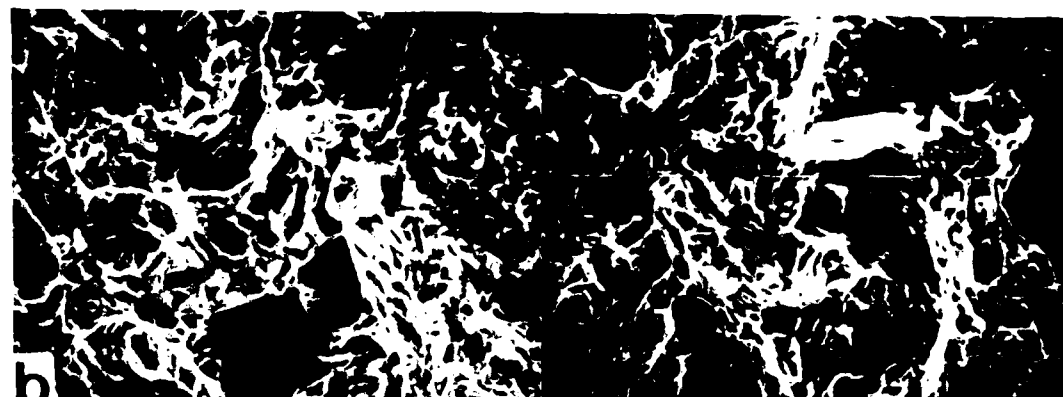
Variation of critical local stress for fracture σ^* with tempering temperature for two vacuum-melted lab heats B7 and B6 and one commercial heat B2. Low temperature (-196°C) tests.

Fig. 43

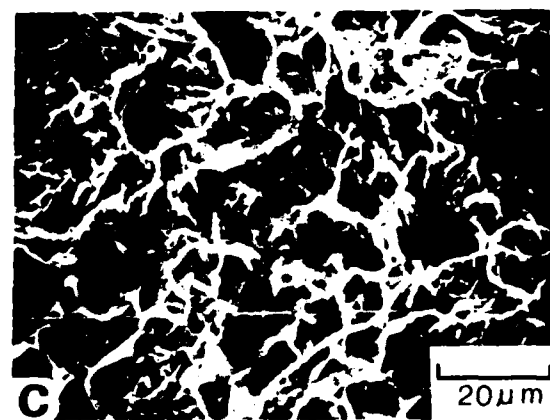
Scanning electron micrographs of
fracture surfaces of four-point bend
specimens austenitized at 850°C and
tempered at 350°C for
a) Steel B7.
b) Steel B6, and
c) Steel B2.
Low temperature (-196°C) tests.



a



b

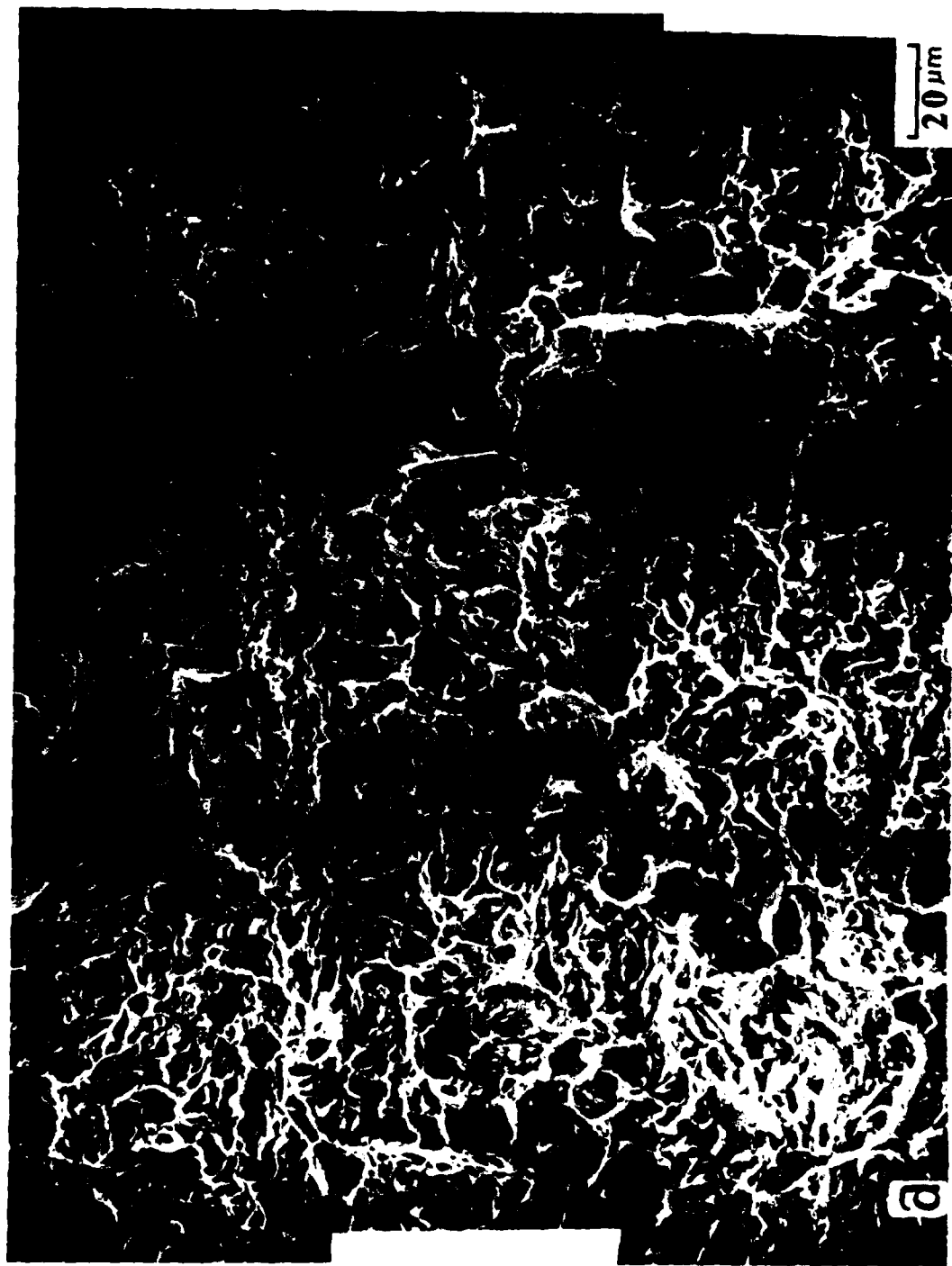


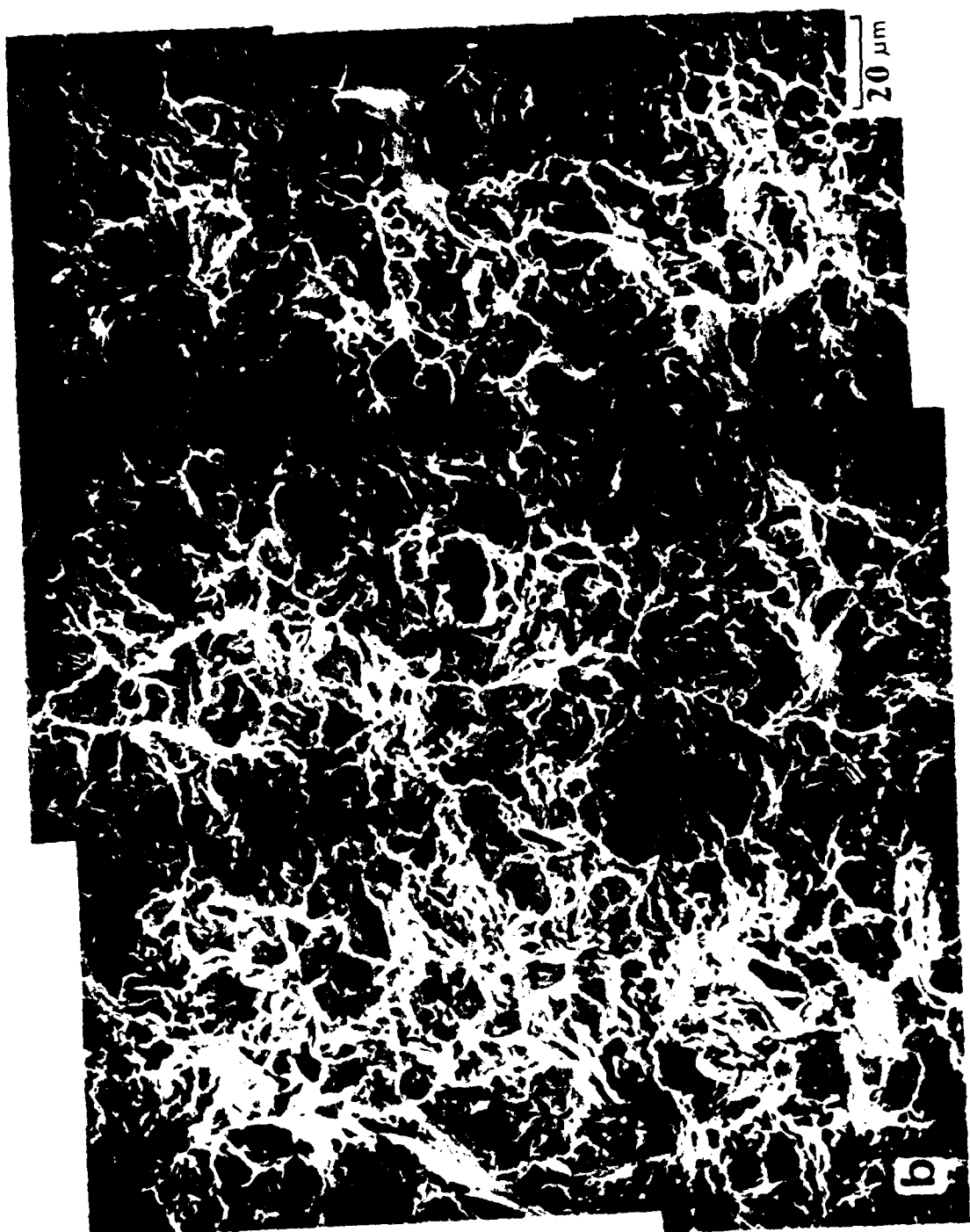
c

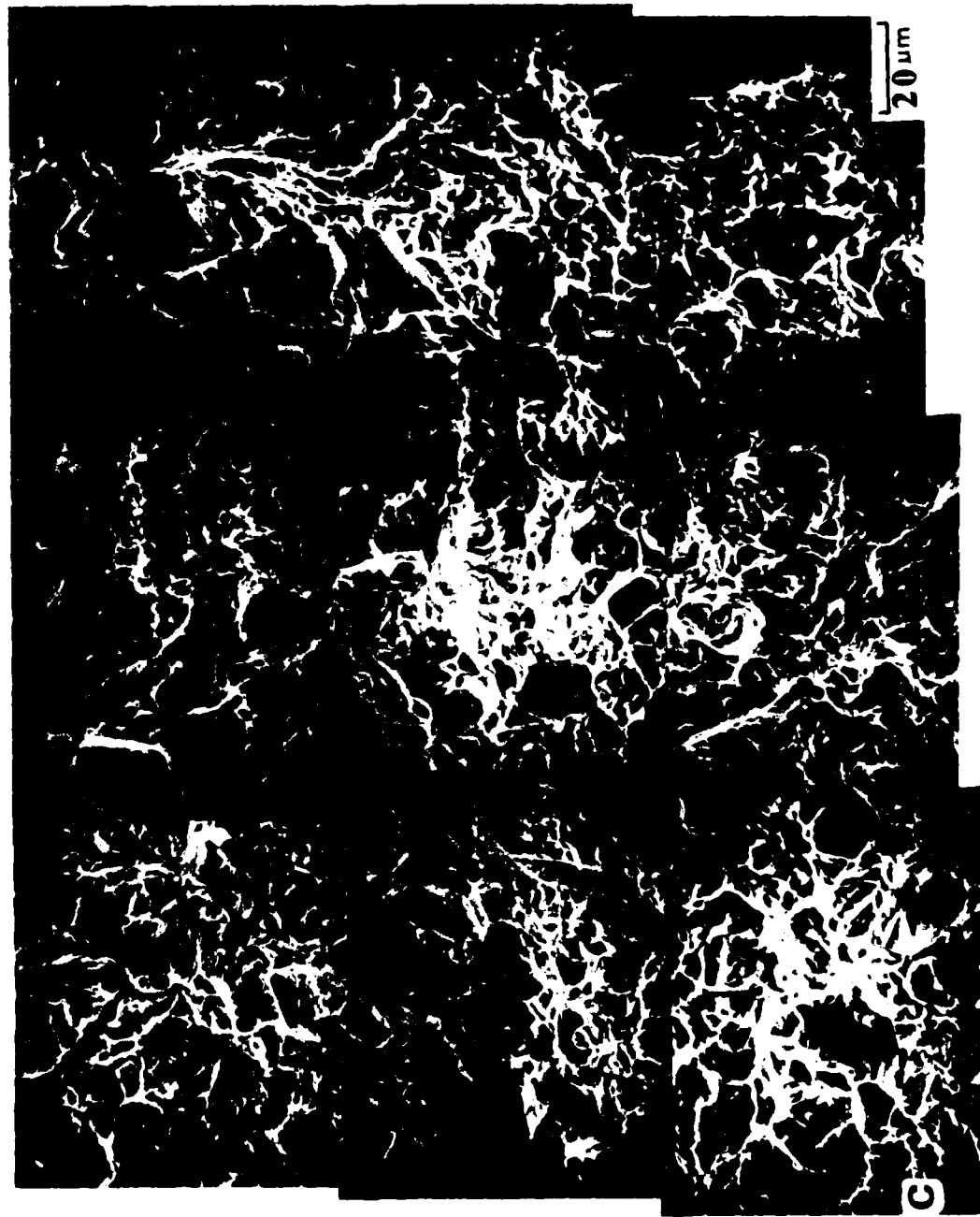
20 μm

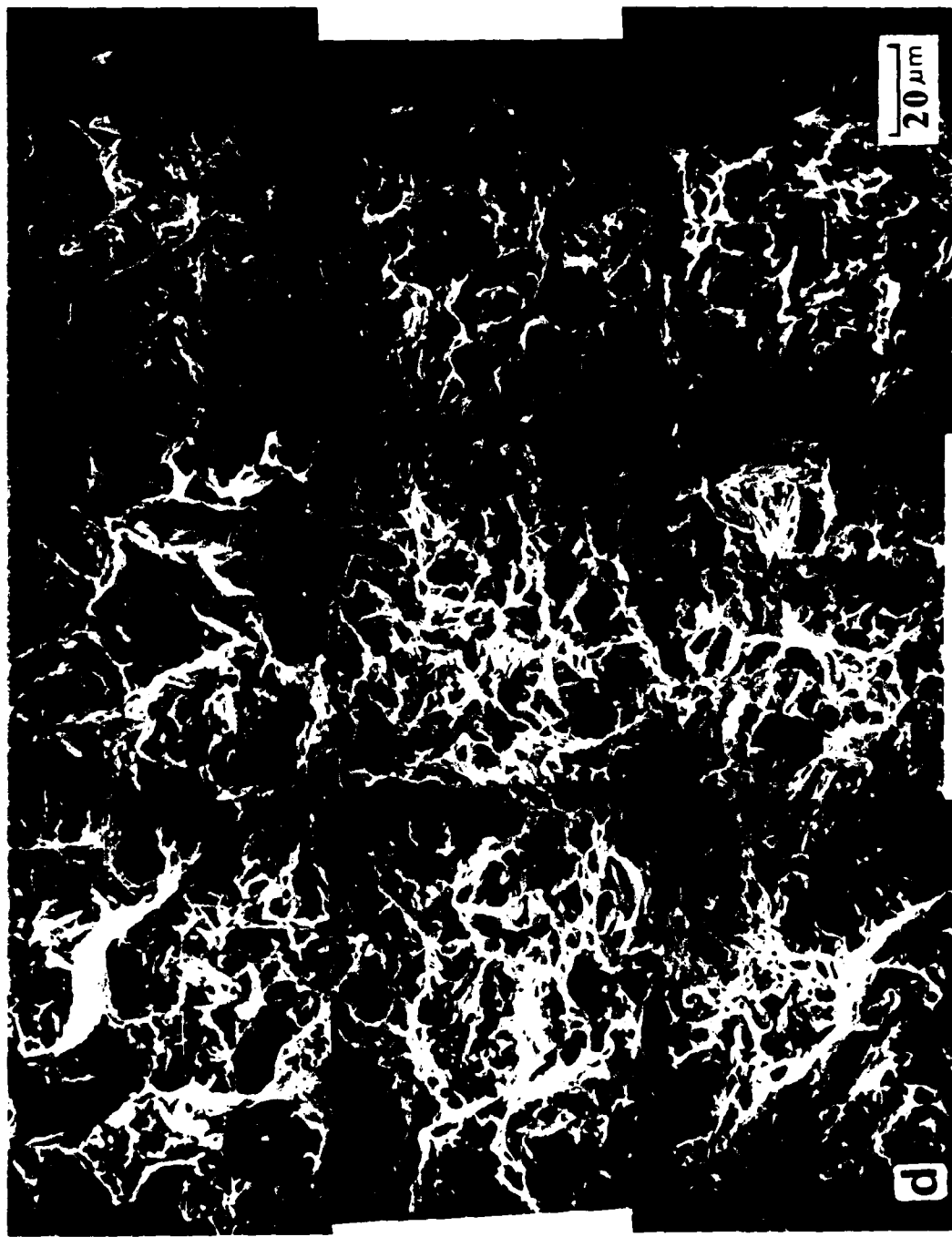
Fig. 44

Scanning electron micrographs of
fracture surfaces of four-point bend
specimens of steel B7 austenitized
at 850°C and tempered at
a) As-Quenched condition
b) 150°C
c) 250°C
d) 350°C
e) 450°C
Low temperature (-196°C) tests.











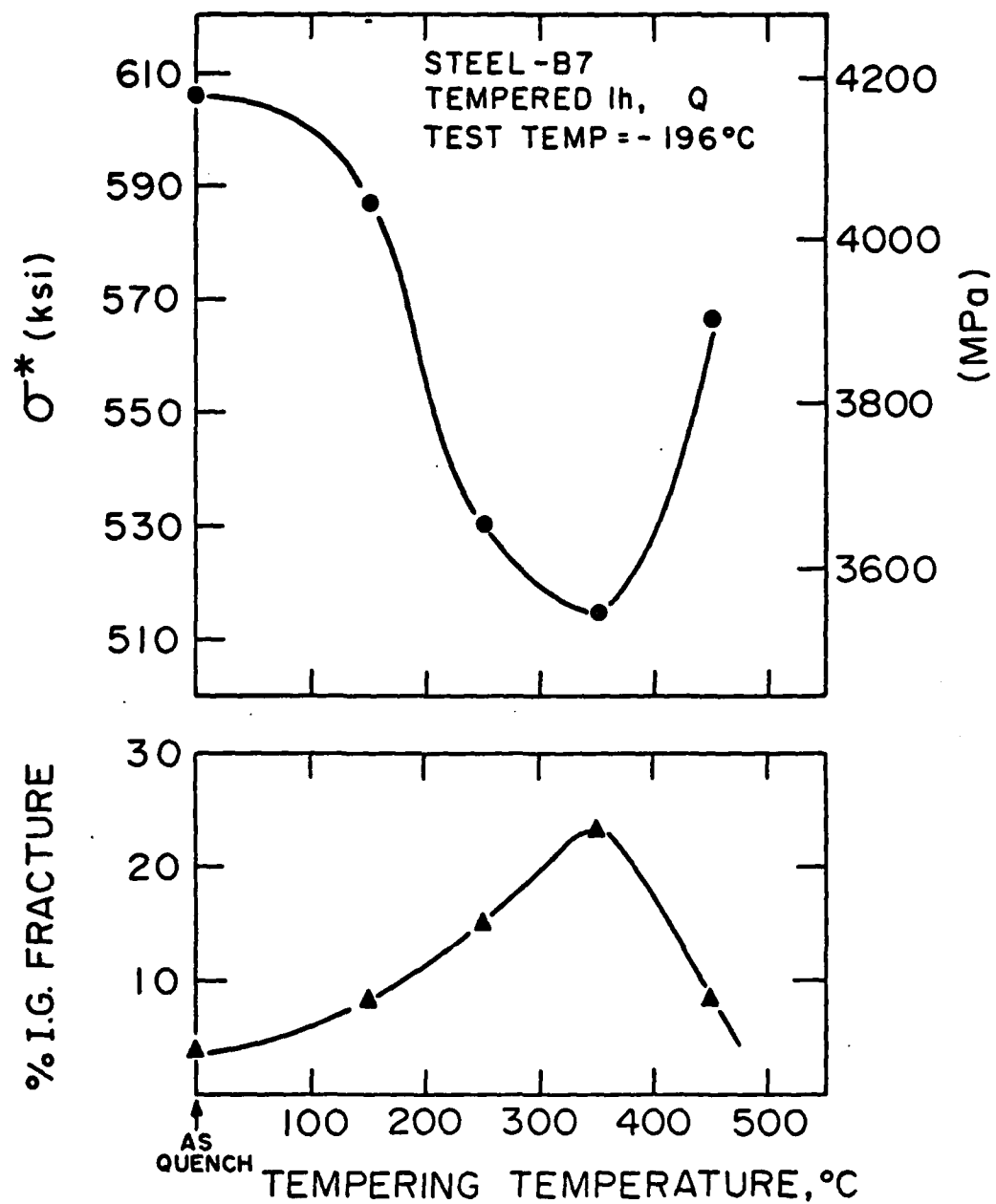


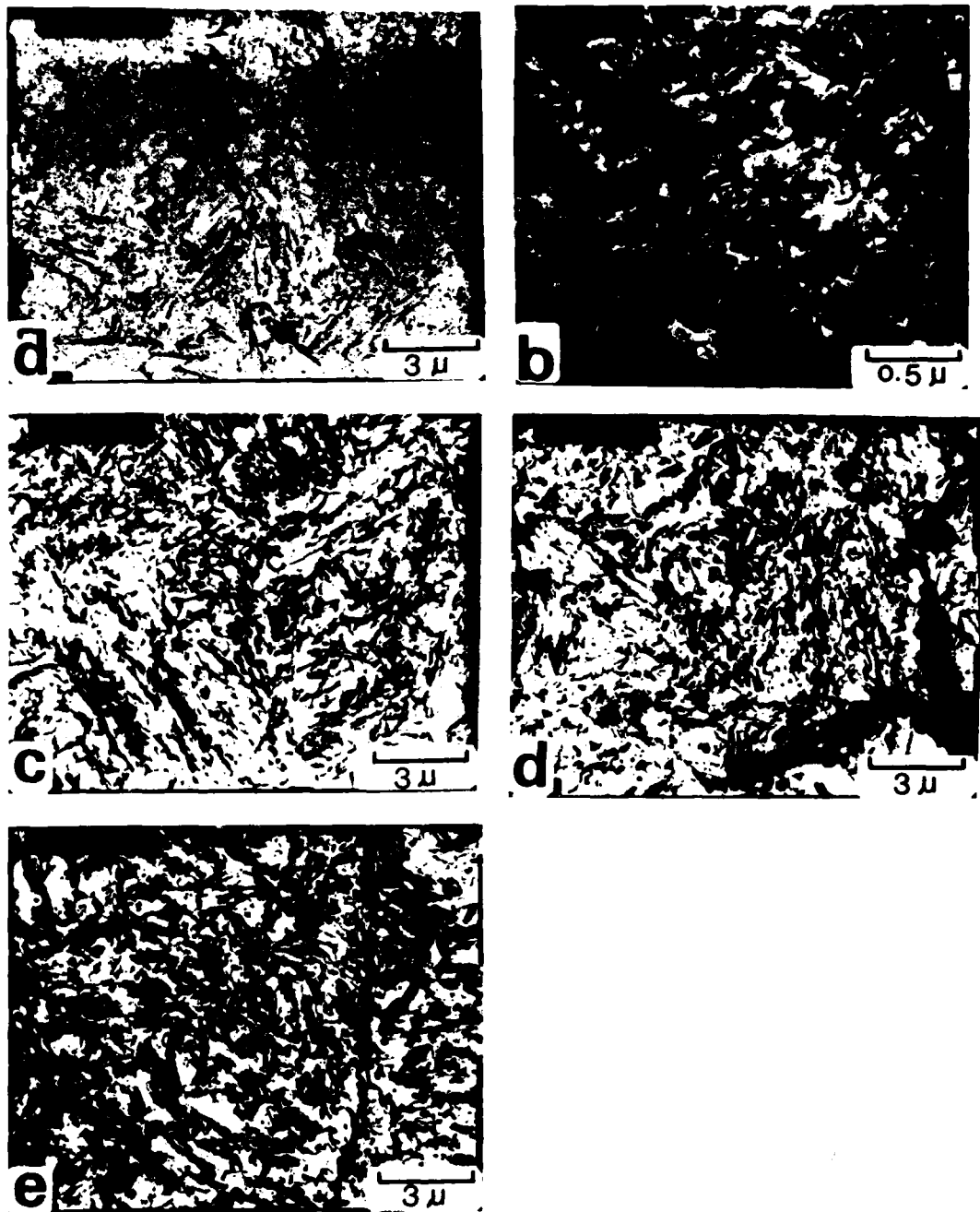
Fig. 45

Variation of critical local stress for fracture σ^* with tempering temperature for steel B7 and corresponding measured amounts of intergranular fracture.

FIG. 46

Carbon extraction replicas of steel B6 showing the grain boundary carbides at various stages of tempering

- a) As quenched
- b) 150°C temper
- c) 250°C temper
- d) 350°C temper, and
- e) 450°C temper.



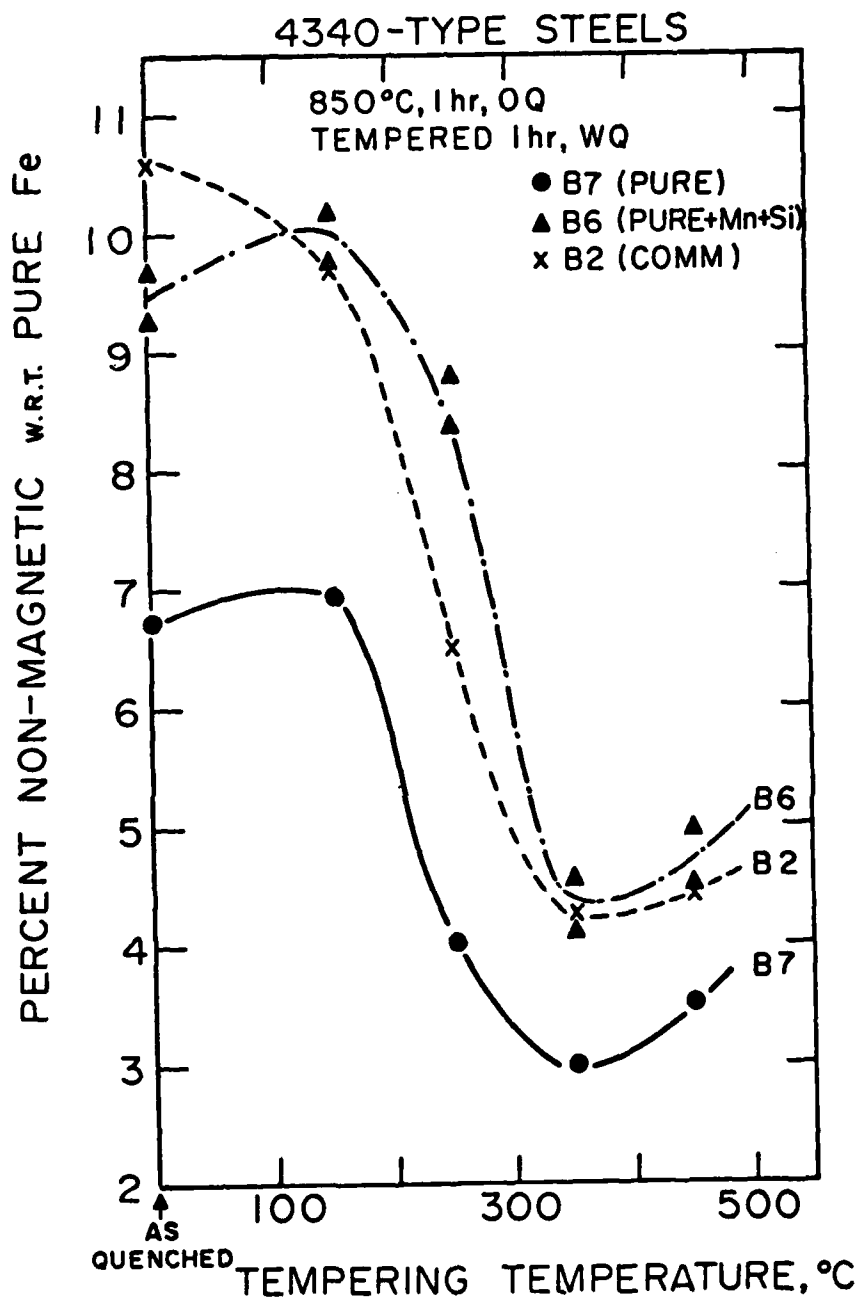


Fig. 47

Variation of percent retained austenite with tempering temperature for two vacuum-melted lab heats B7 and B6 and one commercial heat B2.

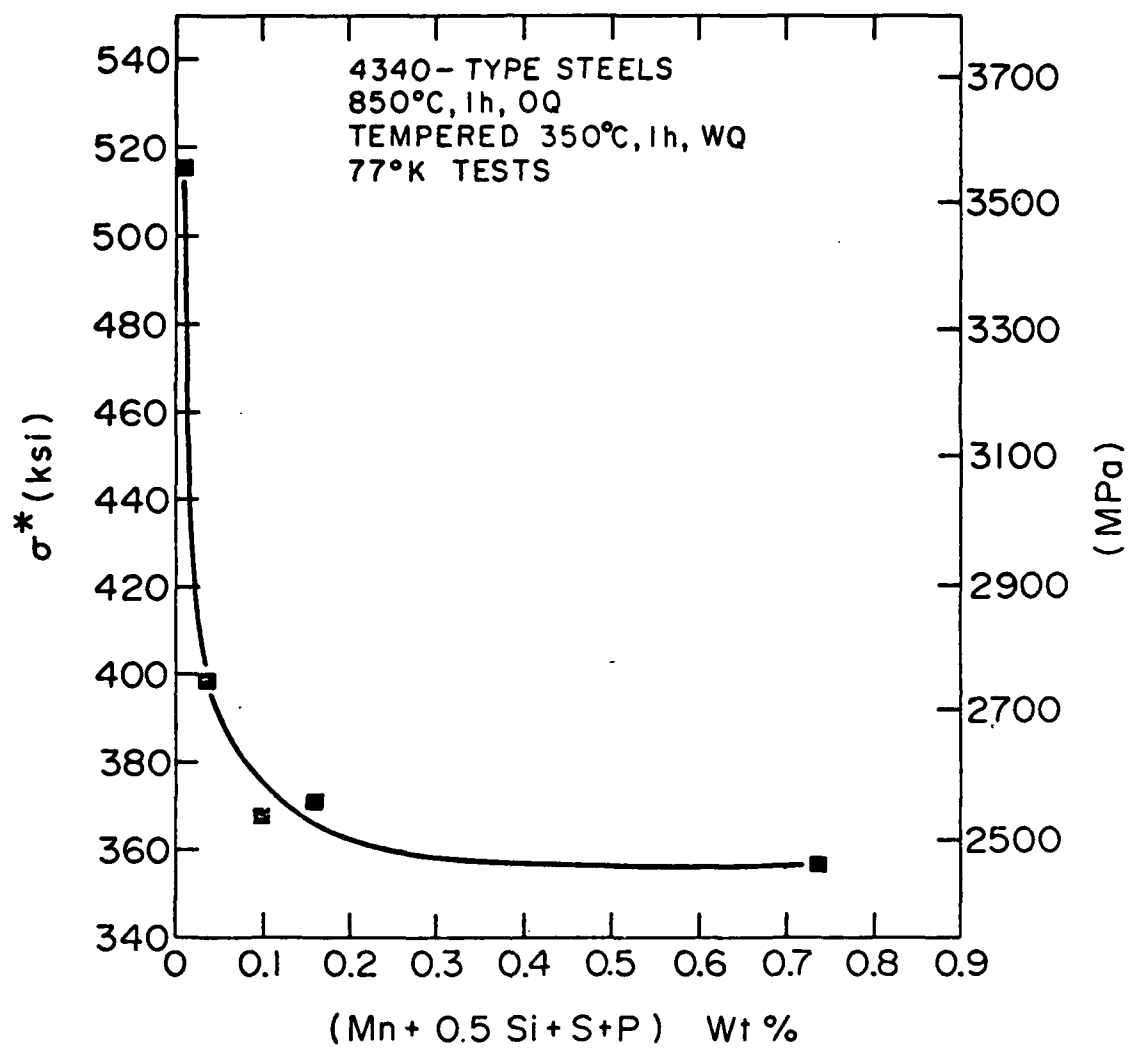


Fig. 48

Variation of critical local fracture stress σ^* with composition parameter $(\text{Mn} + 0.5 \text{Si} + \text{S} + \text{P})$ in wt %.

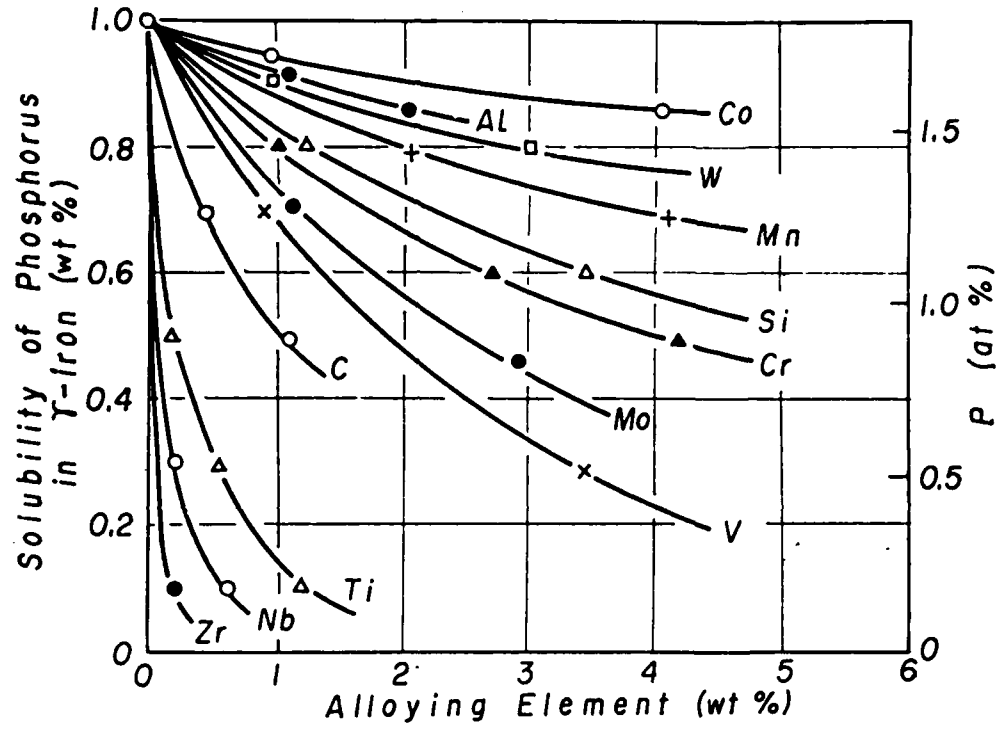
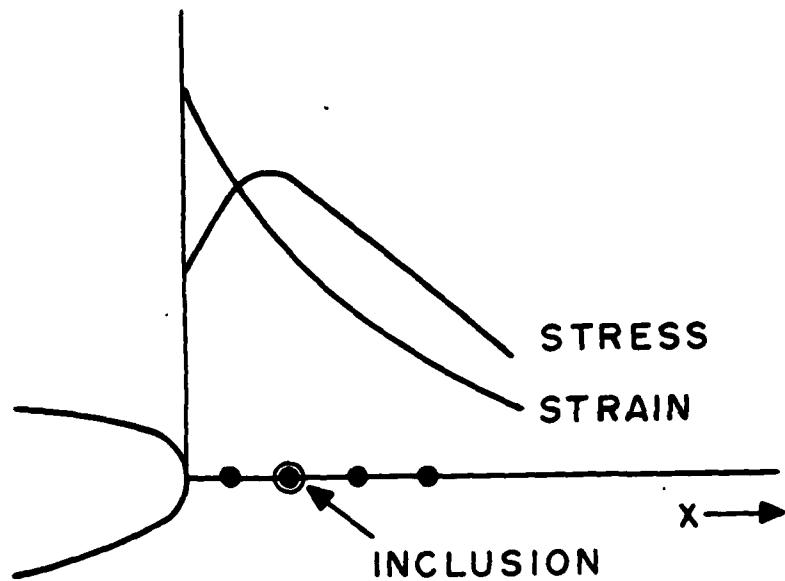


Fig. 49 Effect of alloying elements on the solubility of P in α -Fe containing 12% Ni at 1000°C, from Kaneko et al. (Ref. 89).



(a)



PURE - B7

(b)



COMM. - B2

(c)

Fig. 50

Schematic representation of a) strain and stress profiles ahead of the notch tip. b) Density and size of the inclusion particles in steel B7. c) Density and size of the inclusion particles in commercial air-melted steel B2.

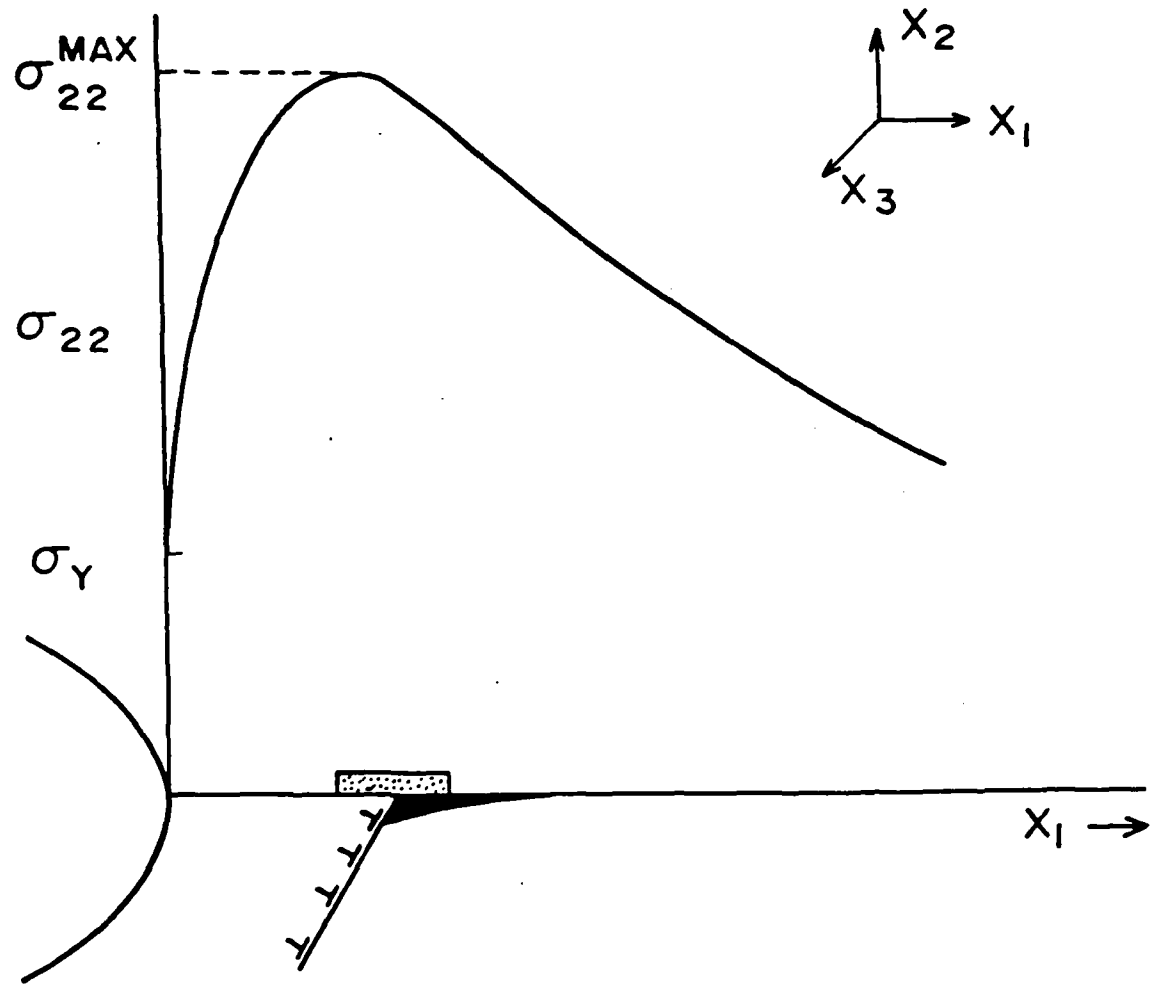


Fig. 51

a) Schematic representation of the conditions necessary for initiation of brittle fracture.

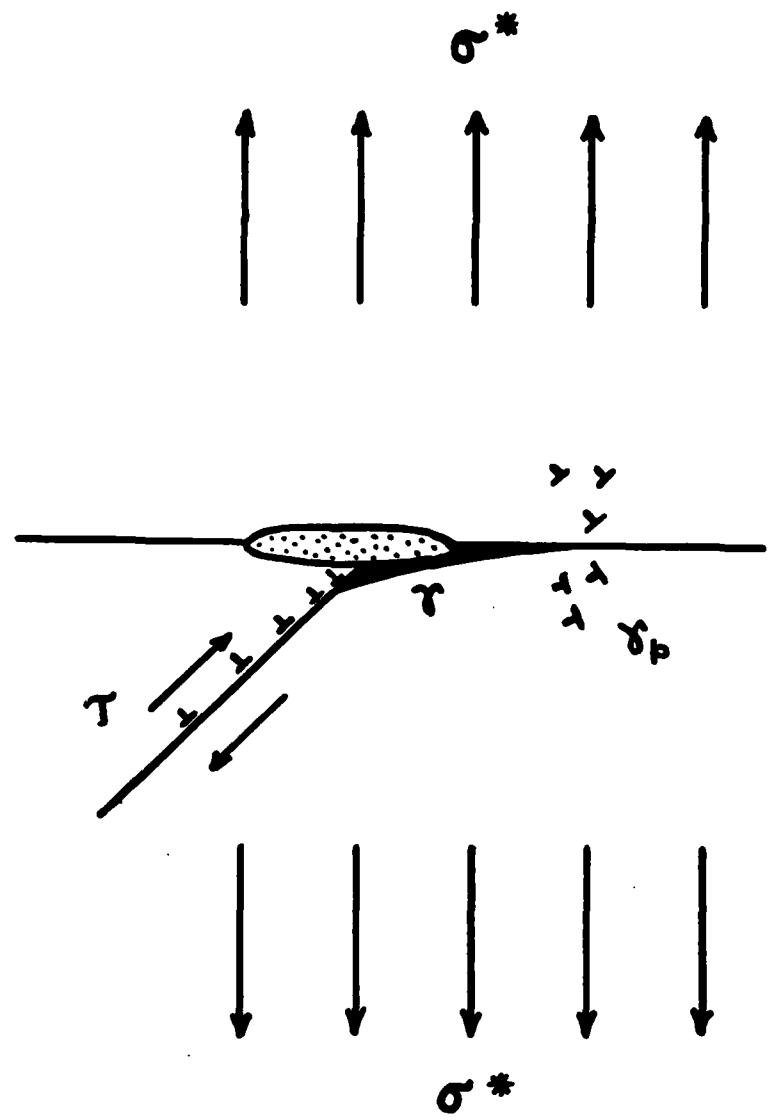


Fig. 51 b) A schematic model for nucleation of intergranular brittle fracture showing the energies involved: γ for bond breaking and γ_p for plastic flow at the crack tip.

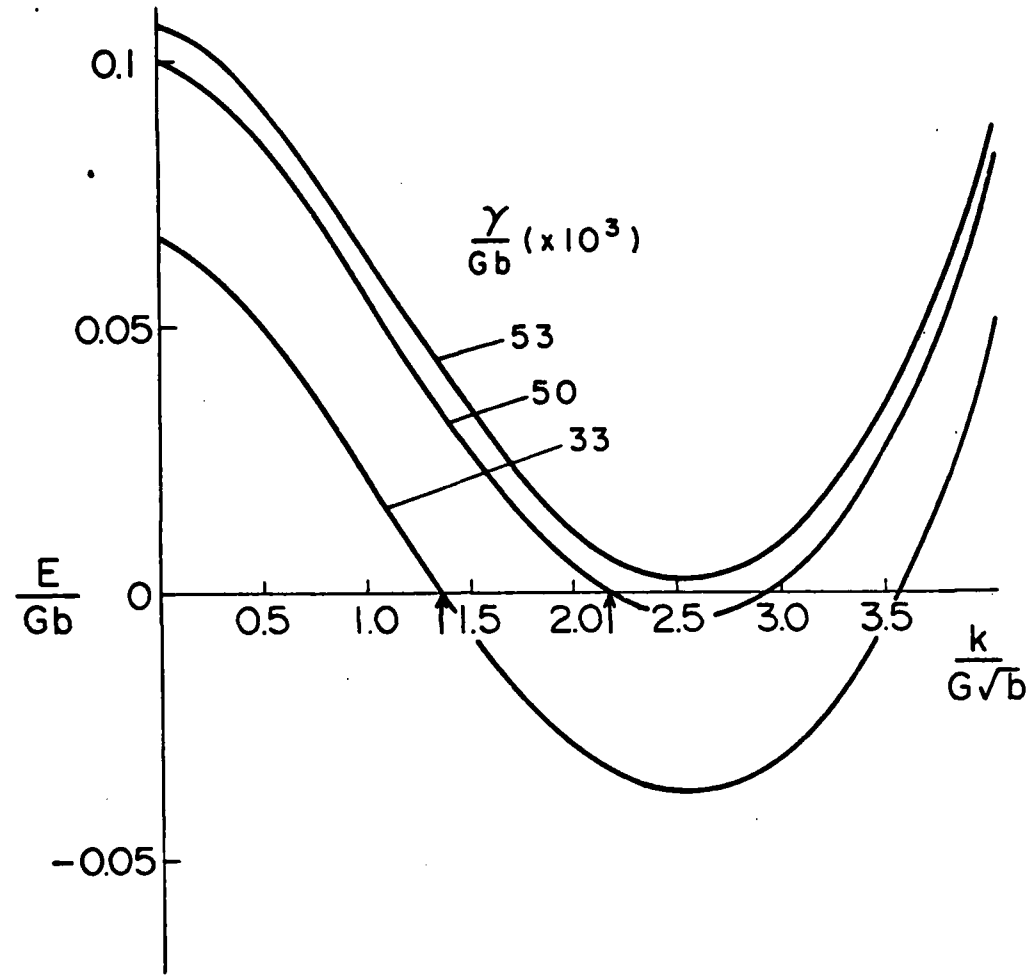


Fig. 52

Dependence of E/Gb on $k/G\sqrt{b}$ for three different values of γ/Gb . (Ref. 98, 129).

Fig. 53

Scanning electron micrographs of fracture surfaces of four-point bend specimens for steel B7 showing intergranular

- a) Second phase particle (presumably inclusion) for the nucleation of brittle microcrack in the as-quenched condition.
- b) Second phase particle (inclusion) and grain boundary carbides for 250°C tempering condition.
- c) Second phase particle (inclusion) and dense grain boundary carbides for 350°C tempering condition.

